



AFRL-OSR-VA-TR-2015-0026

**ADVANCED TECHNOLOGIES FOR STRUCTURAL AND FUNCTIONAL OPTICAL COHERENCE
TOMOGRAPHY**

**James Fujimoto
MASSACHUSETTS INSTITUTE OF TECHNOLOGY**

**01/07/2015
Final Report**

DISTRIBUTION A: Distribution approved for public release.

**Air Force Research Laboratory
AF Office Of Scientific Research (AFOSR)/ RTB
Arlington, Virginia 22203
Air Force Materiel Command**

REPORT DOCUMENTATION PAGE				<i>Form Approved</i> OMB No. 0704-0188	
Public reporting burden for this collection of information is estimated to average 1 hour per response, including the time for reviewing instructions, searching existing data sources, gathering and maintaining the data needed, and completing and reviewing this collection of information. Send comments regarding this burden estimate or any other aspect of this collection of information, including suggestions for reducing this burden to Department of Defense, Washington Headquarters Services, Directorate for Information Operations and Reports (0704-0188), 1215 Jefferson Davis Highway, Suite 1204, Arlington, VA 22202-4302. Respondents should be aware that notwithstanding any other provision of law, no person shall be subject to any penalty for failing to comply with a collection of information if it does not display a currently valid OMB control number. PLEASE DO NOT RETURN YOUR FORM TO THE ABOVE ADDRESS.					
1. REPORT DATE (DD-MM-YYYY)		2. REPORT TYPE		3. DATES COVERED (From - To)	
4. TITLE AND SUBTITLE				5a. CONTRACT NUMBER	
				5b. GRANT NUMBER	
				5c. PROGRAM ELEMENT NUMBER	
6. AUTHOR(S)				5d. PROJECT NUMBER	
				5e. TASK NUMBER	
				5f. WORK UNIT NUMBER	
7. PERFORMING ORGANIZATION NAME(S) AND ADDRESS(ES)				8. PERFORMING ORGANIZATION REPORT NUMBER	
9. SPONSORING / MONITORING AGENCY NAME(S) AND ADDRESS(ES)				10. SPONSOR/MONITOR'S ACRONYM(S)	
				11. SPONSOR/MONITOR'S REPORT NUMBER(S)	
12. DISTRIBUTION / AVAILABILITY STATEMENT					
13. SUPPLEMENTARY NOTES					
14. ABSTRACT					
15. SUBJECT TERMS					
16. SECURITY CLASSIFICATION OF:			17. LIMITATION OF ABSTRACT	18. NUMBER OF PAGES	19a. NAME OF RESPONSIBLE PERSON
a. REPORT	b. ABSTRACT	c. THIS PAGE			19b. TELEPHONE NUMBER (include area code)

AFOSR Grant FA9550-10-1-0551
Advanced Technologies for Structural and Functional
Optical Coherence Tomography
September 30, 2010 to September 29, 2014
Final Report

Table of Contents

1.0 Introduction	2
1.1 Program Highlights	3
2.0 Next Generation OCT Technology	4
2.1 MEMS-tunable VCSELs for Ultrahigh Speed OCT	4
2.2 Functional OCT Imaging	5
OCT Angiography (OCTA)	5
Doppler OCT	6
Polarization Sensitive OCT (PS-OCT)	7
2.3 Ultralong Range Imaging using MEMS VCSEL Technology	10
2.4 Development of Motion Correction Algorithms for Ophthalmology	11
3.0 Ophthalmic OCT	13
3.1 Technology Development for Clinical Ophthalmology	14
3.2 Handheld OCT	16
3.3 Wide Field Retinal Imaging	18
3.4 Long Range Imaging of the Anterior Eye and Full Eye Length Imaging	19
3.5 OCT Angiography of the Retina and Choroid	21
Current Techniques for Visualizing Retinal and Choriocapillaris Microvasculature	21
Development of SS-OCT Angiography using the VCSEL Swept Light Source	21
Demonstration of SS-OCT Angiography Imaging in Normal Subjects	22
Exudative AMD	23
Dry AMD	23
Diabetic Retinopathy	25
3.6 En face Doppler OCT Measurement of Total Retinal Blood Flow	26
Measurement of Total Retinal Blood Flow	26
Conventional Techniques for TRBF Measurement	26
En Face Doppler OCT	27
En Face Doppler OCT with High Speed OCT Technology	27
Synchronized En Face Doppler OCT with Pulse Oximetry Cardiac Gating	28
Clinical Studies of Total Retinal Blood Flow	28
4.0 Brain Imaging	29
4.1 Introduction to OCT for Neuroscience Applications	29
4.2 Quantitative Measurements of Absolute Cerebral Blood Flow (CBF)	31
4.3 DLS-OCT Imaging of CBF and Cellular Viability	31
4.4 OCT Imaging of Capillary RBC Flow Properties	33
4.4 Rapid Volumetric Imaging of Capillary Network Flux	34

5.0 Endoscopic OCT Technology and Applications	36
5.1 Clinical Studies with Endoscopic OCT	36
Characterization of Buried Glands Pre- and Post-Radiofrequency Ablation with OCT	37
Endoscopic OCT Markers of Radiofrequency Ablation Treatment Response	39
5.2 Endoscopic OCT Technology Development	40
Ultrahigh Speed Endoscopic Swept Source OCT	40
Micromotor Endoscopic Imaging Probes	41
5.3 Novel Diagnostics with Endoscopic OCT	42
En Face OCT and Pitt Patterns	43
Endoscopic OCTA and Microvasculature	45
6.0 Pathology Imaging	47
6.1 Multiphoton Microscopy for Rapid Evaluation of Pathology	48
Introduction to multiphoton microscopy (MPM)	48
Preliminary Multiphoton Microscopy Study of Breast Surgical Specimens	49
Development of Ultrahigh Speed Wide Field of View Multiphoton Microscopy for Pathology	51
Development of Gigavoxel Multiphoton Fluorescent Lifetime Imaging Technology	52
6.2 Development of Next Generation Optical Coherence Microscopy Technology	54
Optical Coherence Microscopy (OCM)	54
High Speed Fourier Domain Optical Coherence Microscopy	55
Image Tiling and Display for Large Field of View	57
7.0 Other Collaborations	58
7.1 Computer Aided Diagnosis of Plaque Erosion	58
7.2 OCT for Evaluation of Kidney Transplantation	61
8.0 Publications under AFOSR program	62

1.0 Introduction

This program, AFOSR FA9550-10-1-0551, entitled “Advanced Technologies for Structural and Functional Optical Coherence Tomography,” is a multidisciplinary collaborative program among investigators at the Massachusetts Institute of Technology, Department of Electrical Engineering and Computer Science and Research Laboratory of Electronics (P.I. James Fujimoto, Elihu Thomson Professor of Electrical Engineering and Computer Science); the Harvard Medical School, Massachusetts General Hospital, Martinos Center for Biomedical Imaging (David Boas, Professor in Radiology at Harvard Medical School, Director, Optical Imaging Core & Lab, Martinos Center, Department of Radiology, MGH) and the Tufts University School of Medicine, New England Eye Center (Jay Duker, M.D., Director of the New England Eye Center, Chairman of Ophthalmology). The objective of this program is to develop the next generation of advanced technology for OCT with an emphasis on ultrahigh speed structural and functional imaging and to explore applications in key areas. Emphasis is placed on ophthalmology, the area in which OCT has had the largest clinical impact to date, and brain science, an emerging area where structural and functional imaging are enabling advances in fundamental research. Functional imaging of the retina and brain are synergistic and provide a cross-platform approach to develop and validate new methods. The technology and approaches developed in this program promise to lay the foundation for a range of new applications in fundamental research and clinical medicine.

1.1 Program Highlights

This program was in a one year no cost extension which ended in September 2014 and therefore this Final Report describes results over a four year period. The highlights of the program include technological, scientific and clinical advances, as well as technology transfer and new program development. New technology was developed and translated for studies in multiple clinical applications in ophthalmology and endoscopy. Technology and intellectual property developed under the program was transferred to industry and released a commercial ophthalmic imaging product. AFOSR funding also supported pilot studies in new areas which subsequently lead to the development of new NIH funded research programs. Highlights of major accomplishments in this program include:

- Publication of over 75 peer reviewed journal articles.
- Collaboration with Thorlabs / Praevium Research to develop MEMS-VCSEL lasers as a platform technology for structural and functional swept source OCT imaging. Demonstration of multiple new ophthalmic and endoscopic imaging applications.
- Invention of software based motion correction with collaborators at the University of Erlangen. The technology was transferred to industry and released in 2014 an ophthalmic imaging instrument (Avanti by Optovue) outside of the US and is pending clearance in the US.
- Development and demonstration of handheld ophthalmic OCT technology for 3D retinal imaging.
- Development of prototype OCT technology for ophthalmology which is used for clinical studies at the New England Eye Center, the University of Pittsburgh Eye Center and the Casey Eye Institute, Oregon Health and Sciences University.
- Development of new high performance OCT technology for endoscopic imaging which is used for clinical studies at the Boston VA Healthcare System, Harvard Medical School.
- OCT angiography studies of the choriocapillaris in exudative AMD. This study was featured on the cover of Ophthalmic Surgery Lasers and Imaging Retina, 45, 6, Nov/Dec. 2014, Moul, et al. [1]
- First demonstration of endoscopic OCT angiography enabling three dimensional imaging of subsurface vasculature in the GI tract. This study was featured on cover of Gastroenterology, 147, 6, December 2014, Tsai, et al. [2]
- Demonstration of nonlinear microscopy for assessing cancer pathology in breast surgical specimens. Published in PNAS, 111, 43, 2014, Tao, et al. [3], this study demonstrated that nonlinear microscopy can assess cancer pathology in surgical specimens with comparable sensitivity and specificity to standard histology and promises to reduce rates of second surgeries.
- Development of a new NIH program (R01 CA178636-02, “Intraoperative real time breast cancer margin assessment with nonlinear microscopy”, P.I. James Fujimoto) in collaboration with investigators at the Harvard Medical School and Beth Israel Deaconess Medical Center.
- Development of a new NIH program (R01 DK094877 -01, “Non-invasive evaluation of transplant kidney using OCT”, P.I. Peter Andrews) in collaboration with investigators at the Georgetown University and University of Maryland.

2.0 Next Generation OCT Technology

2.1 MEMS-tunable VCSELs for Ultrahigh Speed OCT

Optical coherence tomography (OCT) is a noninvasive imaging modality which can visualize cross-sectional and three-dimensional tissue microstructure with high resolution and imaging speeds. OCT is analogous to ultrasound, measuring the depth-dependent backscattered power of infrared light instead of acoustic waves. OCT is a powerful technology for biomedical research and clinical diagnostics because tissue can be examined noninvasively in real-time, without excisional biopsy and processing required for histopathology. OCT has excellent imaging resolution (2 to 10 microns) which enables visualization of tissue structure and pathology. OCT has been demonstrated using multiple patient interfaces and medical devices including ophthalmoscopes, endoscopes, catheters, needles, and other clinical or surgical instruments. Extensions of OCT technology including Doppler OCT, OCT angiography (OCTA) and polarization sensitive OCT (PS-OCT) enable integrated structural and functional imaging.

A major focus of this program has been on developing advanced OCT technology for structural and functional imaging, with the aim of creating new methods which would be applicable across a wide range of biomedical applications and clinical specialties. Recent advances in wavelength-swept lasers enable ultrahigh-speed imaging, opening up a wide variety of functional OCT imaging applications. During the previous contract period, our group at MIT worked in collaboration with Praevium Research and Thorlabs to develop MEMS-tunable vertical cavity surface emitting lasers (VCSELs) operating at 1310 nm and 1050 nm center wavelengths and demonstrate swept source/Fourier domain OCT (SS-OCT) in key ophthalmic and endoscopic applications. **Figure 1** shows a schematic diagram and photograph of the MEMS VCSEL laser. The MEMS-tunable VCSELs are wavelength-swept, semiconductor lasers that emit a beam perpendicular to the mirror surface. One of the key features of the MEMS-tunable VCSEL technology is the micro-scale cavity length and high MEMS resonance frequency that allow single longitudinal mode, ultra-narrow linewidth operation at ultrahigh laser sweep rates (>1 MHz). This corresponds to 15 to 40-fold increase in imaging speed compared to commercially available spectral / Fourier domain (SD-OCT) systems. Using this new technology, our collaborative group demonstrated ophthalmic imaging at 400 kHz to 580 kHz A-scan rates [4, 5] as well as endoscopic imaging at 1 MHz A-scan rate [6].

Swept source OCT using the VCSEL laser enables both high speed as well as long imaging range and has been a key technology in this program. High speed is especially powerful because it enables functional imaging such as Doppler flow measurement, motion contrast using OCT angiography (OCTA), or polarization sensitivity OCT (PS-OCT).

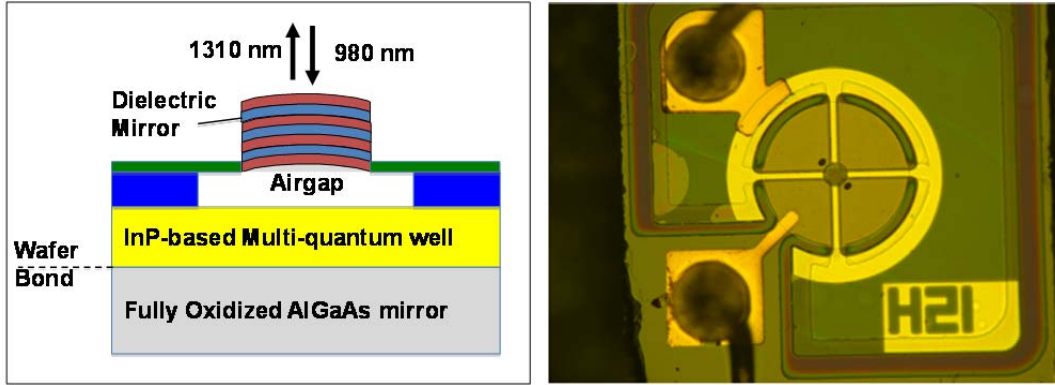


Figure 1. Schematic and photograph of a VCSEL laser. The laser consists of a semiconductor mirror, quantum well gain material and dielectric mirror fabricated on a MEMS. The gain is optically pumped by a laser diode (not shown). The VCSEL cavity is short and can operate in a single longitudinal mode, providing very narrow linewidth. The MEMS mirror is electrostatically actuated and can vary the cavity length to sweep the laser frequency / wavelength. The MEMS mirror can achieve rapid sweep rates as well as adjustable sweep ranges.

2.2 Functional OCT Imaging

OCT angiography (OCTA)

OCT angiography (OCTA) is a functional OCT imaging technique that enables three dimensional visualization of microvasculature without requiring intravenous dyes, such as fluorescein or indocyanine green. OCTA is especially powerful for ophthalmology research and clinical investigation. Retinal and choroidal microvasculature are imaged by measuring fluctuations caused by the passage of red blood cells through an OCT voxel by rapidly acquiring repeated B-scans from the same location [7-16]. Because the same location must be re-scanned multiple times, volumetric OCTA imaging requires much larger numbers of A-scans than structural OCT and ultrahigh imaging speeds are important. Although OCT angiography cannot visualize vascular leakage as is possible with conventional angiography, OCTA can be performed repeatedly because exogenous contrast agents are not administered. Furthermore, because OCT angiography is based on motion contrast, it can potentially provide information on local retinal blood perfusion at the capillary level in addition to three dimensional structural information.

Figures 2 and 3 show retinal and choroidal OCT angiograms acquired using a 1050 nm wavelength, ultrahigh speed swept source OCT prototype instrument operating at a 400 kHz A-scan rate. **Figure 2** shows OCT retinal angiograms of 12 mm × 12 mm and 3 mm × 3 mm regions acquired from a normal volunteer. Although the large field of view OCT angiogram in **Figure 2(A)** visualizes large vascular structure, visualization of progressively finer details requires scanning smaller fields of view as in **Figure 2(B)**. **Figure 3** shows a wide-field mosaicked OCTA spanning ~32 mm on the retina at the level of choriocapillaris, the capillary layer of the choroid, acquired from a normal volunteer. Multiple 3 mm × 3 mm field of view OCTAs were stitched together to generate a panoramic visualization of the choriocapillaris, demonstrating variations in the choriocapillaris density and structure at different locations, consistent with histological studies [17]. Ultrahigh speed is crucial for OCT angiography because it enables larger retinal coverage without stitching and/or higher resolution visualization of microvasculature. Studies of OCTA in ophthalmic and endoscopic applications are further described in sections 3.5 and 5.3.

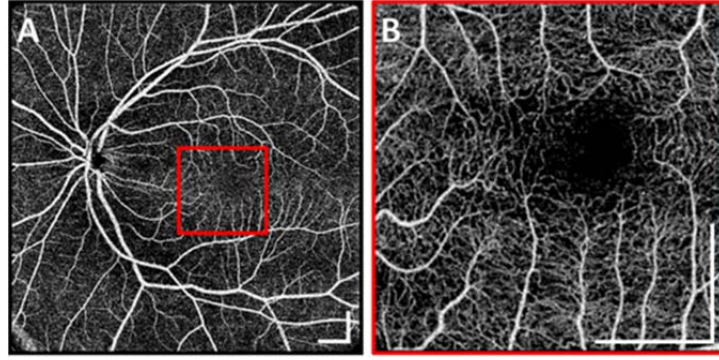


Figure 2. OCT angiograms (OCTA) of retinal capillary structure. (A) 12 mm \times 12 mm and (B) 3 mm \times 3 mm fields showing wide field retinal vasculature as well as the foveal avascular zone. Capillary structure can be imaged in 3D and image analysis can be used to quantitatively analyze the vascular network. Exogenous contrast is not required. Scale bars: 1 mm.

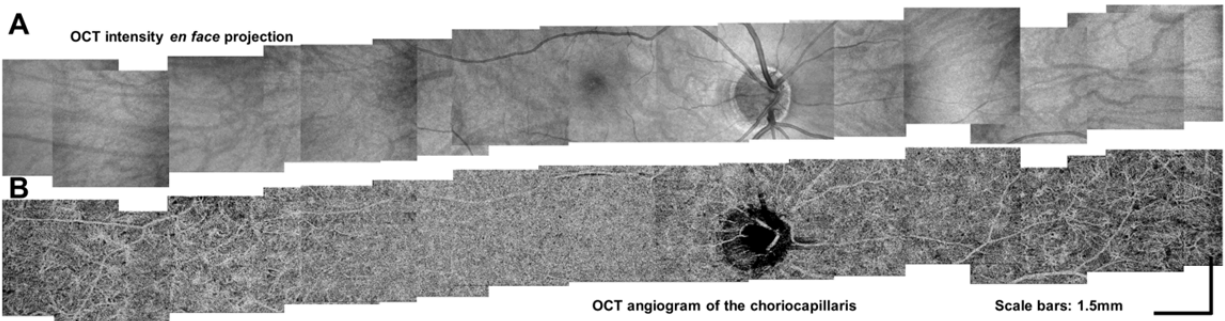


Figure 3. OCT angiograms (OCTA) of choriocapillaris microvasculature spanning ~32 mm on the retina. (A) Mosaicked OCT intensity *en face* projection images. (B) Mosaicked OCT angiograms of the choriocapillaris. Different microvasculature patterns and densities can be observed at different fundus locations, consistent with known histological findings. Scale bars: 1.5 mm.

Doppler OCT

Doppler OCT is another functional OCT imaging technique which is analogous to ultrasound color Doppler imaging. Doppler OCT detects the velocities of moving scatterers such as erythrocytes flowing inside blood vessels. Since Fourier domain OCT acquires phase information along with back-reflected intensity, Doppler measurements can be performed by calculating the difference in optical phase between subsequent A-scans. In ophthalmic applications, retinal blood flow can be assessed by scanning large blood vessels in or around the optic disc. High imaging speed is beneficial for Doppler OCT since Doppler requires the spatial A-scan sampling interval to be much closer than the optical spot size, so that A-scans have correlated speckle information and phase shifts from blood flow can be measured. High speed also enables new measurement techniques such as *en face* Doppler, where blood flow is measured in *en face* planes using a volumetric data set. As described in section 4, this technique was originally developed by Dr. David Boas' group at MGH for measuring blood flow in the brain and was translated to ophthalmology [18]. *En face* Doppler has the advantage that determination of the Doppler angle of the blood vessel is not required, because the total flow can be measured by integrating the velocity over the vessel area in the *en face* plane. However, *en face* Doppler requires extremely high imaging speeds because multiple volumes must be acquired rapidly enough to resolve pulsatile flow from the cardiac cycle. **Figure 4** shows the *en*

face mapping of blood flow velocity in the central retinal artery at different phases in the cardiac cycle. Applications of Doppler OCT to ophthalmology are discussed in section 3.6.

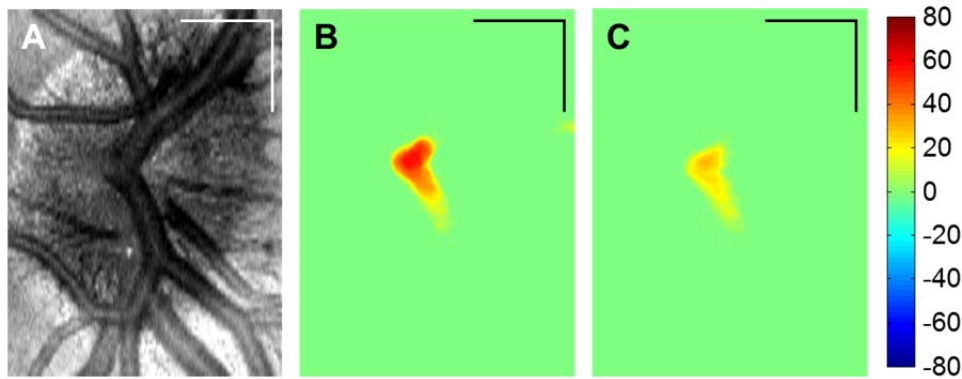


Figure 4. *En face* Doppler OCT. (A) *En face* OCT of human optic disc and (B, C) blood flow velocity map measured by Doppler OCT. A $1.5 \text{ mm} \times 2 \text{ mm}$ area was raster scanned to generate volumetric OCT data. A blood flow velocity map was extracted from the automatically selected *en face* plane at an optimal depth. Units $\mu\text{L}/\text{min}$, scale bars: 500 μm .

Polarization sensitive OCT (PS-OCT)

PS-OCT is a functional extension of conventional OCT that can assess depth-resolved tissue birefringence in addition to intensity [19]. Examples of birefringent tissue include: corneal stroma, sclera and retina nerve fiber layer (RNFL), collagen, muscle, tendons, nerve, bones, cartilage and teeth. Alteration of tissue birefringence is often a hallmark for disease progression. PS-OCT has been applied for anterior and posterior eye imaging [20], burn depth and thermal damage assessment [21], and collagen assessment for atherosclerotic plaque characterization [22]. Although many different PS-OCT techniques have been demonstrated [23-29], their clinical translation has been complicated by their high degree of complexity. Free space PS-OCT systems are susceptible to misalignment and are difficult to operate [25]. Fiber based PS-OCT using polarization maintaining (PM) fibers requires compensation of PM fiber mismatch between reference and sample arms in post-processing [24]. Moreover, these PS-OCT techniques require known polarization states of the incident light on the sample, which is difficult to achieve in catheter or endoscope-based OCT. Fiber-based PS-OCT using polarization multiplexing illuminates the sample with two or more polarization states [27-29] and can be used in catheter-based OCT. However, most existing fiber-based PS-OCT systems are complex and require high system SNR, long imaging range and high phase stability.

We have developed a simpler, more compact and robust all-fiber swept source PS-OCT technique that is particularly suitable for clinical translation. The system diagram is shown in **Figure 4**. Polarization multiplexing and polarization sensitive detection are used to extract tissue birefringence. Polarization multiplexing is performed using a polarization maintaining (PM) fiber in the sample path. PM fiber has polarization mode dispersion (PMD), and by selecting a proper length of PM fiber, signals from the two orthogonal polarization states of the input light can be acquired in a single A-scan, but separated at different depths. For polarization sensitive detection, two fiber-based polarization beam splitters (FPBS) are used to eliminate free space to fiber coupling and improve sensitivity. Polarization controllers are used to balance the FPBS based polarization sensitive detection, which can be shown by Jones Matrix analysis to unambiguously resolve the tissue birefringence.

Fiber-based OCT systems greatly augment the ability of OCT by enabling fiber coupled, handheld OCT instruments as well as catheter, endoscope and needle based imaging which can access luminal organ systems such as the gastrointestinal and pulmonary tracts as well as solid organs and tumors [30]. We have recently demonstrated a catheter / endoscope based PS-OCT system with an all-fiber PS-OCT design (**Figure 5**) using a MEMS-tunable VCSEL light source [31] and a micromotor imaging probe [6]. **Figure 6** shows preliminary imaging results from the PS-OCT system in human finger, lip, *ex vivo* swine esophagus and coronary arteries. It can be seen that PS-OCT provides tissue birefringence contrast which can differentiate layers inside the tissue. For example, in the esophagus, epithelium is associated with low birefringence, whereas lamia propria and muscularis mucosa have high birefringence (**Figure 6 (F-G)**).

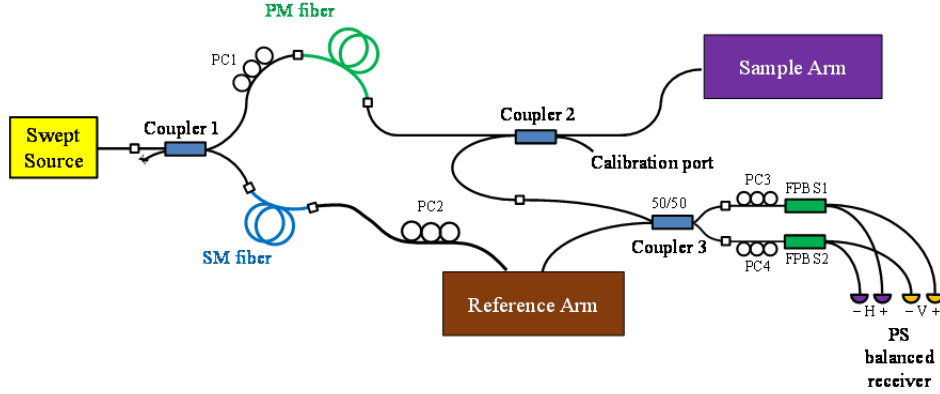


Figure 5. Schematic of the depth-encoded all-fiber PS-OCT system. The system uses a short length of PM fiber to generate two time multiplexed incident polarization states. The OCT interference signal is detected with a polarization sensitive dual balanced detector. This technique is simpler and more robust than previous approaches and promises to enable a wide range of clinical applications.

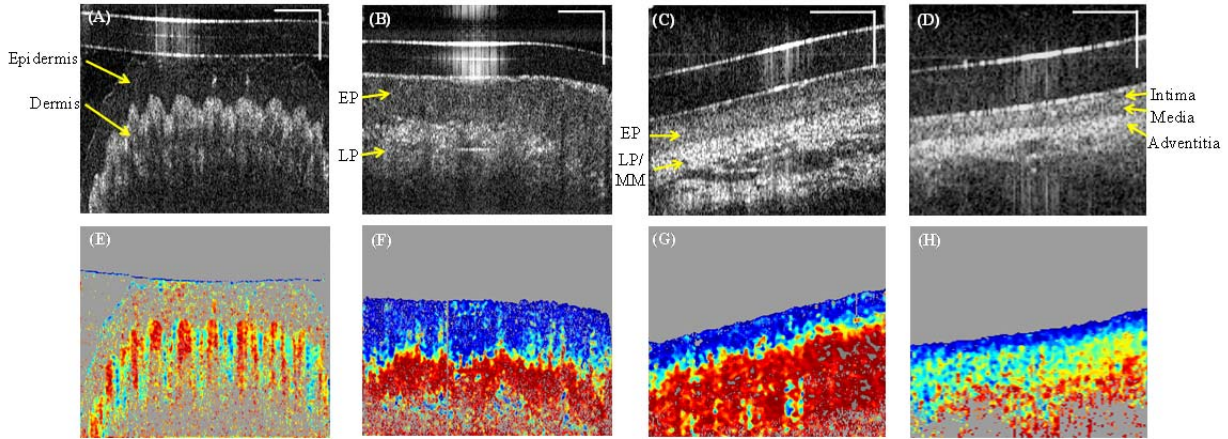


Figure 6. Catheter-based PS-OCT imaging. (A) A single frame OCT intensity image of thick skin from a human index finger tip. (E) Corresponding phase retardation image shows high retardance at the dermal papillae. (B) A single frame intensity image of human lip. (F) Corresponding phase retardation image shows low retardance at the epithelium (EP) and high retardance at the lamia propria (LP). (C) Single frame intensity image shows the epithelium (EP) and lamia propria (LP) / muscularis mucosa (MM) layers of swine esophagus *ex vivo*. (G) Corresponding phase retardation image shows low retardance at EP but high retardance at LP/MM. (D) Single frame intensity image of a swine right coronary artery *ex vivo*. (H) Corresponding phase retardation image shows low retardance in the intima layer, and high retardance in the media and adventitia. Horizontal scale bar: 30 degrees; vertical scale bar: 500 um.

OCT speckle noise can significantly affect polarimetry measurement and must be reduced for birefringence calculation [32-34]. Conventional speckle reduction methods which use complex data averaging at surface Jones matrices [32], or directly on the Stokes vectors [33] or Jones matrices [35], require phase stability over successive A-scans. However, for SS-OCT, laser sweep jitter or sampling fluctuation can make the phase unstable. Existing phase stabilization methods complicate PS-OCT designs [5, 36]. In addition, if phase stability is required, it is not possible to average data over multiple acquisitions or data which has been motion corrected using automated software [37]. We developed a simplified speckle reduction method which does not require phase stability, thereby greatly simplifying system design and implementation. By multiplying the measured Jones matrices by the inverse of the surface Jones matrix [26], we can generate a matrix similar to a diagonal matrix. The phase difference of the two eigenvalues of the similar matrix contains the phase retardation information from the tissue. It can be shown that the two eigenvalues suffer from the same unstable phase. By sorting the eigenvalues with respect to their magnitude, averaging can be directly performed over the eigenvalue ratio, cancelling the unstable phase. Preliminary retinal imaging results utilizing averaging over a small kernel and over repeated frames are shown in **Figure 7**. This technique enables more accurate polarimetry measurement and quantitative assessment of tissue birefringence.

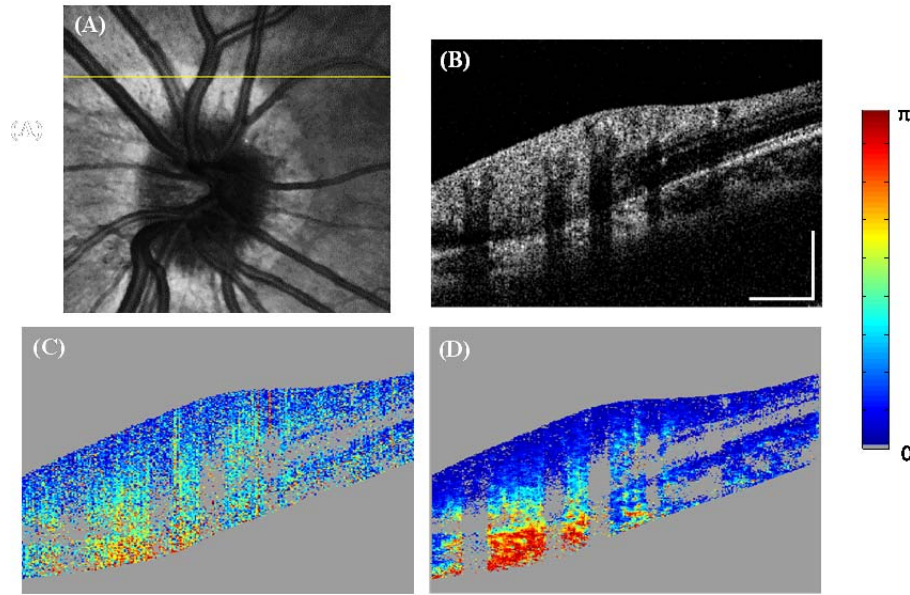


Figure 7. Retinal PS-OCT imaging with speckle noise reduction. The scan area is $3 \text{ mm} \times 3 \text{ mm}$ with $300 \times 300 \times 5$ A-lines/volume (5 repeated B-scans per location). (A) OCT fundus image. (B) Single frame cross-sectional intensity image. (C) Corresponding phase retardation image without speckle noise reduction (D) Phase retardation image using speckle noise reduction. Scale bar: 500 μm .

Esophageal cancer is one of the most lethal malignancies, with a five-year survival rate of only 16% [38]. Barrett's Esophagus (BE) is associated with gastroesophageal reflux disease (GERD) and BE with dysplasia confers an increased risk of esophageal adenocarcinoma [39]. Endoscopic RFA is a therapy [40-44] utilizing electrode arrays to deliver radiofrequency (RF) energy superficially to ablate BE with a low stricture rate [45, 46]. However, repeated RFA treatments are required to achieve complete eradication of intestinal metaplasia (CE-IM) [47-49]. Improving the effectiveness of RFA would reduce the number of treatments, improve cost effectiveness and make therapy more widely available. However, currently there are no effective

methods to directly evaluate the efficacy of RFA. Our previous studies showed that endoscopic OCT could identify markers of treatment response based on BE thickness pre-treatment or residual glandular structure post-treatment [50]. In addition to structural OCT, our preliminary studies also suggest that RFA results in loss of tissue birefringence due to thermal damage of the lamia propria, which can be assessed by PS-OCT. **Figure 8** shows endoscopic PS-OCT imaging of the swine esophagus *ex vivo* before **Figure 8 (A, B)** and after RFA (**Figure 8 (C, D)**). Before RFA, the low retardance epithelium can be clearly differentiated from the underlying high retardance lamina propria / muscularis mucosa layer. After RFA, the low retardance region extended deeper, indicating loss of birefringence caused by the ablation.

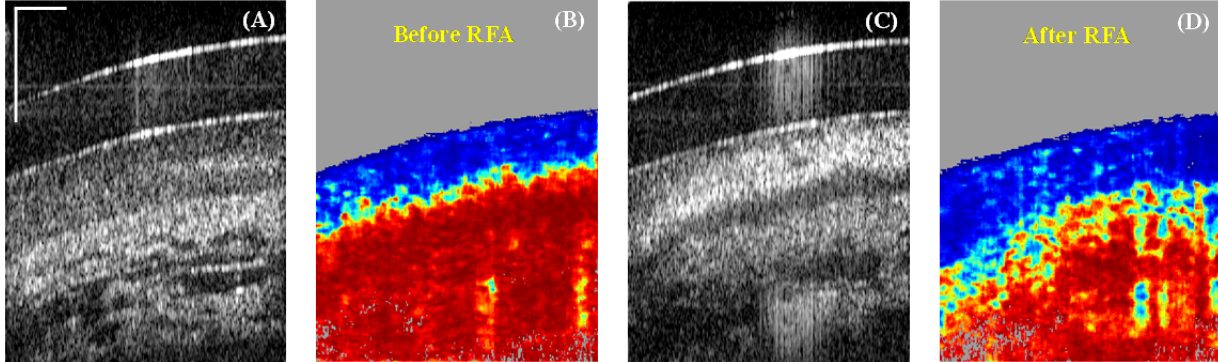


Figure 8. Endoscopic PS-OCT imaging for monitoring RFA. Preliminary results from the swine esophagus *ex vivo*. RFA was applied 2x with an energy of 15 J/cm^2 , consistent with clinical treatment protocols. Intensity and phase retardation images of swine esophagus before (A, B) and after RFA (C, D). The phase retardation images were averaged over 10 frames after non-rigid registration to correct catheter non-uniform rotational distortion. Horizontal scale bar: 30 degrees; vertical scale bar: 500 μm .

2.2 Ultralong Range Imaging Using MEMS VCSEL Technology

The micron-scale cavity length of MEMS-tunable VCSELs enables single longitudinal mode operation, resulting in an extremely long coherence length, estimated to be in excess of 100 meters. This is significantly longer than the coherence length of other swept lasers using a short cavity, which is on the order of millimeters to 1 cm. Whereas the imaging range of traditional SS-OCT systems has been limited by laser coherence length, VCSEL systems are only limited by the analog detection bandwidth and A/D sampling rate, potentially enabling micron-scale measurements of macroscopic objects. The VCSEL can be adjustably scanned with a programmable drive waveform, enabling the available analog bandwidth to be optimized for imaging range, axial resolution, or A-scan rate. We utilized the long imaging range to visualize the anterior segment of the human eye which comprises the cornea, iris and crystalline lens [4]. The results are summarized in section 3.4.

In addition to biometry and full-eye imaging, the ability to image many centimeter scale objects at micron resolution may have important industrial or military applications in nondestructive testing and validation. To demonstrate this capability, we performed long range OCT imaging of large objects, including a high aspect ratio machined metal optical housing, light bulbs, and ammunition [51]. **Figure 9** shows examples of long range OCT imaging.

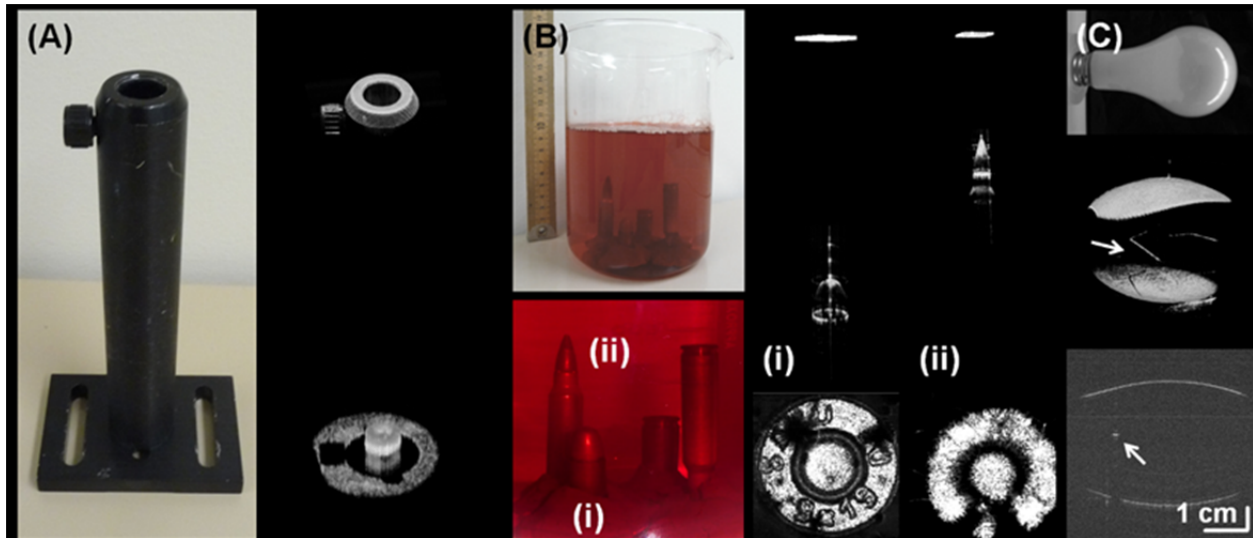


Figure 9. Applications of long range OCT imaging. Imaging examples of (A) Optical post holder which has a high aspect ratio bore hole. (B) Bullets in colored gelatin. (C) Light bulb. White arrow indicates the filament holder.

2.4 Development of Motion Correction Algorithms for Ophthalmology

Working in collaboration with Prof. Joachim Hornegger's group at the Friedrich Alexander University of Erlangen-Nuremberg in Germany, we have developed new software based motion correction technology for ophthalmic OCT that corrects eye motion in transverse and axial directions and enables multiple volumetric data sets to be merged to increase signal to noise [37, 52]. Intellectual property was filed based on this research (US Patent Application 13/097785, Filed April 29, 2011, Kraus, et al. "Method and Apparatus for Motion Correction and Image Enhancement for Optical Coherence Tomography"). The technology was licensed and transferred to Optovue, Inc. and released in a commercial ophthalmic OCT instrument (the Optovue, RTVue-XR) in 2014, which is available outside the United States. Approval in the US is pending. This is an example of a successful technology translation under the AFOSR program.

Even with improvements in imaging speed, there is a drive to acquire high density volumetric data sets in clinical ophthalmology because they enable the generation of *en face* OCT images of the retina. The acquisition of volumetric data sets can take 2-3 seconds. This makes volumes susceptible to motion artifacts from heartbeat and involuntary eye movement, especially in elderly subjects who may have difficulties fixating. OCT volumes are acquired by raster scanning the retina where the OCT beam acquires an A-scan at one location on the retina at a time. Transversely scanning the beam along a line, called the fast scan direction, generates a B-scan cross-sectional image. Acquiring a series of B-scans at offset positions, called the slow scan direction, generates an OCT volumetric data set. Motion artifacts occur predominantly in the slow scan direction because the data acquisition in the fast scan direction is rapid enough to minimize motion artifacts. Working in collaboration with the group at the University of Erlangen, we have developed a software based registration and motion correction technique where two volumes are imaged with orthogonal fast scan directions and then registered to one another. **Figure 9** shows fundus projections of input and motion corrected volumes.

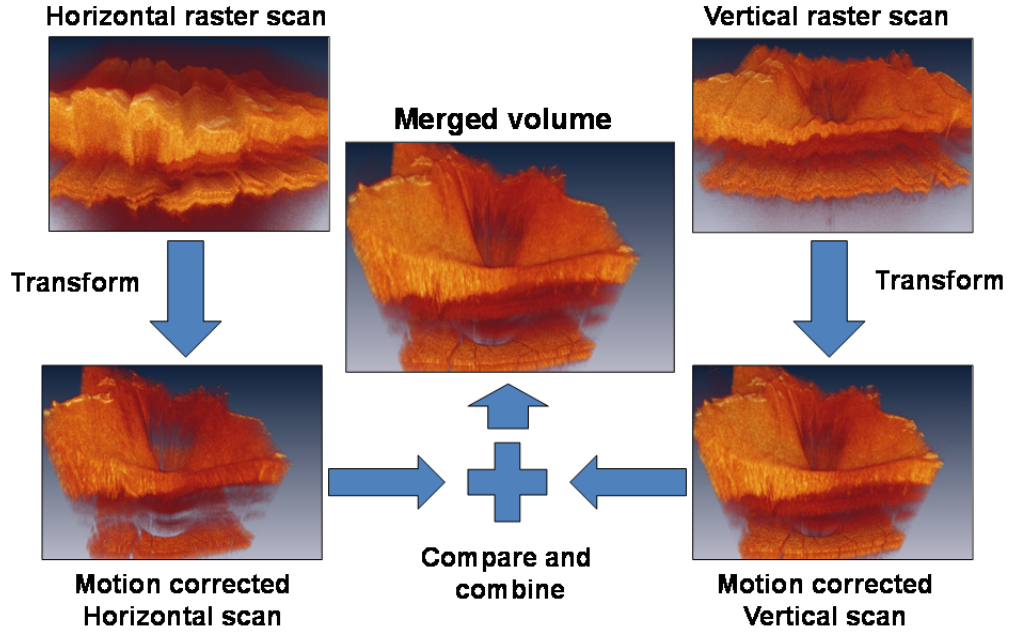


Figure 9. Software motion correction. Two orthogonal raster scanned volumes are acquired and transforms used to motion correct the volumes. The transforms are iteratively calculated to optimize the similarity between the transformed volumes while penalizing motion. The two motion corrected volumes are then merged to generated a volume with improved signal to noise..

The motion correction algorithm operated using two 2D displacement fields for the horizontal and vertical raster scanned volumes which are iteratively optimized to correct motion [37]. These fields consist of 3D displacement vectors for every A-scan. A non-linear optimization algorithm maximizes the similarity between the displaced volumes while a regularization term penalizes abrupt changes in the displacement field. To reduce the risk of the optimization converging at a local minimum, a multi-resolution approach is employed. After registration, the input volumes are merged into one output volume to improve SNR and coverage of the scanned area. The use of motion correction technology to reduce motion artifacts avoids the need for additional hardware, such as eye tracking devices in the OCT device. The motion correction algorithm can potentially be applied to data from every OCT device which employs the orthogonal raster scan pattern.

Recently, an advanced version of the motion correction algorithm was developed [52]. The advanced motion correction method adds several elements to further enhance performance and robustness to variations in input data quality. Variations in alignment of the OCT instrument to the patient's eye between scans can cause the imaged volumes to exhibit varying amounts of tilt along the transverse directions (**Figure 10**). To mitigate this effect, the advanced approach employs a two-stage optimization (**Figure 11**). The first stage compensates for tilt only and the adjusted volumes are used for full optimization in the second stage.

Differences in alignment, vignetting or lens opacities can also cause differences in intensity between subsequent volumes acquired from the same area. To correct for these differences, illumination correction was introduced as a preprocessing step. Based on the OCT fundus projection for a given input volume, a bias field is computed (**Figure 12**). This bias field is then used to correct the intensities across the entire volume.

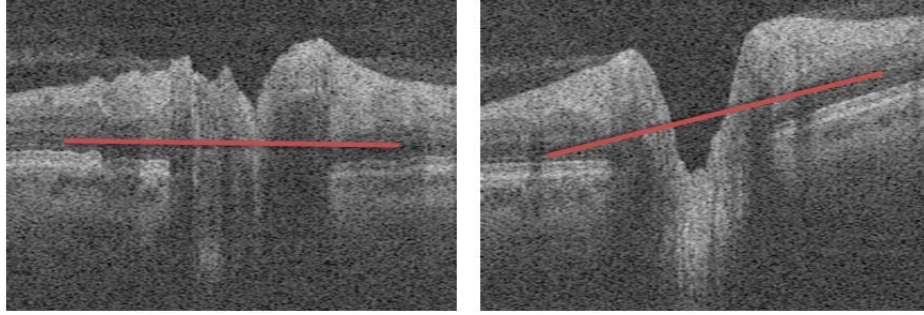


Figure 10. Cross sections from consecutive orthogonal raster volumes showing different amounts of tilt, indicated by the red lines.



Figure 11. Improved, two stage, motion correction algorithm. The first stage performs a rough compensation of tilt using multi-resolution optimization. The tilt-corrected volumes are then used for a full optimization in stage two.

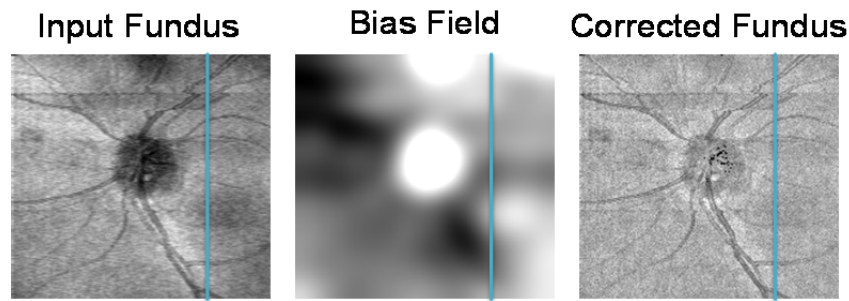


Figure 12. An input OCT fundus image, the corresponding bias field and the illumination corrected OCT fundus image.

Quantitative evaluation was performed using a large set of data acquired from 73 healthy and glaucomatous eyes using SD-OCT instruments and showed that the advanced motion correction technology improves robustness and reproducibility of quantitative measurements between different scans when compared to the first generation algorithm [52]. As noted previously, IP was filed on this technology and it was licensed and transferred to Optovue, Inc. and released in a commercial ophthalmic OCT instrument (the Optovue, RTVue-XR) in 2014.

3. Ophthalmic OCT

OCT imaging of the eye has continued to be one of our program's major research areas, dating back to our initial invention and development of OCT in 1991 [53]. OCT enables ophthalmologists to obtain *in vivo* cross-sectional and volumetric images of the retina and choroid which was not possible to obtain with previous imaging techniques. OCT is now a standard imaging modality in clinical ophthalmology. Although there is considerable commercial development of OCT instrumentation in ophthalmology, our group has continued research in this area and remained at the forefront of OCT technological development. In the previous grant period, we developed and deployed prototype, swept source OCT instruments to multiple clinical

sites, Dr. Jay Duker, at the New England Eye Center, Dr. Joel Schuman at the University of Pittsburgh Eye Center, and Dr. David Huang at the Oregon Health and Sciences University. These instruments used commercially available swept laser sources operating at 100 kHz A-scan rates at 1050 nm wavelength and were in use 3 years before the introduction of commercial swept source OCT technology.

Working in collaboration with Praevium Research and Thorlabs, we have developed ultrahigh speed VCSEL swept light sources for use in handheld OCT instrumentation, ultrawide field retinal imaging, and long range anterior and full eye imaging. Furthermore, the ultrahigh speed of the VCSEL light source is critical for OCT angiography and Doppler of the retina. These advanced OCT technologies can provide functional information about three dimensional microvascular structure and blood flow that promise to elucidate pathogenesis as well as develop new diagnostic or progression markers for ocular diseases which are leading causes of blindness.

3.1 Technology Development for Clinical Ophthalmology

Our group collaborates with clinical investigators at the New England Eye Center, Oregon Health and Science University (OHSU) and University of Pittsburg Medical Center (UPMC) to translate new OCT technology development in our laboratories for studies in the ophthalmology clinic. Technology translation is a challenging engineering task because it requires developing a robust, self-contained OCT imaging system, which ergonomics which is suitable for use in the ophthalmology clinic and which can transported and operated at a remote site. Multiple design considerations must be addressed to enable operation in the clinical environment which greatly differs from the typical laboratory setting. Close interaction with clinical investigators is necessary to understand the workflow in the clinic, the clinical applications, and to design the technology so that it addresses these needs.

In 2011, we designed and deployed a 1 μm wavelength SS-OCT retinal imaging system to OHSU, shown in **Figure 13 (A)**. This technology employed a commercially available, short-cavity swept laser (Axsun Technologies, Inc) which operated at 100 kHz A-scan rate [54]. The data acquisition was optically clocked enabling evenly spaced samples in wavenumber, so that the interferometric OCT data could be rapidly processed without requiring computationally costly resampling. The OHSU group, lead by Dr. David Huang, used this SS-OCT technology for their development of split-spectrum amplitude-decorrelation angiography (SSADA) algorithm for OCTA [4]. This algorithm was transferred to industry and has been integrated into the commercial Avanti RTVue-XR (Optovue, Inc.) ophthalmic imaging instrument. In 2014, we designed and deployed a second SS-OCT instrument to OHSU. This instrument was especially designed for anterior eye imaging and operated at 100 kHz A-scan rate with a long imaging range, shown in **Figure 13 (B)**. This system incorporated a novel optical clock doubling circuit, similar to that used in our PS-OCT studies, to double the imaging range of the system. Doubling the optical clock frequency enables both anterior surface of the cornea and posterior surface of the crystalline lens to be captured in a single image.

In 2013, we designed a similar 100 kHz SS-OCT retinal imaging system and deployed it to UPMC, **Figure 13 (C)**. The UPMC group, led by Dr. Joel Schuman, is using this technology for performing studies of glaucoma. The combination of high imaging speed and the enhanced penetration of 1 μm wavelength enables 3D OCT imaging of the lamina cribrosa structure of the optic nerve head. UPMC has published studies analyzing the structure of the lamina cribrosa and its relation to glaucoma [55, 56].

Our group has developed and deployed several systems to Dr. Duker's group at NEEC which is located across the Charles River in Boston. The system shown in **Figure 13 (D)** is a 91 kHz ultrahigh resolution SD-OCT instrument. The 3 μm axial resolution provided by this prototype instrument is higher than the standard 6–10 μm in commercial SD-OCT systems. Ultrahigh resolution enables visualization of the photoreceptor-RPE complex to analyze changes in the photoreceptor outer segments and RPE which occur in retinal diseases such as AMD. We have also developed a 100 kHz SS-OCT retinal imaging system for NEEC, shown in **Figure 13 (E)**, that parallels the systems deployed to the other collaborative sites. In November 2013, we developed and deployed an ultrahigh speed 400 kHz VCSEL SS-OCT retinal imaging system to NEEC, shown in **Figure 13 (F)**. In addition to structural imaging, this ultrahigh speed technology can perform wide field OCT angiography (OCTA) and acquire multiple, densely oversampled volumes per cardiac cycle for *en face* Doppler imaging of total retinal blood flow. These functional imaging protocols are currently used to image patients with ocular diseases such as AMD, diabetic retinopathy, and glaucoma in order to elucidate fundamental mechanisms of disease pathogenesis as well as to identify markers for improved diagnosis and progression monitoring.



Figure 13. OCT imaging instruments were developed and deployed to the ophthalmology clinics at multiple collaborator sites. (A) 100 kHz retinal and (B) anterior imaging SS-OCT systems at OHSU. (C) 100 kHz retinal SS-OCT system at UPMC. (D) 91 kHz ultrahigh resolution retinal SD-OCT, (E) 100 kHz retinal SS-OCT, and (F) 400 kHz retinal VCSEL SS-OCT at NEEC.

3.2 Handheld OCT

Although currently available commercial OCT systems have excellent image quality, these systems are relatively large and most are table mounted, limiting their use outside of ophthalmology or optometry settings. Development of a handheld OCT technology can enable OCT imaging of supine patients and children, as well as facilitate use in settings such as primary care, intraoperative, developing countries, and military medicine. Many retinal diseases are asymptomatic and thus go undetected until irreversible vision loss or impairment occurs [57, 58]. The rate of undetected retinal disease is especially high for minority communities in the US that do not have easy access to eye care [59, 60]. Early detection allows for early treatment and improvement of patient outcome [61, 62]. Portable OCT technology would also be advantageous for deployment in remote medical centers, such as in field hospitals to access ocular trauma and in third world countries that have limited access to diagnostic technologies. Assessment of OCT data can be performed remotely by trained specialists in reading centers.

To increase the portability of ophthalmic OCT systems, galvanometer scanners used in tabletop instruments have been adapted for handheld instruments in research [63-65] and commercial systems such as the Envisu (Biotigen) and iVue (Optovue). However, OCT beam scanning required two, orthogonally oriented galvanometer scanners encased in a bulky metallic mount for stability and heat dissipation. To reduce the size and weight of a handheld OCT instrument, MEMS scanning mirrors have been used in a handheld SD-OCT system at 70 kHz to generate 2D cross-sectional images for use in a primary care environment [66].

Our group demonstrated ultrahigh speed, swept source handheld OCT technology using a MEMS scanning mirror in combination with VCSEL based SS-OCT [67]. The handheld instrument combined multiple technologies to overcome many of the classic limitations of handheld imaging. First, we used a VCSEL light source to achieve an imaging speed of 350,000 A-scans a second to enable volumetric imaging of the retina. Volumetric imaging enables visualization of arbitrary cross sections and generation of *en face* images which can be used to precisely locate retinal features. Second, we utilized motion correction software to correct for both patient and operator motion artifacts [37]. Third, we used a MEMS scanning mirror instead of galvanometers to scan the beam and a plastic 3D printed enclosure to reduce the size and weight of the instrument. Finally, an iris camera, fixation target, and long axial imaging range were used to facilitate alignment and reduce imaging session time.

The system, **Figure 14**, had an imaging speed of 350,000 A-scans per second and operated at 1060 nm wavelength. The axial resolution was 10 μm in tissue with a 3.1 mm imaging range in tissue. Two different handheld enclosures were designed using 3D printing, **Figure 15**. The first design was a “power grip” style that has a handle for ambidextrous operation. The second design was a “camcorder” style, held from the side with a nylon strap supporting the back of the hand. A rotational adjustment was used to translate the ocular lens to compensate refractive errors of -12 to +6 Diopters. Both enclosures had identical optical components, including an iris camera and manually adjustable fixation target. The iris camera provided a video of the pupil and iris to aid in aligning the OCT beam through the pupil. The manual fixation target could move horizontally for OCT imaging of the macula or optic nerve head. The video from the iris camera and preview OCT scans were displayed on a 3.5 inch LCD screen on the device.

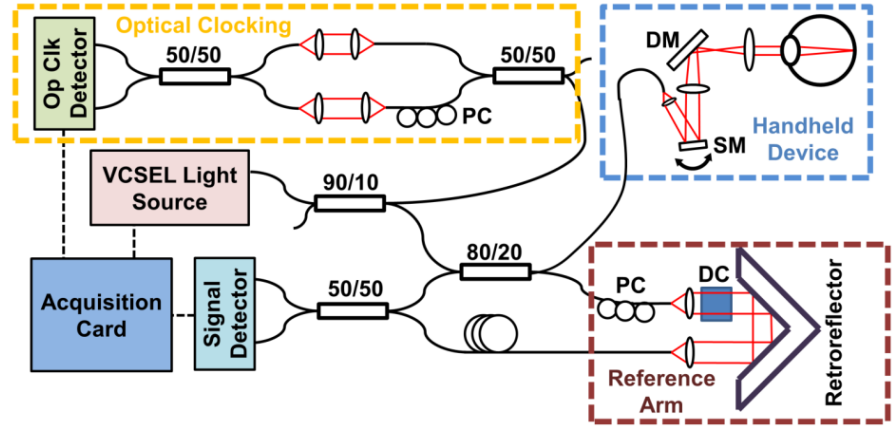


Figure 14. Swept Source OCT imaging engine using a high speed VCSEL light source at 1060 nm. A calibration MZI is used to generate an optical clock signal. MEMS scanning mirror (SM). Dichroic mirror (DM). Polarization controller (PC). Dispersion compensation glass (DC).

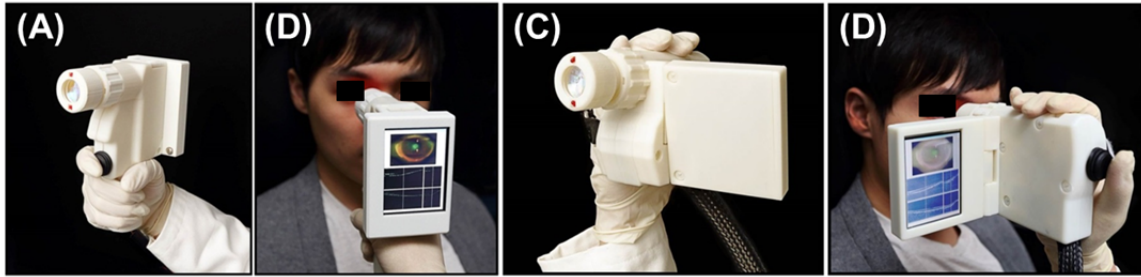


Figure 15. Photographs of the (A, B) power grip style and (C, D) camcorder style designs. The optical components inside both enclosures are identical.

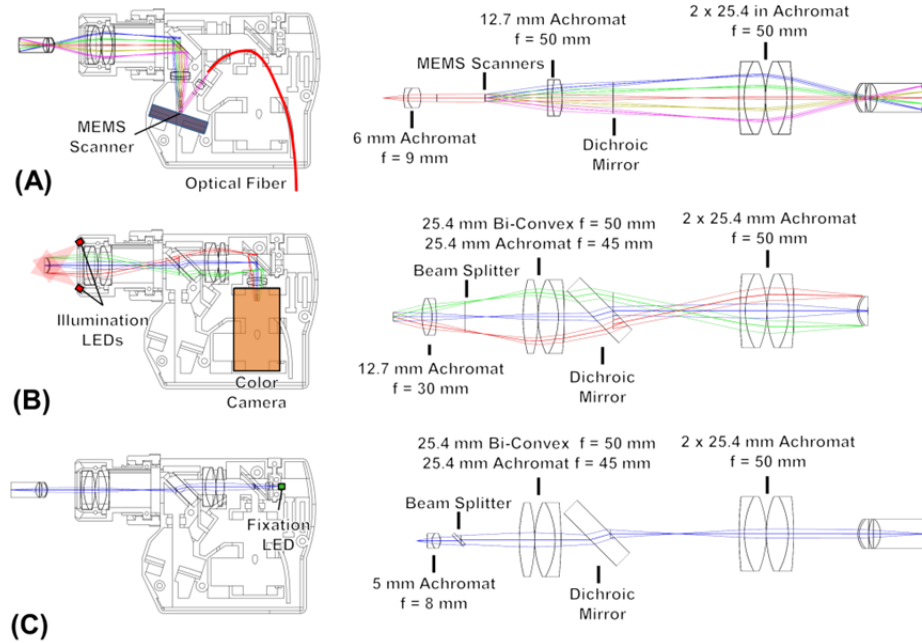


Figure 16. Internal optical layout of handheld OCT and unfolded optical design showing the (A) OCT 1060 nm optical path, (B) iris camera optical path, and (C) fixation target optical path.

Figure 16 shows the OCT (A), iris camera (B), and fixation target (C) optical pathways. A 2.4 mm diameter 2D gimbal-less tip-tilt MEMS mirror (Mirrorcle Technologies) was used to scan the OCT beam. Due to the low resonance frequency of the MEMS mirror, volumetric images were acquired by scanning the mirror sinusoidally in one direction and linearly in the other direction. Two orthogonally scanned volumes were acquired, motion corrected and merged using our software motion correction. **Figure 17** shows a 10 mm x 10 mm volumetric image taken with the handheld system. Two 1400 x 350 A-scan sinusoidal raster volumes were acquired in 1.4 seconds per volume. The two volumes were converted to 350 x 350 A-scan linear volumes and motion corrected to generate a merged 350 x 350 A-scan volume. This volume was centered between the fovea and optic nerve head by adjusting the fixation target. Since this wide field volumetric scan captures the macular and optic nerve head area, the operator does not need to image both areas separately.

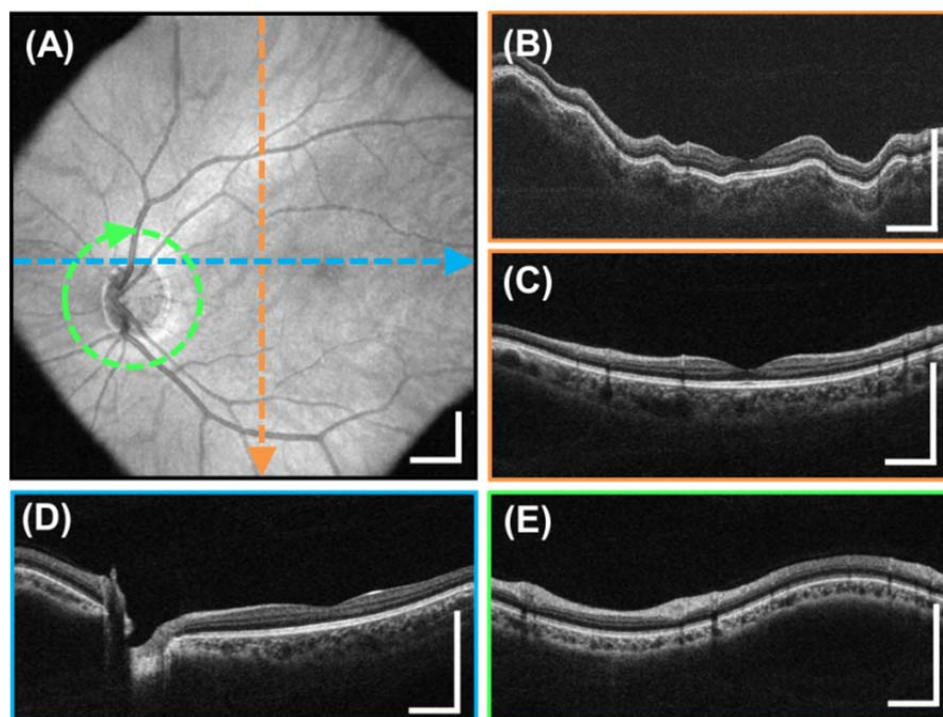


Figure 17. Hand held OCT imaging. Motion-corrected, wide field 10 mm x 10 mm, 350 x 350 A-scan volume generated from two volumes acquired in 1.4 seconds each. (A) En face OCT fundus image. (B) Original vertical cross-sectional image from the horizontal raster scanned volume. (C) Vertical cross-sectional image from the motion-corrected merged volume. (C, D) Colors indicate cross section locations on the fundus. (E) Interpolated 3.4 mm diameter circumpapillary scan extracted from motion-corrected volumetric data. Scale bars: 1 mm.

3.3 Wide Field Retinal Imaging

For volumetric OCT imaging, the A-scan sampling interval should be smaller than the illumination spot diameter in order to ensure optimal resolution in order to visualize focal pathology. Therefore, faster speeds are required to image wider areas, since the data acquisition times for retinal imaging are limited. The 400 kHz ultrahigh speed VCSEL swept source OCT technology enables much wider retinal imaging fields, while still maintaining comprehensive structural information [4]. **Figure 18** shows a 14 mm x 14 mm, 800 x 800 A-scan motion-

corrected volume of the retina generated from two orthogonally scanned volumes each acquired in ~3 seconds. Wide field imaging enables coverage of both the macula and the optic nerve head in a single data acquisition, simplifying workflow and reducing the time required to image patients.

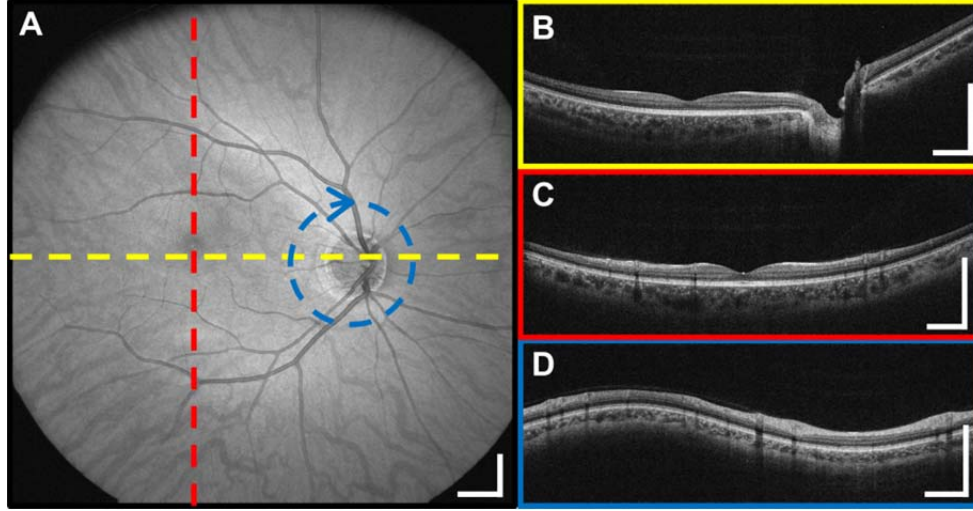


Figure 18. Wide field volumetric OCT imaging of the human eye. (A) OCT fundus image from a large 14 mm \times 14 mm, 800 \times 800 A-scan motion-corrected volumetric data set. (B-D) Arbitrary cross-sectional images can be extracted from volumetric data. The data contains comprehensive structural information on both retina and choroid. Scale bar: 1 mm.

3.4 Long Range Imaging of the Anterior Eye and Full Eye Length Imaging

Utilizing the long imaging range and adjustability of the MEMS-tunable VCSEL, we developed prototype multi-modal SS-OCT technology that can be adapted for visualizing the human retina, the anterior segment of the eye, and the full eye length, with minimal hardware modification in the patient interface [4]. For retinal imaging, the A-scan rate was set to 580 kHz with 1.9 mm imaging range in tissue. For imaging the anterior segment, the A-scan rate was set to 100 kHz with 13.6 mm imaging range. In order to achieve 38 mm imaging range to cover the full eye length, the A-scan rate was further reduced to 50 kHz. **Figure 19** shows a 3D rendering and representative cross sectional image from an OCT volume of the entire anterior segment from the anterior cornea to the posterior surface of the ocular lens. Previously, Visualizing the entire anterior segment with OCT has been challenging because other SS-OCT light sources have limited coherence lengths and limited imaging range.

The measurement of the optical surfaces of the anterior eye is essential for monitoring refractive or cataract surgery procedures such as laser-assisted *in situ* keratomileusis (LASIK), photorefractive keratotomy (PRK), phototherapeutic keratotomy (PTK), intracorneal rings, astigmatic keratotomy, lamellar keratoplasty and intraocular lens implants [68-71]. The ultrahigh imaging speed and long imaging range of VCSEL SS-OCT in combination with software motion correction enable *in vivo* anterior segment biometry. **Figure 20** shows examples of biometric measurements of the corneal and the crystalline lens surfaces. Image distortion caused by light refraction was corrected using a 3D ray-tracing algorithm. Advanced motion correction methods are crucial for performing keratometry with OCT because mapping optical power requires accurate measurement of the second derivative of the surface contour.

The unprecedented imaging range of the VCSEL also enables full-eye OCT, as shown in **Figure 21**. Full-eye OCT spans the full eye length from the cornea to the retina, enabling precise measurement of intraocular distances [72]. We have investigated the measurement reproducibility of the full-eye OCT ocular biometry, demonstrating good reproducibility and correlation with commercially available optical and ultrasonic biometers [51].

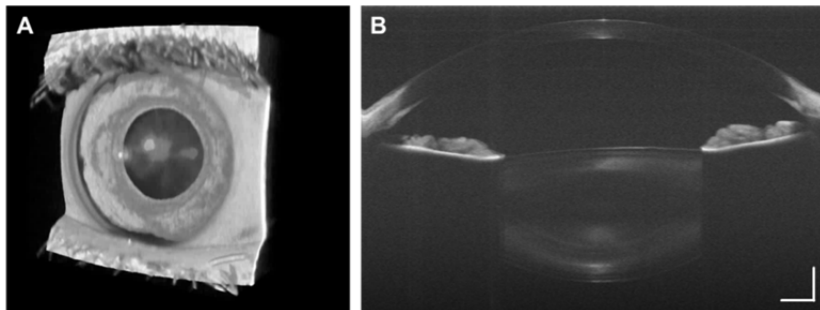


Figure 19. Anterior segment imaging with high speed, long range SS-OCT. (A) Motion-corrected volume comprising 400×400 A-scans over a $15 \text{ mm} \times 15 \text{ mm}$ area. (B) Representative central cross-sectional image from the volumetric data set.

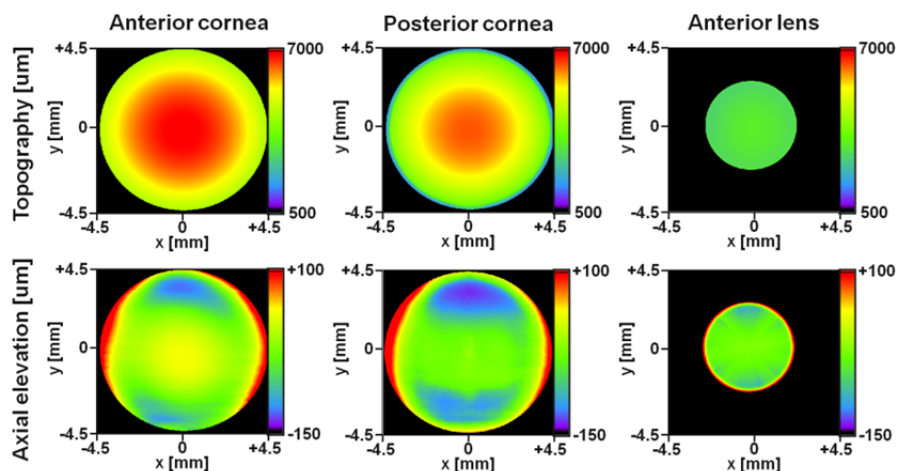


Figure 20. Examples of anterior eye biometry. Top row shows the topographic map of the anterior chamber surfaces and the bottom row shows the residual elevation from spherical fit.

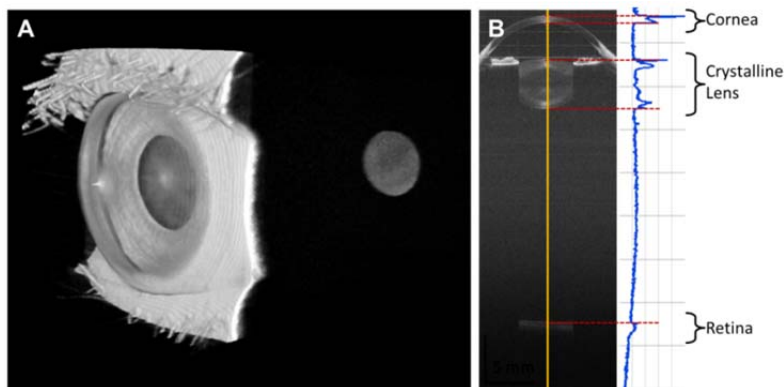


Figure 21. Full-eye OCT can visualize the anterior and posterior eye in a single volume. (A) Full-eye OCT volume with 500×500 A-scans, $15 \text{ mm} \times 15 \text{ mm}$ area and 42 mm imaging range. (B) Central cross section and averaged intensity profile of extracted central A-scans shows the axial distances of ocular surfaces.

3.5 OCT Angiography of the Retina and Choroid

Current Techniques for Visualizing Retinal and Choriocapillaris Microvasculature

The retina and choroid, which are the two blood supplies to the eye, are thought to play an important role in a variety of ocular diseases, including age-related macular degeneration (AMD) and diabetic retinopathy. Traditionally, ocular vasculature has been visualized, both in the research setting and clinically, using fluorescein angiography (FA) and indocyanine green angiography (ICGA) which require intravenous dye injection. While FA can visualize retinal vasculature, visualization of the choriocapillaris/choroid using FA is challenging because the blue-green excitation wavelength of fluorescein is partially absorbed by the macular xanthophyll and retinal pigment epithelium (RPE), and ~20% of the injected fluorescein does not bind to albumin and leak out of the choriocapillaris fenestrations, creating diffuse hyperfluorescence which obscures vasculature [73]. In contrast, indocyanine green angiography (ICGA) enables visualization of choroidal circulation because its near infrared excitation wavelengths are not as readily absorbed by the macular xanthophyll and RPE, and ~98% of the injected indocyanine green is bound to plasma protein, preventing it from leaking out of the choriocapillaris fenestrations [73]. ICGA has also been shown to be capable of visualizing the choriocapillaris circulation [74]. However, since ICGA is not depth resolved, the task of separating choriocapillaris blood flow from that of deeper choroidal vasculature is complicated and may only be possible if it is assumed that the blood flow velocity of the larger choroidal arteries is small compared to the choriocapillaris [74, 75]. In addition to the limited ability of FA and ICGA to image the choriocapillaris, both require the injection of exogenous dyes, making the imaging procedure invasive and time consuming.

OCT angiography (OCTA) can generate three-dimensional microvascular angiograms *in vivo*, rapidly and without requiring injection of exogenous dyes [7-14, 76]. OCTA is based on the fact that stationary tissue generates a time-independent B-scan image, while flowing blood motion produces time-dependence in the B-scans. If repeated B-scans of stationary tissue are acquired at the same location over time, then each B-scan will be identical. However, if there is motion, for example flowing erythrocytes, then repeated B-scans will differ. These differences can be quantitatively represented by a decorrelation signal, where large differences in image features (corresponding to fast flow) generate high decorrelation and small differences (corresponding to slow flow) generate low decorrelation. A number of different techniques for quantitating the decorrelation signal have been demonstrated [5, 10, 77]. Since OCT angiograms are obtained from repeated intensity B-scans, they are intrinsically co-registered with structural data. OCTA therefore enables simultaneous assessment of structure and microvasculature.

Compared with conventional dye-based angiography techniques, OCTA offers several important advantages. First, OCTA does not require the injection of exogenous dyes and is noninvasive. Second, unlike dye-based angiography, OCTA is fast (typical acquisition time < 4 seconds), and can be performed repeatedly, potentially during every patient visit. Third, OCTA enables depth resolved imaging of both the retinal and choroidal vasculature. Taken together, these advantages make OCTA a powerful technique for studying retinal and choroidal microvasculature, particularly in longitudinal clinical studies.

Development of SS-OCT Angiography using the VCSEL Swept Light Source

Our group has demonstrated ultrahigh speed swept source OCT (SS-OCT) for ophthalmic applications using VCSEL technology and developed a phase-stabilized prototype system with a 400 kHz A-scan rate, approximately 5-10 times faster than standard commercial systems [5]. The instrument used a VCSEL centered at ~ 1050 nm wavelength with a ~ 80 nm tuning range. OCT signals are sampled with a high-speed digitizer externally clocked at up to ~ 1.1 GHz using a Mach-Zehnder interferometer calibration signal yielding an imaging range of ~ 2.1 mm in tissue. Imaging at ~ 1 μ m wavelengths has the advantage over 840 nm wavelength light sources in current commercial SD-OCT systems in that it is less sensitive to attenuation by ocular opacities and allows deeper light penetration into tissue, such as the RPE and choroid. The ultrahigh speed is especially advantageous for imaging the choriocapillaris, which has very features requiring a high A-scan sampling density.

Demonstration of SS-OCT Angiography Imaging in Normal Subjects

Our group demonstrated *in vivo* OCTA imaging of the choriocapillaris and choroidal microvasculature in a cohort of normal human subjects using OCTA [78]. The vascular patterns of the OCTA were shown to be consistent with those seen in previous histological and electron micrograph studies (**Figure 22**) [17, 79].

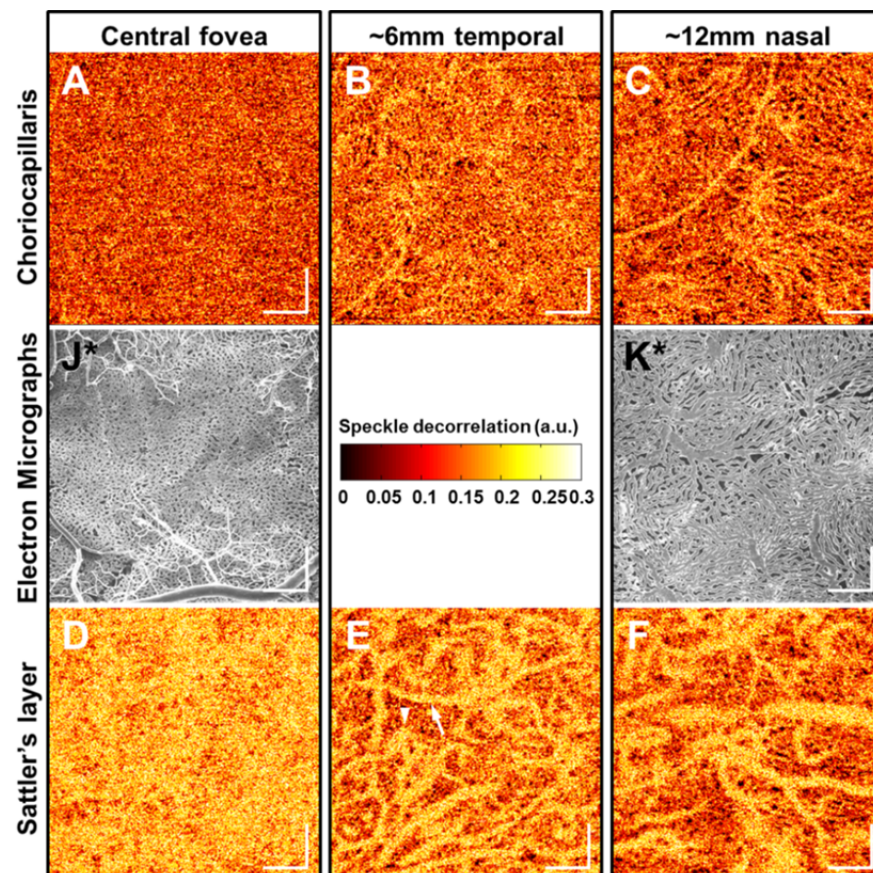


Figure 22. 1.5 mm x 1.5 mm *en face* OCT angiograms at three different fundus locations. (A, D, G) OCT angiogram of the choriocapillaris, OCT angiogram of the Sattler's layer, and *en face* OCT intensity image (slice) corresponding to the choriocapillaris layer, respectively, at the central fovea. (B, E, H) OCT angiogram of the choriocapillaris, OCT angiogram of the Sattler's layer, and *en face* OCT intensity image (slice) corresponding to the choriocapillaris layer, respectively, at 6 mm temporal to the central fovea. The

arrowhead indicates venules and arrow arteriole in (E). (C, F, I) OCT angiogram of the choriocapillaris, OCT angiogram of the Sattler's layer, and *en face* OCT intensity image (slice) corresponding to the choriocapillaris layer, respectively, at 12 mm nasal to the central fovea. (J, K) Electron micrographs of corrosion casts reproduced from Olver et al. with permission. Scale bars: 250 μ m.

Exudative AMD

Exudative age-related macular degeneration (AMD), a pathology characterized by choroidal neovascularization (CNV), is a leading cause of vision loss and impairment in developed countries. Working in collaboration with Dr. Jay Duker at the NEEC, we performed a clinical study of OCTA imaging and analysis of 17 eyes with exudative AMD with active CNV (15 patients; 79.7 ± 8.3 years old). Enrollment is ongoing. Choroidal neovascularization was clearly visualized in 16 of the 19 eyes with exudative AMD. In all of the 16 eyes in which CNV was visualized, the CNV was located above regions of severe choriocapillaris alteration. In 14 of these eyes, the CNV lesions were surrounded by regions of choriocapillaris alteration. **Figure 23** shows OCT and OCTA images from an 87 year old treatment naive exudative AMD patient with a minimally classic CNV. All images were obtained from a single volumetric scan. The results of this study suggest mechanisms for CNV development and its link to choriocapillaris alterations. The study also suggests a role for OCTA in the identification of CNV for determining treatment of exudative AMD. The results of our exudative AMD studies were recently featured on the cover of Ophthalmic Surgery, Lasers and Imaging Retina, Nov/Dec 2014 [1].

Dry AMD

While the most severe vision loss has historically been associated with the exudative or wet form of AMD which is characterized by the formation of choroidal neovascularization (CNV), the atrophic or dry form of AMD which is characterized by geographic atrophy (GA), is likely to become the most common cause of severe loss in the future. This shift is largely due to the success of vascular endothelial growth factor inhibitors. We have performed a clinical study of OCTA imaging and analysis of 12 eyes with non-exudative AMD with GA (7 patients; 75.9 ± 6.1 years old). Enrollment is ongoing. In 12/12 eyes OCTA revealed evidence of CC atrophy within the regions of GA. In 10/12 eyes OCTA showed CC flow impairment extending beyond the margin of GA. In 14/16 eyes choriocapillaris alteration was observed in regions extending beyond the CNV lesion. **Figure 24** illustrates the ability of OCTA to examine the choriocapillaris in a 75 year old atrophic age-related macular degeneration (AMD) patient. These studies also investigated the role of OCTA imaging parameters in determining the sensitivity of OCTA to low flows and provided a method to differentiate choriocapillaris flow impairment from atrophy. More extensive cross-sectional studies are ongoing and are needed to investigate the potential of OCTA for monitoring disease progression and response to therapy. Recruitment of age matched normal subjects will be especially important in order to separate effects of normal aging from alterations due to disease.

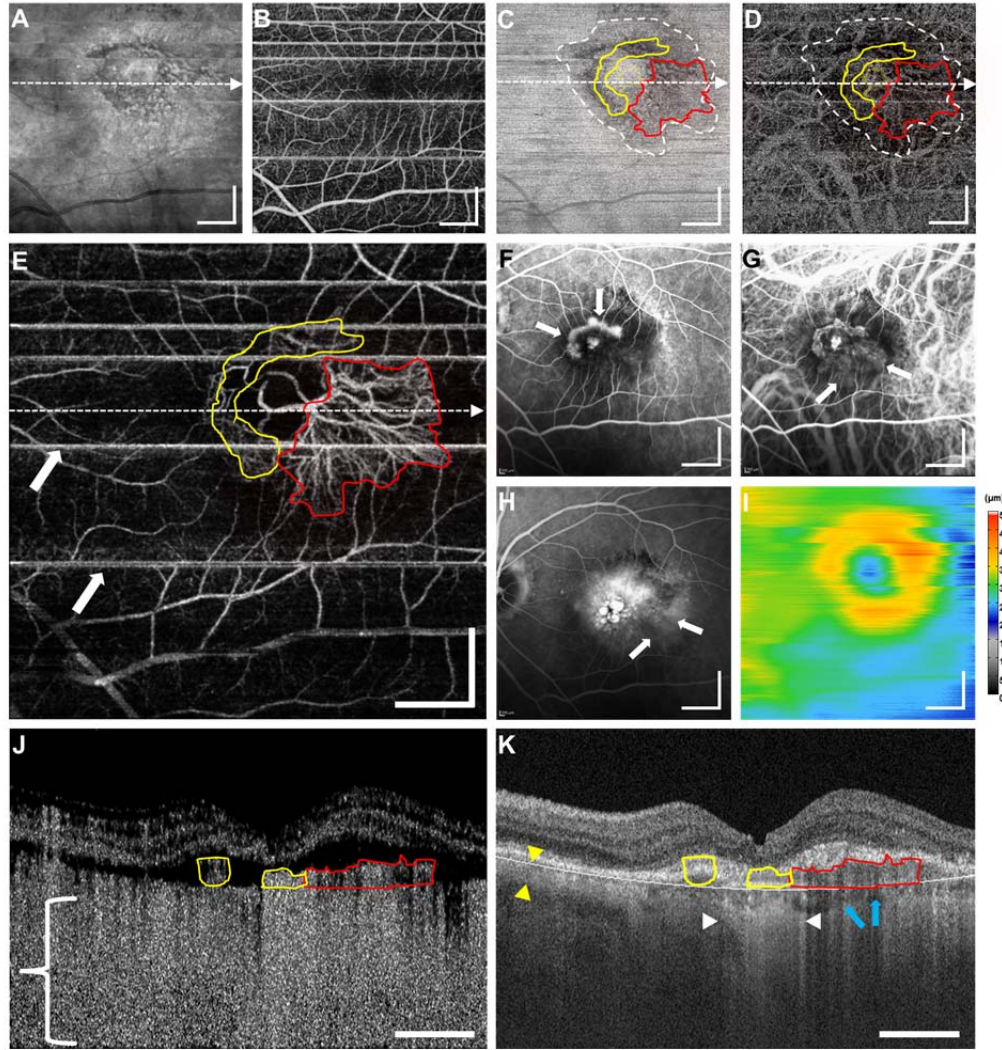


Figure 23. An 87 year old patient with a CNV lesion exhibiting both occult and classic components. (A) OCT intensity projection. (B) *En face* OCTA projection showing retinal vasculature. (C) *En face* slice of the OCT intensity volume at the depth of the choriocapillaris. The white dashed contour shows an area of lower intensity. (D) *En face* slice of the OCTA volume at the depth of the choriocapillaris. (E) *En face* projection of the OCTA volume through the depths spanned by the CNV. The red shading corresponds to the occult components of the lesion while the yellow shading corresponds to the classic components. The arrows point to motion artifacts that appear as horizontal lines through the image. (F) Early phase FA. Arrows point to the classic component. (G) Early phase ICGA. Arrows point to the occult component. (H) Late phase FA. Arrows point to area of stippled hyperfluorescence. (I) OCT retinal thickness map. (J, K) OCT intensity and OCTA cross-sections, respectively, corresponding to the white dashed horizontal lines in (E). The bracket in (J) roughly spans the depths in which the OCTA B-scan is uninterpretable due to shadowing from the choriocapillaris/choroidal vasculature. The yellow arrows in (K) indicate the choroidal thickness away from the lesion; the white arrows show an area of shadowing; and the blue arrows correspond to a region of choroidal atrophy. All OCT images are from a 6 mm × 6 mm area and all scale bars are 1 mm. All OCT and OCTA images were generated from a single volumetric scan.

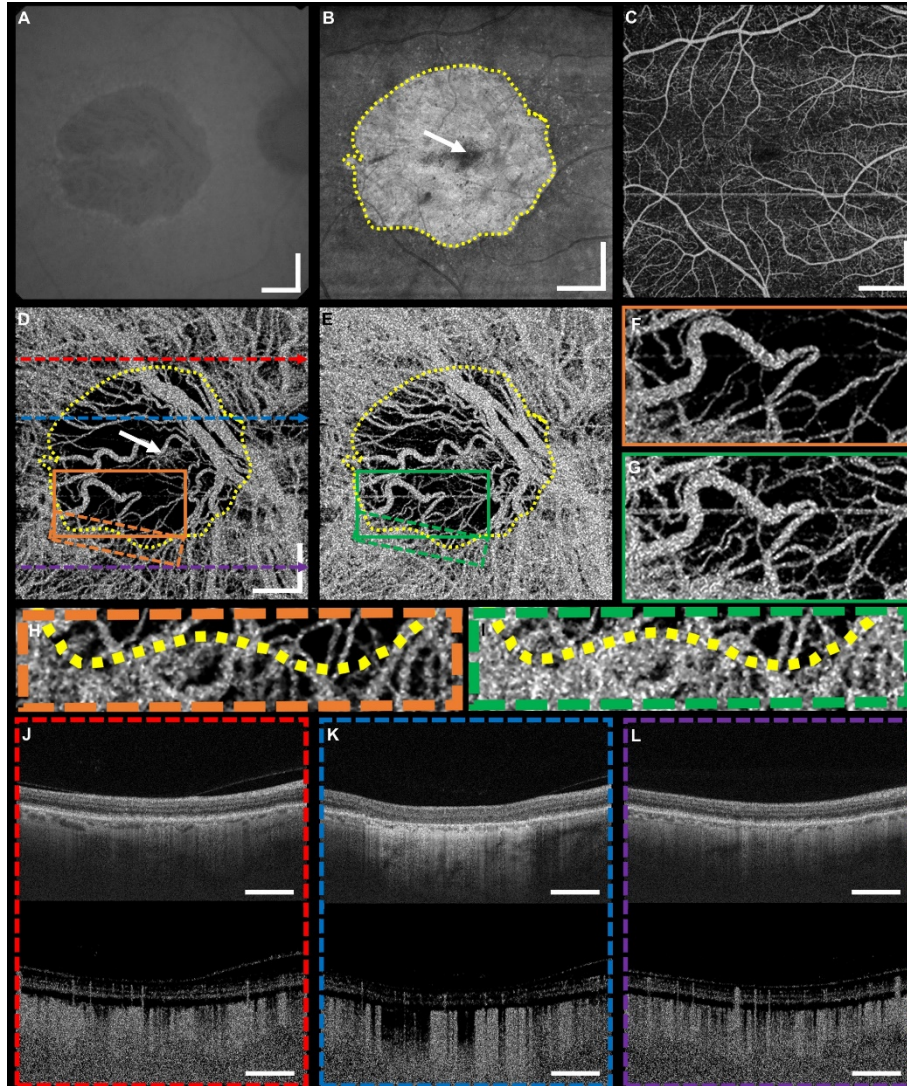


Figure 24. Fundus autofluorescence (FAF) image, OCT and OCTA in a 75 year old atrophic age-related macular degeneration (AMD) patient with a visual acuity of 20/20. The FAF (A) and the *en face* OCT (B) clearly show the region of GA, outlined by the yellow dashed line in the *en face* OCT. The GA region appears lighter due to increased light penetration into the choroid caused by RPE atrophy. The white arrow shows the region of foveal sparing. (C) An OCTA of the retinal microvasculature, generated by mean projection of the OCTA volume between the inner limiting membrane (ILM) and retinal pigment epithelium (RPE). The retinal vasculature appears normal. (D) An *en face* OCTA of a 4.4 μm thick slab at the level of the choriocapillaris (CC) using a ~ 7.5 ms interscan time. The yellow dashed contour from (B) is superposed, and severe CC alteration appears within this contour. Flow in the area of foveal sparing, indicated by the yellow arrow, is also visible. Severe CC alteration is evident outside the GA margin. (E) An *en face* OCT of the same 4.4 μm thick slab at the level of the CC as in (D), using a ~ 15 ms interscan time which has increased sensitivity. Magnified views of the solid orange and green boxes of (D) and (E) are shown in (F) and (G), respectively. Note that some choroidal vessels that are not visible in (F) become visible in the high sensitivity image (G). Magnified views of the dashed orange and green boxes of (D) and (E) are shown in (H) and (I). OCT intensity (top) and OCTA (bottom) B-scans through the red, blue and purple horizontal dashed lines in (D) are shown in (J), (K) and (L), respectively. All scale bars are 1 mm.

Diabetic Retinopathy

Both retinal and choroidal blood circulation are believed to be altered in diabetic retinopathy (DR), a leading cause of vision loss or impairment in developed countries. There are multiple

vascular abnormalities that are potential early markers for DR. Early changes in non-proliferative diabetic retinopathy (NPDR) include microaneurysms, foveal avascular zone (FAZ) enlargement, and capillary dropout. We have performed a clinical study of OCTA imaging and analysis of 9 eyes with proliferative diabetic retinopathy (PDR), 29 eyes with non-proliferative diabetic retinopathy (NPDR), and 53 diabetic eyes without retinopathy. Enrollment is ongoing. **Figure 25** illustrates the ability of OCTA to visualize microvascular changes of a 55 year old diabetic patient with PDR. Preliminary results suggest that microvascular changes appear in patients without overt retinopathy.

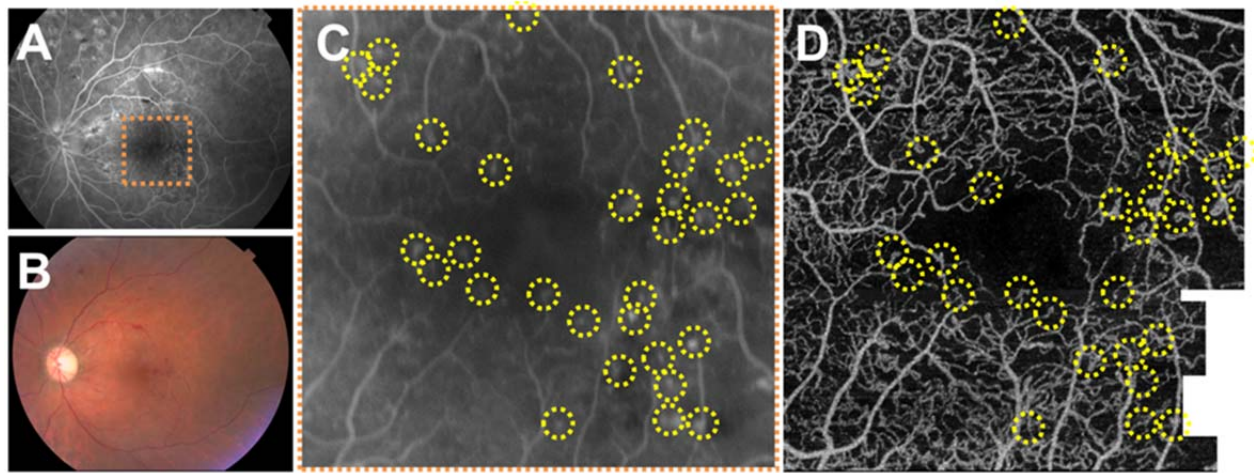


Figure 25. (A) FA, (B) fundus photograph, (C) enlarged view of the FA, and (D) OCT angiogram from a 55 year old diabetic patient with PDR. The enlarged area indicated by the orange square in (A) is shown in (C). The OCT angiogram in (D) show high correspondence to the FA in (C). Many of the microaneurysms indicated by the yellow circles appear as hyperfluorescent spots in the FA while they appear as abnormal capillary loops in the OCT angiogram. OCT angiogram acquired from a 3 mm × 3 mm area.

3.6 En Face Doppler OCT Measurement of Total Retinal Blood Flow

Measurement of Total Retinal Blood Flow

Measurement of retinal blood flow *in vivo* is an important research area in ophthalmic imaging since alterations in retinal perfusion are suggested to play an important role in pathogenesis of ocular diseases such as glaucoma [80-83] and diabetic retinopathy [84-87]. Quantitative assessment of total retinal blood flow (TRBF) enables objective comparison of retinal circulation among different subjects and simplifies longitudinal tracking of changes associated with disease progression. TRBF measurement can provide useful information for investigating ocular pathophysiology as well as for identifying potential early diagnostic markers.

Conventional Techniques of TRBF Measurement

Multiple imaging modalities such as video fluorescein angiography, laser speckle flowgraphy, laser Doppler velocimetry, scanning laser Doppler flowmetry, and ultrasound color Doppler imaging can be used to investigate quantitative retinal blood flow [88-94]. However, objective measurement of TRBF remains challenging. Video fluorescein angiography and laser speckle flowgraphy cannot directly measure blood flow velocity, but yield indirect metrics such as arteriovenous passage time and mean blur rate. Scanning laser Doppler flowmetry (e.g. Heidelberg Retina Flowmeter, Heidelberg Engineering, Heidelberg, Germany) can map the flow

velocity component along the probe beam direction over a two-dimensional scan area; however, the absolute flow velocity is required for quantitative flow rate measurement. Ultrasound color Doppler imaging can measure flow velocity at different tissue depths but has a ~200 μm spatial resolution which is insufficient to visualize detailed structure of the central retinal vasculature, complicating accurate blood flow calculation.

Among these techniques, bidirectional laser Doppler velocimetry (BLDV) combined with fundus photography is one of the most well suited methods for quantitative TRBF measurement. This technique measures maximum absolute flow velocity in a vessel by detecting the Doppler frequency shifts of the light backscattered in two different directions. Blood flow in the vessel is calculated as the product of the maximum absolute flow velocity and the effective vessel cross-sectional area, estimated from the vessel diameter measured in a fundus photograph. TRBF is then calculated as the sum of the blood flow in major retinal vessels near the optic disc. BLDV measurement of TRBF was validated in healthy subjects [95-98] and used for investigating TRBF in diabetic patients [99-102]. However, the calculation of effective vessel cross-section area relies on the assumption that vessel shapes are round and blood flow velocity follows a parabolic profile. This assumption can be inaccurate in some subjects and may result in flow measurement errors. Moreover, measurement times can be preclusive because individual major retinal vessels must be measured separately, requiring 20 to 55 minutes per eye [103]. Due to this limitation, the number of patients in most TRBF studies using BLDV has been limited.

En face Doppler OCT

Fourier-domain OCT has enabled phase-sensitive imaging methods such as Doppler OCT, which promises simpler and more robust measurements of TRBF using depth-resolved vessel structure and Doppler velocity [104]. Conventional Doppler OCT techniques require measuring the angle of blood vessel, because Doppler OCT detects only the axial velocity component. Previous Doppler OCT methods have used double circumpapillary scans that intercept central retinal vasculature to detect the axial velocity and measure the Doppler angle, the angle between the OCT beam and blood flow direction for each major retinal vessel [105, 106]. However, this technique was sensitive to small errors in Doppler angles, making automatic measurements challenging. Our collaborators from Dr. David Boas' group at MGH developed a new *en face* Doppler OCT technique for measuring blood flow in the small animal brain, which does not require angle measurements [18]. *En face* Doppler measures blood flow by volumetric raster scanning the vessels and integrating the axial velocity components in an *en face* plane. The *en face* velocity can be integrated to obtain the total flow without requiring the Doppler angle. Our group used a 200 kHz SS-OCT instrument to demonstrate that human total retinal blood flow can be measured by volumetrically scanning a small area at the optic disc [107]. This is an example of translating imaging techniques developed in the brain to the retina and shows the synergy between methods in brain science and ophthalmology.

En face Doppler OCT with High-Speed OCT Technology

Our group continued development *en face* Doppler OCT measurement techniques using ultrahigh speed SD-OCT and SS-OCT to resolve pulsatile retinal blood flow and improve measurement reproducibility in small animals and human subjects [5, 108]. Small animal studies are particularly challenging because heart rates in rats can be 300 beats per minute. Ultrahigh speed *en face* Doppler OCT enabled volume acquisition rates of 55 Hz in small animals using SD-OCT and 7.6 Hz in humans using SS-OCT. These volume acquisition rates are several times

faster than the normal heart rates in small animals and humans, enabling the acquisition of multiple flow measurements per cardiac cycle. **Figures 26 (B-F)** show an example of pulsatile retinal blood flow measurement in a normal human subject performed with an ultrahigh speed swept source OCT prototype using a 1 μm wavelength VCSEL light source at a 400 kHz A-scan rate. Each flow value measurement in **Figure 26 (B)** requires a 3D OCT volume.

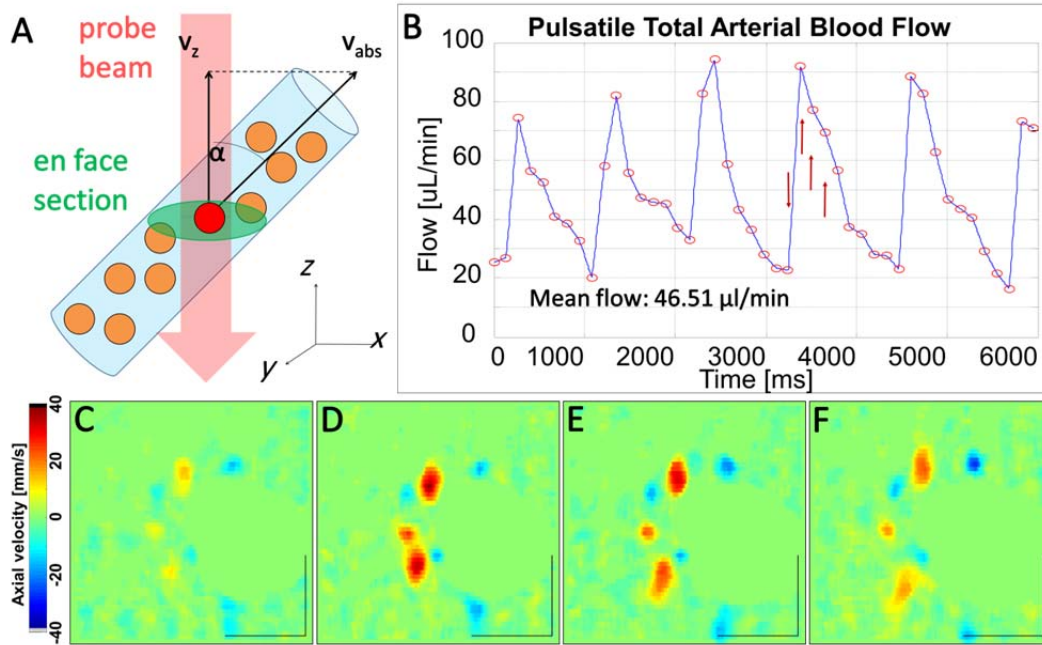


Figure 26. *En face* Doppler OCT provides a robust and fully automatable measurement of total retinal blood flow. (A) Flow is measured in *en face* plane avoiding the need to measure the Doppler angle α . (B) Ultrahigh speed OCT at 1050 nm enables repeated volumetric imaging (750 x 60 A-scan volumes at 7.6 Hz rate) to measure pulsatile flow. (C-F) Pulsatile flow in *en face* plane of central retinal vasculature. Scale bar: 500 μm .

Synchronized *En face* Doppler OCT with Pulse Oximetry Cardiac Gating

In order to enable larger scale clinical studies, we developed a cardiac gating method for enhanced sampling of blood flow pulsatility in *en face* Doppler with commercially available 100 kHz A-scan rate SS-OCT technology. A pulse oximetry plethysmogram was obtained from subject's earlobes and was connected to the OCT system to synchronize the start of a multiple volume OCT acquisition sequence with the subject's cardiac cycle. Total flow was measured using three synchronized, multiple volume acquisitions. Highly repeatable mean total retinal blood flow measurement with fully automatic processing was made possible using specialized segmentation algorithm and retrospective correction of cardiac gating. In a repeatability study of mean total retinal blood flow measurement on 10 healthy young subjects, we observed an improvement from 8.0% median coefficient of variance (COV) to 4.9% COV using cardiac gating. In the same study, ultrahigh speed asynchronous acquisition at 400 kHz A-scan rate and 7.6 Hz volume rate yielded median COV of 6.1%. These results demonstrate that the simple addition of pulse oximeter can enable repeatable measurement of total retinal blood flow in the clinic using commercially available OCT imaging speeds.

Clinical Studies of Total Retinal Blood Flow

In an ongoing clinical study at NEEC using the 400 kHz prototype SS-OCT instrument, we measured total retinal blood flow in 18 eyes with non-proliferative diabetic retinopathy, 4 eyes with proliferative diabetic retinopathy, 16 diabetics without clinically evident retinopathy, 21 eyes with primary open-angle glaucoma, and 3 eyes with normal tension glaucoma. The study is ongoing, however preliminary results suggest that patients with primary open-angle glaucoma exhibit lower mean retinal blood flow than normal subjects. The mean flow difference between normal eyes and eyes with primary open-angle glaucoma was not large compared to the variation inside each group, suggesting that the statistical significance of the mean flow difference has to be further tested. In eyes with diabetic retinopathy, blood flow had a wide range of variation, occasionally exhibiting both lower [92-94] and higher [87, 99, 100] flows than the normal range. Previous studies in diabetic retinopathy have also reported both an increase and decrease in blood flow, depending on the severity of the disease. Therefore, further investigations involving detailed classification of retinopathy severity and its correlation with blood flow alteration are important.

4. Brain Imaging

4.1 Introduction to OCT for Neuroscience Applications

In collaboration with Dr. David Boas at Martinos Center of Biomedical Imaging, Massachusetts General Hospital, Harvard Medical School, we have developed advanced OCT technologies for neuroscience applications. Many of these methods can be translated to fundamental and clinical research in ophthalmology. These studies are also relevant for investigating the pathogenesis of traumatic brain injury (TBI), a problem of direct military relevance. Dr Boas's group has extensive infrastructure for Magnetic Resonance Imaging as well as OCT and a track record of collaborations with neurologists specializing in brain science, neurovascular coupling, brain trauma, stroke and migraine.

Optical imaging methods have had a significant impact on the field of neuroimaging over the past 20 years. Optical imaging is now widely used in studies of cerebrovascular and cellular physiology and pathology. While macroscopic methods using diffuse light (optical intrinsic signal imaging [109], laser Doppler imaging [110], laser speckle imaging [111], diffuse optical imaging [112], and laminar optical tomography [113]) provide relatively large fields of view but with spatial resolutions of hundreds of microns to millimeters, microscopic methods (two photon and confocal microscopy) enable micron-scale resolutions. Two-photon microscopy [114], in particular, is widely used in structural and functional imaging at the cellular and subcellular levels. However, two-photon microscopy has imaging speed, penetration depth, and field of view.

OCT has a unique combination of high imaging speed, penetration depth, field of view, and resolution; and therefore occupies an important niche between macroscopic and microscopic optical imaging technologies. OCT is uniquely capable of investigating important questions in neuroscience that are either difficult or impossible to address with the above techniques. Relative to the optical imaging technologies currently used for neuroscience research, OCT has several advantages: 1. faster volumetric imaging rates, 2. greater depth penetration with microscopic resolution, 3. quantitative measurements of tissue dynamics (red blood cell and intra-cellular organelle dynamics), and 4. the ability to use intrinsic contrast, rather than exogenous fluorescent markers.

During the previous funding cycle, we developed a powerful array of OCT methods for *in vivo* imaging of vascular and cellular dynamics in living animal brains. Specifically, we developed and validated Doppler algorithms for absolute CBF measurements in arteries and veins, which do not require measuring the vessel Doppler angles [18]. We also developed rapid volumetric imaging of blood perfusion patterns (i.e., angiograms) with OCT [115], which enables visualization of perfusion not only in arteries and veins, but also in capillaries. These technologies were combined and applied for a study of how CBF is affected by ischemic stroke in animal models [116]. We then integrated OCT with dynamic light scattering for microscopic imaging of tissue dynamics (DLS-OCT) [117]. This technology enabled us to simultaneously obtain 3D maps of the axial and transverse flow velocities and diffusion coefficient, enabling *in vivo* monitoring of not only blood perfusion, but also intra-cellular organelle motility within individual cells [118]. Finally, we developed OCT techniques to quantitatively measure blood flow within the capillary network. We discovered that individual RBC passages can be captured by dynamic OCT imaging and utilized to measure the RBC speed, flux and density over hundreds of capillaries [119]. These OCT technologies developed for neuroimaging in the previous funding cycle lead to technical advances that will enable us to study a range of questions which could not be addressed with existing technologies. This series of advances will also enable a number of novel experiments investigating neurovascular coupling, interpretation of human fMRI data, and cerebrovascular pathologies including those related to brain trauma. These advances, though developed for neuroimaging, can be translated to other fields such as retinal imaging or tumor biology.

4.2 Quantitative Measurements of Absolute Cerebral Blood Flow (CBF)

In the normal brain, cerebral blood flow (CBF) is regulated to satisfy metabolic demand determined by brain activity. CBF is required for the supply of oxygen and nutrients and the removal of metabolites and heat. Alterations in CBF may contribute to the pathogenesis of stroke, trauma, and Alzheimer's disease [120]. The gold standard for determination of regional blood flow is autoradiography. Although autoradiographic methods provide three-dimensional spatial information, they cannot assess the temporal evolution of CBF changes [121]. Therefore, studies of disease progression or response to treatment using intra-animal comparisons cannot be performed, limiting the utility of this method.

Methods of flow measurement based on magnetic resonance imaging [122] and positron emission tomography [123] provide spatial maps of CBF, but are limited in their temporal and spatial resolution. Two-photon microscopy can calculate both transverse velocity and linear density of RBCs [124], which may be combined to calculate RBC flux. However, the determination of CBF requires knowledge of the flow profile as well as vessel orientation, which can be difficult to measure. Scanning laser Doppler techniques can be used to obtain spatially-resolved relative CBF images by moving a beam across the field of interest [125]. Laser speckle imaging [126] has recently been applied for high spatiotemporal resolution relative measurements of CBF [111]. However, it is difficult to relate correlation times (laser speckle) or the width of the power spectral density (laser Doppler) to absolute velocities and flow of red blood cells, because the number of moving particles that the light interacts with and their orientations are unknown [127]. Doppler OCT overcomes many of the limitations of these aforementioned optical techniques by using path delay to gate out multiply scattered light [104, 128-130]. Using "coherence gating" [131], OCT enables measurement of velocity averaged over well-defined volumes, determined by the spot size in the transverse direction and coherence

length in the axial direction. Thus, Doppler OCT avoids the limitations associated with laser Doppler and laser speckle imaging.

The MGH group has developed methods and algorithms for the quantification of absolute CBF using Doppler OCT. **Figure 27 (B, C)** show an *en face* image of the z projection of velocity in the cortex at the depths of 100 μm and 25 μm , respectively. As shown in **Figure 27 (A)**, by integrating the flow profile over a vessel cross-section, it is possible to obtain the flow through that vessel. Notably, this method does not require the explicit measurement of the vessel angle relative to the probe beam. Using this *en face* Doppler OCT flow measurement, we compared the results of OCT flow measurements to measurements using the gold standard of hydrogen clearance [132]. The results are shown in **Figure 27 (C)** and demonstrate that *en face* Doppler OCT absolute blood flow measurements correlate with hydrogen clearance absolute blood flow measurements.

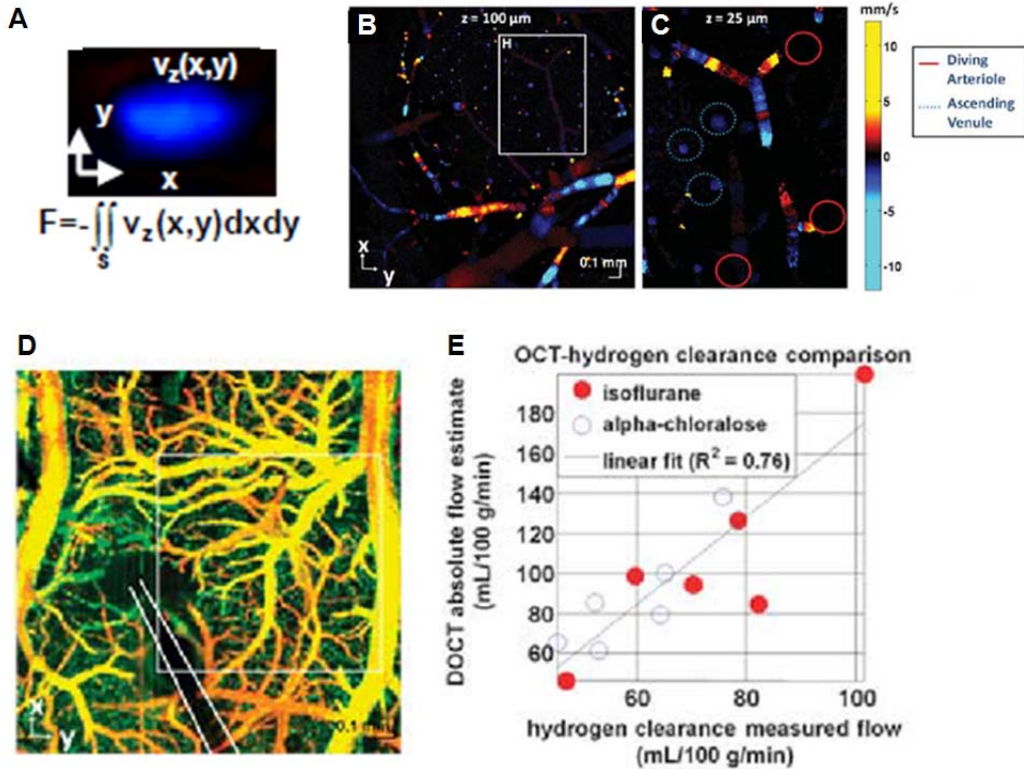


Figure 27. Doppler OCT for the quantitative study of cerebrovascular physiology. (A) *En face* Doppler principle of calculating flow without requiring vessel angle. The vessel area in the *en face* (xy) transverse plane is inversely proportional to $\cos(\phi)$, while the z-projection of the velocity is proportional to $\cos(\phi)$. Therefore, absolute flow can be measured by integrating the axial Doppler velocity over the vessel area. The figure shows an example of a venule showing the z projection of velocity over the vessel cross-section (upsampled to reduce pixellation). (B) *En face* DOCT image showing axial projection of velocity as a function of transverse position. (C) Zoomed DOCT images of boxed region at a 25 μm depth. (D, E) Validation of DOCT absolute CBF using simultaneous hydrogen clearance in a rat thinned skull preparation. (D) OCT angiogram showing the outline of the hydrogen clearance electrode and field of view for absolute flow measurements as a box, where the dural and superficial cortical vessels are colored orange and the deeper cortical regions are colored green. (E) Plot of DOCT absolute flow and hydrogen clearance flow in $n=12$ rats ($p < 0.001$).

4.3 DLS-OCT Imaging of CBF and Cellular Viability

We developed an integrated dynamic light scattering and OCT technique for high-resolution 3D imaging of heterogeneous diffusion and flow [117]. DLS analyzes fluctuations in light scattered by particles to measure particle diffusion or flow, while OCT uses coherence gating to collect only light scattered from a small volume for high resolution structural imaging. Therefore, the integration of DLS and OCT enables high resolution 3D imaging of diffusion and flow. We derived a rigorous theory for the field autocorrelation function of the complex-valued OCT signal, where static and moving particles are mixed within the OCT resolution volume and the moving particles can exhibit either diffusive or translational motion. Based on this theory, we developed a fitting algorithm to estimate dynamic parameters including the axial and transverse velocities and the diffusion coefficient at every voxel of OCT. We validated DLS-OCT measurements of diffusion and flow through numerical simulations and phantom experiments (**Figure 28 (A)**). This method could image both the axial and transverse velocities of CBF to obtain three-dimensional maps of the diffusion coefficient quantifying non-translational motions.

In order to validate this method, we performed DLS-OCT imaging of the rodent cerebral cortex, to measure 3D maps of the flow velocity and diffusion coefficient (**Figure 28 (B)**) [118]. In the diffusion map, we observed high diffusion spots, whose locations correspond to neuronal cell bodies and whose diffusion coefficient agreed with values from *in vitro* intracellular organelles motion reported in the literature (**Figure 28 (C)**). This technology enables label-free and *in vivo* imaging of the diffusion-like motion of intracellular organelles (so called intracellular motility; IM). We performed preliminary studies to demonstrate this method to monitor CBF and IM during a brief ischemic stroke, where we observed an induced persistent reduction in IM, despite the recovery of CBF after stroke. As the preliminary data suggests, DLS-OCT provides a unique means to simultaneously monitor CBF and individual cell viability *in vivo*.

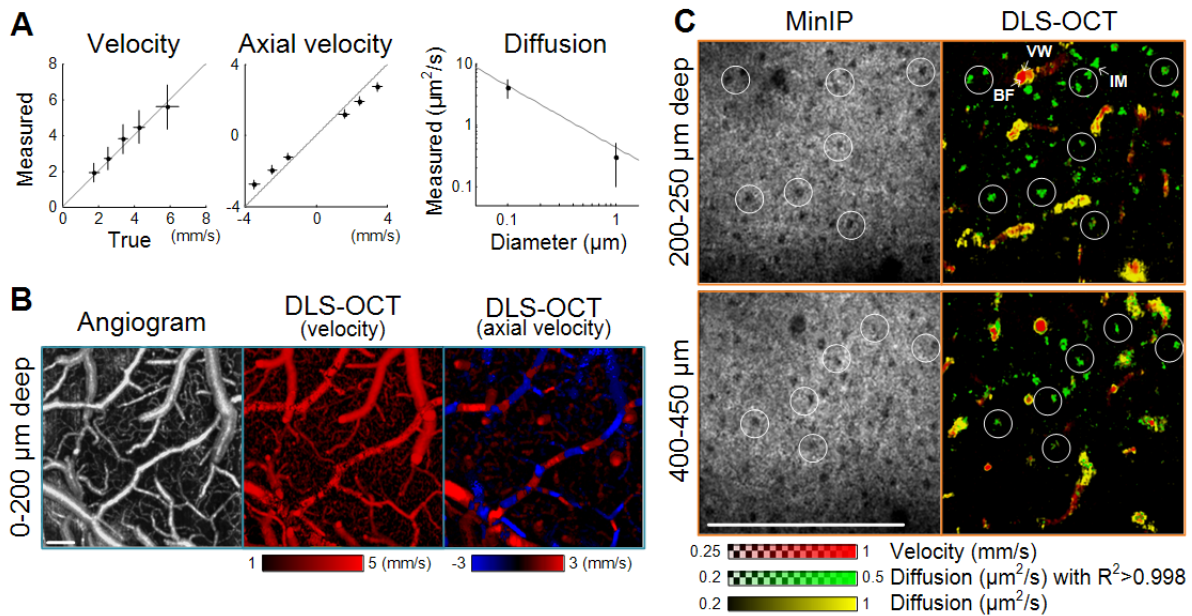


Figure 28. Quantitative imaging of cerebral blood flow velocity and intracellular motility using dynamic light scattering - optical coherence tomography (DLS-OCT). (a) Phantom validation of DLS-OCT measurements of flow velocities (left and center) and diffusion coefficient (right). The gray line

in the right panel shows the Einstein–Stokes equation. Data are presented in mean \pm s.d. (b) DLS-OCT imaging of the cerebral cortex. An OCT angiogram and DLS-OCT maps (absolute velocity and axial velocity) are presented as *en face* images using a maximum projection over a 200 μ m depth. A negative velocity (blue) in the axial velocity map means that blood flows toward the cortical surface. The scale bar is 200 μ m. (c) DLS-OCT imaging of neuronal intracellular motility. The velocity and diffusion images (red and yellow) are superimposed with the map of diffusion with high coefficient of determination R^2 (green). White circles are collocated to show the spatial correlation between the positions of neuronal cell bodies (dark spots in minimum intensity projection, MinIP) and neuronal intracellular motility (green spots). Not all cell bodies are marked. BF, blood flow; IM, intracellular motility; and VW, vessel wall. Scale bar: 200 μ m.

4.2 OCT Imaging of Capillary RBC Flow Properties

OCT has enabled quantification of blood flow in arteries and veins [133], and visualization of microvasculature [11]. However, in order to quantify blood flow in the microvasculature, it is important to note that capillaries have different flow characteristics than arteries and veins. RBCs flow one-by-one in capillaries, sometimes with large separations, and the hematocrit or linear RBC density varies significantly across segments in capillary networks [124]. Doppler OCT has been widely used to quantify blood flow speed in arteries and veins [133, 134], but its application in capillaries is challenging owing to the discrete nature of capillary RBC flow and the fact that many capillaries lie nearly along the transverse direction. Several decorrelation based methods have been proposed to image the speed or flow even in the transverse direction [119, 135-138], but those approaches only have been validated in large vessels or glass capillaries whose diameters are larger than 100 μ m [136, 138-140]. Cerebral capillaries are \sim 8 μ m in diameter, such that RBCs only can pass one-by-one. A second issue in quantifying capillary flow properties is the varying hematocrit. While arteries and veins have a relatively constant hematocrit equal to the systemically measured hematocrit, the hematocrit or RBC linear density is known to vary significantly across segments in capillary networks [119, 124]. Many of the Doppler and decorrelation based methods validated their measurements of the RBC speed using blood samples with a constant hematocrit, but the signal decorrelation rate is generally hematocrit dependent.

Techniques which involve identification of individual RBC passage will be relatively free from the above challenges of the discrete RBC flow speed and varying hematocrit, and are able to quantify the RBC flux [RBC/s]. Two-photon microscopy line scanning methods [124] and fluorescence video microscopy methods [141] identify individual RBC passage, but they monitor only one or a few capillaries at a time. We developed and investigated a new OCT technique that is based on identification of individual RBC passage, but enables simultaneous measurements over many capillaries [119]. According to the Mie scattering theory which suggests that 1 μ m wavelength light scattering is sensitive to scatterers of 0.1 μ m to 10 μ m in size, high backscattering (i.e., large OCT signals) will result from RBCs as well as cellular constituents and membranes. We validated the hypothesis that the OCT signal at a given voxel is sensitive to the transit of a single RBC through the voxel (**Figure 29 (A)**). This finding enabled us to measure the RBC speed, flux, and density over a large number of capillaries in a relatively short period of time. The OCT method was compared with the traditional stripe imaging based technique (**Figure 29 (B)**). This new OCT method provides a means to monitor microvascular flow dynamics over many capillaries located at different depths at the same time (**Figure 29 (C)**).

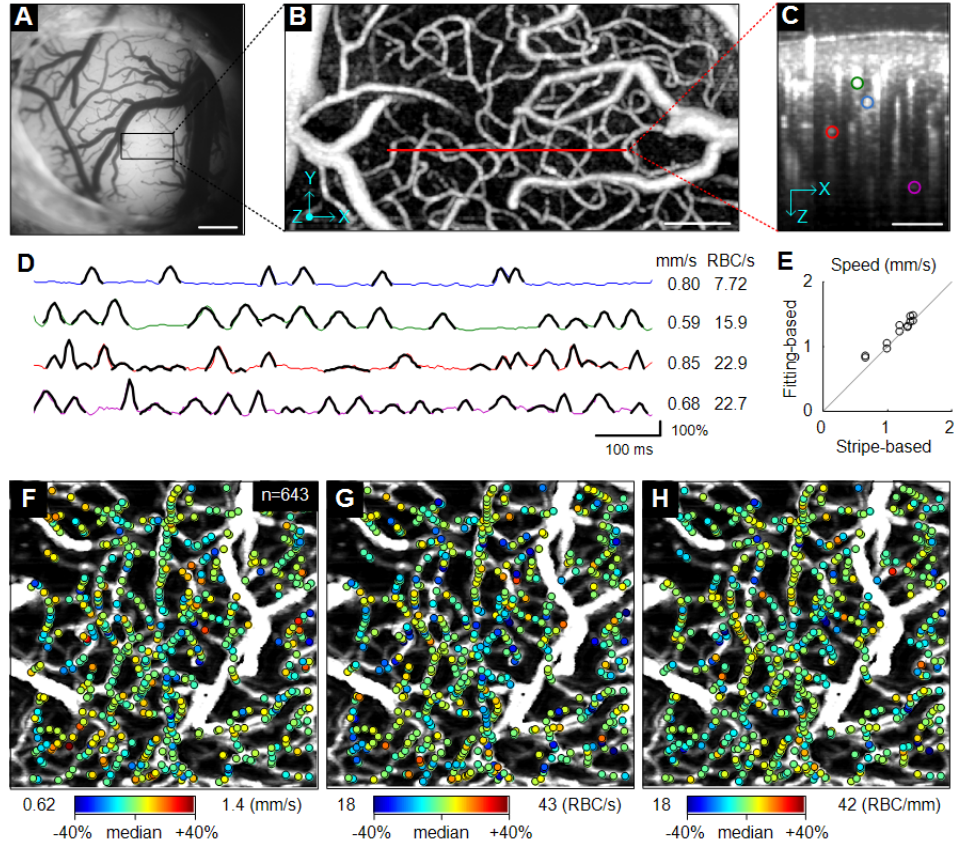


Figure 29. Multiple-capillary measurement of RBC speed, flux, and density with OCT. (A) CCD image of the cortical surface through the cranial window. Scale bar: 500 μm . (B) The *en face* maximum intensity projection (MIP) of the 3D OCT angiogram over a 0–400 μm depth. Ten volumes were averaged. The red line indicates the scan line for cross-sectional dynamic OCT imaging. Scale bar: 100 μm . (C) The cross-section of the 3D angiogram. Data are presented over four selected capillaries (color circles). Scale bar = 100 μm . (D) RBC passage captured in OCT intensity time courses. The lines present the time courses of relative intensity changes at the four capillaries, with colors matching to those in panel C. The peaks were localized over a few neighboring voxels. Gaussian fits obtained by our algorithm were overlaid (black pieces). Fitting-based estimations of the RBC speed (mm/s) and flux (RBC/s) are presented on the right side. (E) Comparison between the fitting- and stripe-based measurements of the RBC speed. (F–H) Estimated RBC speed, flux, and density are presented as color spots on the MIP angiogram. We performed the above analysis of the OCT intensity time courses for each cross-sectional plane in the volume of interest. Data are presented with relatively comparable ranges (median \pm 40%) for all flow properties.

4.5 Rapid Volumetric Imaging of Capillary Network Flux

Interest in blood flow regulation in the brain has been evolving towards understanding the role of the spatio-temporal dynamics of capillary networks. In contrast to arterioles, capillaries have been reported to exhibit highly heterogeneous responses to neural activation, capillary by capillary [142, 143], and nearly stochastic distributions during baseline [141], potentially masking neural activity-induced responses within single capillaries [124]. Thus, in order to characterize capillary network flow responses to brain activation with sufficiently high statistical power, it is necessary to measure blood flow properties over hundreds of capillaries at the same time and with high temporal resolution of ~ 1 second during functional activation. Although the technique described in the previous section is faster than two-photon microscopy, it still requires

hundreds of seconds to obtain a map over a capillary network consisting of hundreds of capillaries.

We have obtained preliminary results using a novel method to quantify capillary RBC flux with higher temporal resolution using rapid volumetric imaging data, where only two scans are repeated for each plane. To achieve this, we utilize a statistical intensity variation (SIV) metric quantifying the normalized OCT intensity difference between the two consecutive scans. If there are no RBCs flowing, the signal difference is zero. Also, if there is no RBC present during the two consecutive scans, the signal difference is zero. As the flux of RBCs increases, the probability of an RBC being present for one scan, but not the other scan increases and the signal difference increases on average as the flux increases. As described in reference [144] and show in **Figure 30 (A, B)**, we have shown that the mean SIV is proportional to the RBC flux through both simulations and measurements. From rapidly scanned volume data, we used Hessian matrix analysis to vectorize a segment path of each capillary and estimate its flux from the mean of the SIVs gathered along the path. Repeating this process led to a 3D flux map of the capillary network as shown in **Figure 30 (C)**, which required only a 10 second data acquisition. Therefore, by properly splitting the imaging area and merging data, this technology enabled us to trace the RBC flux changes over hundreds of capillaries with a temporal resolution of ~ 1 second during functional activation (**Figure 30 (D)**). This high-throughput monitoring of capillary RBC flux dynamics will enable us to investigate many processes which were not possible to address using previous technologies. We believe that many of these advanced imaging techniques will be translatable to ophthalmology and other clinical applications.

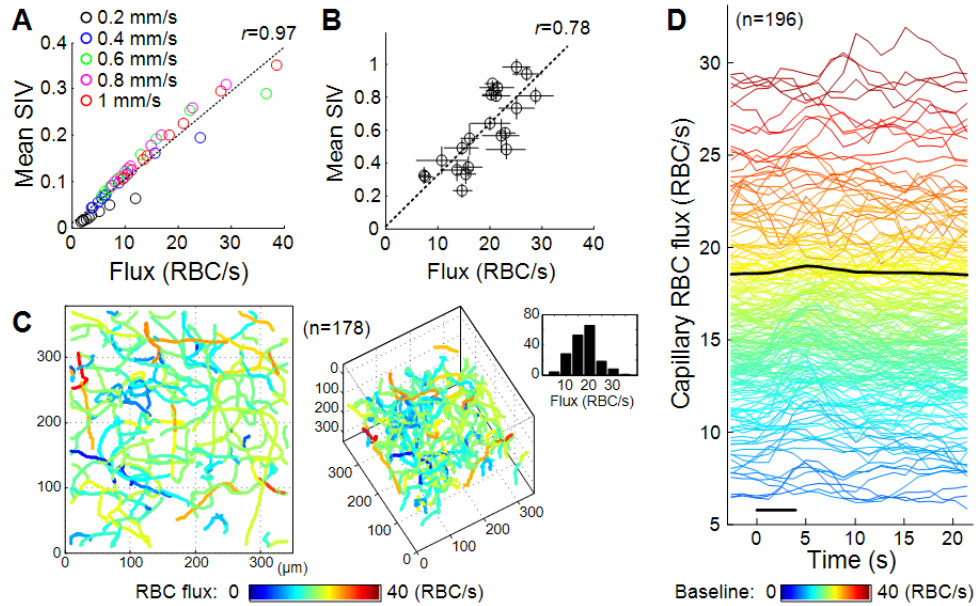


Figure 30. Statistical intensity variation (SIV) analysis for rapid volumetric imaging of capillary network flux. (A) Numerical simulation of the relation between the mean SIV and the RBC flux. We performed numerical simulations to validate the mean SIV as a function of the RBC flux. First, we numerically synthesized OCT time courses embedding RBC passage peaks, for various flow speeds and mean RBC separations. From each time course, we sampled a set of SIV values with the time gap equal to the one that was used in experiments (11 ms). Then, we averaged the set of SIV values into a mean value and compared it to an RBC flux obtained by counting the RBC passage peaks during the time course. The mean SIV was proportional to the RBC flux regardless of various speeds and densities as hypothesized ($r=0.97$). (B) We

also experimentally investigated the relation of SIV to RBC flux. We obtained OCT intensity time courses of capillary centers (4 s in length, $n = 22$) that exhibited individual RBC passage as in the publication [119]. We divided each time course into four 1-s segments; for each segment, we counted the number of peaks for true RBC flux values and obtained the mean of randomly sampled SIVs; and then presented their mean and standard deviation (SD) as a single data point in this figure. We experimentally found that the mean SIV was linearly related with the RBC flux ($r = 0.78$). The slope and intersect will depend on the measurement system and scanning protocol including the time gap (Δt). The slope was slightly larger in the experiment, likely because the experimental data had non-zero fluctuations even when no RBC passes. The empirical relation with our system and $\Delta t = 11$ ms was $(SIV) = 0.012 + 0.032 \times (\text{Flux})$. Since isotropic voxels were used, this relation is in principle independent of the direction of RBC flow or the angle between the capillary axis and the scanning plane. (C) 3D flux map of the capillary network. Using our algorithms to vectorize capillary segment paths and the SIV volume data, the RBC flux of each capillary segment was obtained from the mean SIV averaged along its path. This technique enabled us to measure the RBC flux over hundreds of capillaries, leading to a 3D flux map of the capillary network. The bar graph in the right shows the RBC flux histogram of 178 capillaries. (D) Time courses of RBC flux changes 196 capillaries during functional activation. We performed dynamic SIV imaging over an ROI near the center of functional activation in the somatosensory cortex corresponding to forepaw stimulation. A temporal series of 20 SIV volumes was obtained by averaging over ten runs of stimulation, leading to a temporal series of 20 capillary network flux maps. It was possible to trace how the RBC flux varies with activation over 196 capillaries. A change in the mean flux averaged across capillaries is presented by the thick black curve. The peak change was 2.2% and highly significant ($p < 10^{-8}$). The black bar in the bottom indicates the duration of forepaw stimulation (3 Hz for $T = 0 - 4$ s).

5.0 Endoscopic OCT Technology and Applications

Barrett's esophagus (BE) is a common condition associated with gastroesophageal reflux disease (GERD) in which the normal squamous epithelium of the esophagus is replaced by metaplastic columnar epithelium [145, 146]. In the US, about 5.6% of the population is affected by this disease [147]. Patients with BE have an increased risk of developing esophageal adenocarcinoma [148], which is a lethal disease with less than 20% five-year survival rate [149]. The incidence of esophageal adenocarcinoma (EAC) has increased dramatically over the past decades [150, 151].

For over 15 years we have been working in collaboration with Dr. Hiroshi Mashimo, MD, PhD, at the VA Boston Healthcare System and Harvard Medical School to develop and apply advanced endoscopic OCT technology to improve the management of BE and related diseases of the gastrointestinal (GI) tract. During the previous grant period we made significant advances towards developing endoscopic OCT as a clinically accepted imaging modality. We performed clinical studies on the natural history of BE disease, as well as identifying markers that can be useful in planning endoscopic interventions or predict treatment outcomes. In another set of studies, we continued advancing the state of the art of the endoscopic OCT technology by developing OCT imaging engines with ultrahigh imaging speeds and OCT imaging catheters with high speed, precision beam scanning. This new generation ultrahigh speed endoscopic OCT technology enables three dimensional, depth resolved visualization mucosal surface patterns and microvasculature, promising to enhance the sensitivity and specificity of OCT for identifying early neoplastic changes as well as assessing treatment response.

5.1 Clinical Studies with Endoscopic OCT

Radiofrequency ablation (RFA) is an emerging endoscopic therapy for treating Barrett's esophagus (BE) [40-44]. Utilizing electrode arrays, RFA catheters deliver radiofrequency energy

to ablate BE with a low risk of complications such as stricture [45, 46]. Recent studies have shown that complete eradication of intestinal metaplasia (CE-IM) was achieved in 93% of patients with dysplasia after two years [152] and in 92% of patients with non-dysplastic BE (NDBE) at 5-year follow-up [153]. However, recurrence of intestinal metaplasia (IM) has been observed in 13% [152] to 26% [154] of patients at 1 year after CE-IM. Repeated RFA treatments are generally required to achieve CE-IM [47-49]. On average, CE-IM was achieved after 3.4 RFA sessions for patients with NDBE [153] and over 3.5 sessions for patients with dysplasia [43, 152]. After RFA treatment, new squamous epithelium generally replaces the BE epithelium. However, residual BE glands can become "buried" by the neosquamous epithelium and are not visible by conventional endoscopy, even using chromogen or narrow band imaging (NBI). Because areas of neosquamous epithelium are not routinely biopsied in clinical practice, these buried glands are likely under-appreciated with the current surveillance protocol [43, 153, 155].

OCT has the capability to visualize subsurface features in the human esophagus with 1-2 mm imaging depth, enabling evaluation of morphology under the squamous epithelium. The development of high speed endoscopic OCT technology [156-159], enables three-dimensional (3D) comprehensive imaging of the epithelium. Because buried glands cannot be detected using standard endoscopic imaging, OCT uniquely enables depth-resolved imaging of a broad area with near-microscopic resolution and is a promising technology for identifying and characterizing buried glands before and after ablative therapies. In addition, depth-resolved imaging can also characterize the thickness of different mucosal layers in the BE region, which may guide treatment dosage and improve efficacy.

During the previous contract period, we performed several clinical studies of RFA using a prototype 3D-OCT imaging system developed by LightLab Imaging (a subsidiary of Saint Jude Medical) combined with custom built imaging probes. The SS-OCT system used a Fourier domain mode-locked laser operating at 60 kHz A-scan sweep rate and 1310 nm wavelength. The system had ~5 μ m axial and ~15 μ m transverse resolution in tissue. The OCT imaging probe had a 2.5 mm outer diameter and was radially scanned at 60 Hz and pulled back at 1 mm/s. 3D-OCT data sets, covering a region of 8 mm (circumference) \times 20 mm (length) \times 2 mm (depth) were acquired in 20 seconds.

In one study, we quantified buried glands using endoscopic 3D-OCT in a cohort of 27 patients undergoing RFA treatment [160]. In a second study, we identified structural markers that predicted RFA treatment response using endoscopic 3D-OCT in a cohort of 33 patients undergoing RFA treatment [50]. Results of these two studies will be summarized in the next two sections.

Characterization of Buried Glands Pre- and Post- Radiofrequency Ablation using 3D-OCT

Figure 31 shows examples of cross-sectional OCT images (**A**, **B**) and corresponding histology (**c**) of the gastroesophageal junction (GEJ). Buried glands (red arrows) were identified with 3D-OCT at the GEJ of a patient during the imaging procedure. Biopsies were performed on landmarks identified during OCT imaging using video endoscopy. The histological micrograph shown in **Figure 31 (C)** confirmed the presence of buried glands with intestinal metaplasia underneath neosquamous epithelium.

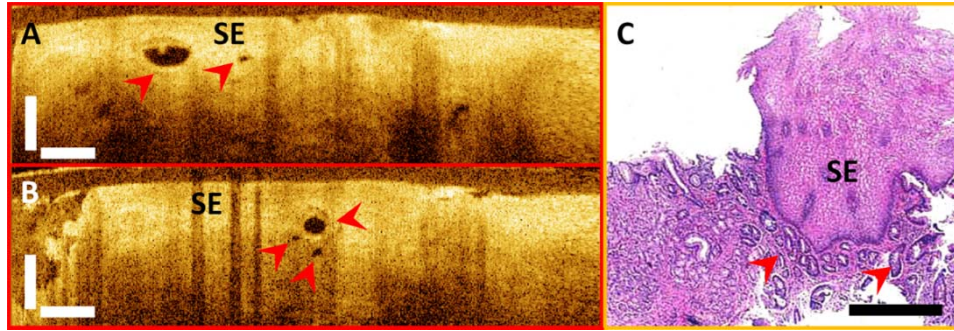


Figure 30. Cross-sectional OCT images and corresponding histology showing buried glands (red arrows) from one patient *in vivo* (a-c). Histological micrograph shown in (c) confirmed the presence of buried glands with intestinal metaplasia. SE, squamous epithelium. Scale bars: 500 μ m.

From the entire patient cohort, buried glands were identified in 72% (13/18) of patients in the pre-CE-IM group and 63% (10/16) of patients in the post-CE-IM group. Overall, 620 and 114 buried glands were marked in 3D-OCT datasets from patients in the pre-CE-IM and post-CE-IM groups, respectively. For comparison, **Figure 32** shows histograms of the gland sizes (**Figure 32 (A)**) and the distance from the squamous-columnar junction (SCJ) (**Figure 32 (B)**). On average, the size of the buried glands was 214 ± 126 μ m in the pre-CE-IM group, and 219 ± 111 μ m in the post-CE-IM group, respectively. Furthermore, the distribution of the buried glands relative to the SCJ was also similar in both groups (**Figure 32 (B)**). 67% (415/620) and 69% (79/114) of the glands were observed within 5 mm from the SCJ in the pre-CE-IM group and post-CE-IM group, respectively. The average distance of these glands from the SCJ was 3.6 ± 2.7 mm in the pre-CE-IM group and 3.8 ± 3.9 mm in the post-CE-IM group and was not statistically significant between the two groups ($p = 0.54$).

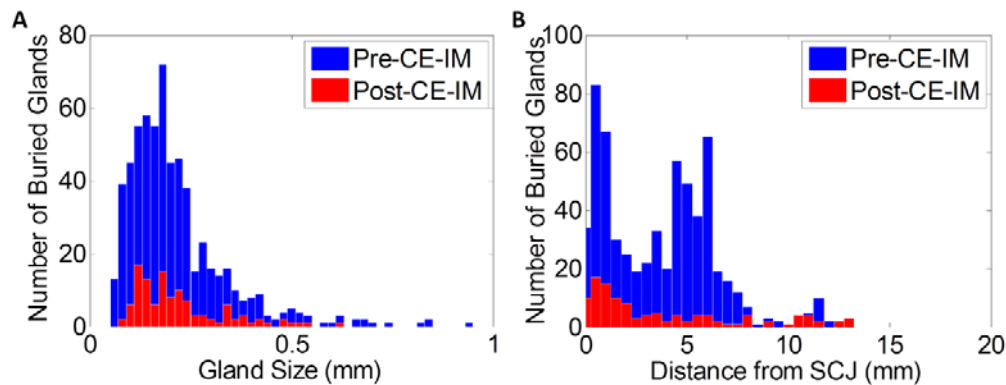


Figure 32. Histograms of (a) the buried gland size and (b) distance from the SCJ in the Pre-CE-IM and Post-CE-IM groups. No significant difference was observed in either the gland size or gland distribution between the two groups.

This study demonstrates that 3D-OCT provides sufficient sensitivity to detect buried glands pre- and post-CE-IM. Interestingly, a very high prevalence of buried glands was observed in both groups, with 72% of patients pre-CE-IM and 63% in the post-CE-IM group. The number of buried glands per patient decreased significantly after CE-IM is achieved ($p = 0.02$). However, the size and distribution of the buried glands relative to the SCJ in patients with short segment BE did not change significantly post-CE-IM.

Endoscopic 3D-OCT Markers of Radiofrequency Ablation Treatment Response

Figure 33 (A) shows an example endoscopic image of the gastroesophageal junction (GEJ) before focal RFA treatment. 3D-OCT imaging was performed at the GEJ over the area of BE (pink colored). **Figure 33 (B)** shows a representative cross-sectional OCT image obtained at the GEJ prior to the RFA treatment, together with histology obtained from the same site (**Figure 33 (C)**). The thickness of the BE epithelium was measured from the OCT image as distance between the BE surface to the top of the lamina propria (LP) / muscularis mucosa (MM) layer.

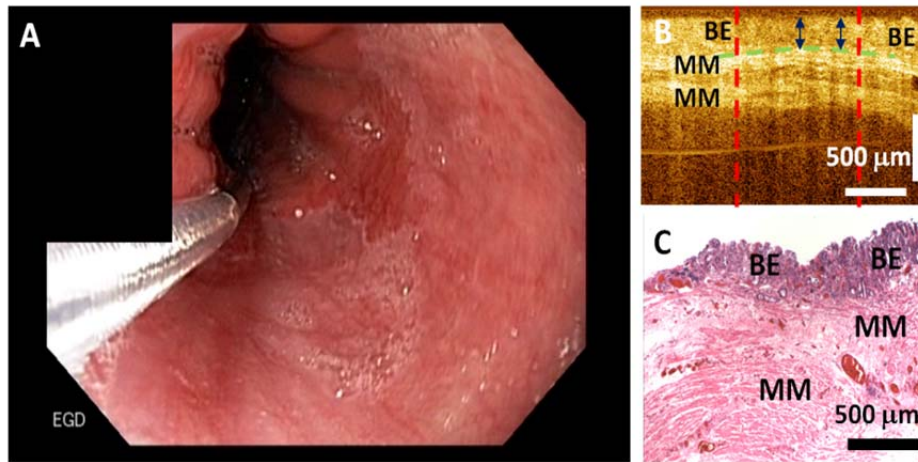


Figure 33. (a) Representative endoscopic image of the GEJ before RFA treatment. (b) Representative cross-sectional endoscopic OCT image and (c) corresponding histology illustrating the BE epithelium thickness measurement.

The BE thickness measured with OCT prior to RFA was found to be a predictor of the RFA treatment response. Both the average and maximum BE thickness prior to RFA were significantly thinner for the CE-IM group compared to the non-CE-IM group (average BE thickness, 257 ± 60 μm versus 403 ± 86 μm , $p < 0.0001$). The scatter plot in **Figure 34 (A)** shows the difference between the average BE thickness for the two groups. **Figure 34 (B)** shows ROC curves using average and maximum BE thickness to predict RFA treatment response. The area-under-the-curve (AUC) was 0.942 ($p < 0.001$) and 0.934 ($p < 0.001$) using the average and maximum BE thickness, respectively. An average BE thickness of 333 μm was determined from the ROC curve to achieve the best prediction accuracy. Using this decision threshold, a sensitivity of 92.3% (12/13), specificity of 85% (17/20), PPV of 80%, NPV of 94.4% and an accuracy of 87.9% (29/33) was obtained for predicting treatment response evaluated by the presence or absence of endoscopically visible residual BE at follow-up visit using the average BE thickness measured with OCT prior to the RFA treatment. The BE thickness measured with OCT was not correlated with the length of the BE ($p = 0.88$) or the number of prior RFA treatments ($p = 0.24$).

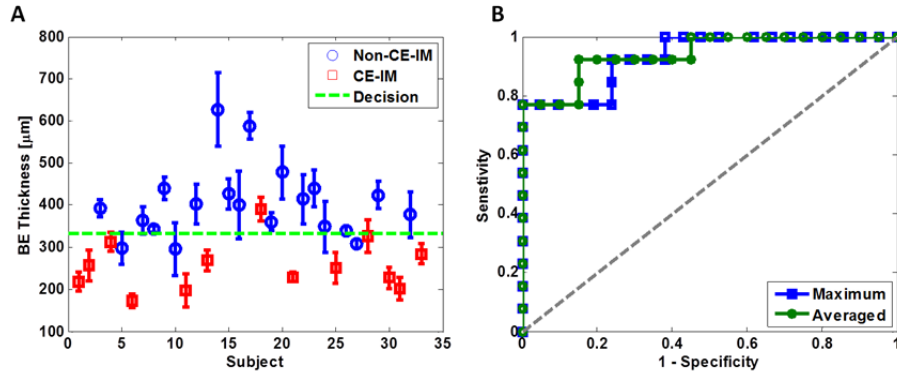


Figure 34. (A) Scatter plot of the average BE epithelium thickness measured by OCT. Blue circles: Non-CE-IM group; Red crosses: CE-IM group; Green dotted line: discrimination threshold at 333 μm as determined from the average BE thickness ROC curve in (B). (B) ROC curves of treatment response prediction using average (green) and maximum (blue) BE thickness. The area-under-the-curve (AUC) values were 0.942 ($p < 0.001$) and 0.934 ($p < 0.001$) using the average and maximum BE thickness, respectively.

In summary, these studies show that endoscopic 3D-OCT can identify structural markers, such as BE thickness and residual glandular structure which are predictors of RFA treatment response at follow up. 3D-OCT may provide information which will enable real-time treatment decisions, improving the efficacy of RFA treatment and reducing the number of required treatments in the future.

5.2 Endoscopic OCT Technology Development

Ultrahigh Speed Endoscopic Swept Source OCT System

Our ongoing collaboration with Praevium Research and Thorlabs Inc. in VCSEL light source development has enabled us to design and develop ultrahigh speed endoscopic swept source OCT (SS-OCT) technology that is 10-20 times faster than commercially available endoscopic OCT technology. We have translated this ultrahigh speed technology to the endoscopy clinic, working in collaboration with Dr. Hiroshi Mashimo, M.D., Ph.D. at the Boston Veterans Affairs Healthcare System and Harvard Medical School. Ongoing clinical studies are investigating the diagnostic potential of this advanced endoscopic OCT technology.

The ultrahigh speed endoscopic SS-OCT system operates at 1300 nm using a MEMS VCSEL light source. The system schematic is shown in **Figure 35**. The laser sweep is triggered by a function generator at a frequency of 300 kHz. Both forward and backward sweeps are used for imaging, resulting in an effective A-scan rate of 600 kHz. The system uses a dual circulator interferometer design to maximize detection efficiency. A/D sampling is performed using optical clocking from a Mach-Zehnder interferometer to sample the OCT fringe data linear in wavenumber, greatly simplifying processing and reducing data volume. Acquisition was performed using a high speed A/D card (AlazarTech) and custom C++ software. Axial resolution was 11 μm in air and 8 μm in tissue, with an imaging range of 3.3 mm in air. The ultrahigh imaging speeds achieved by this technology enable both 3D volumetric OCT as well as OCT angiography.

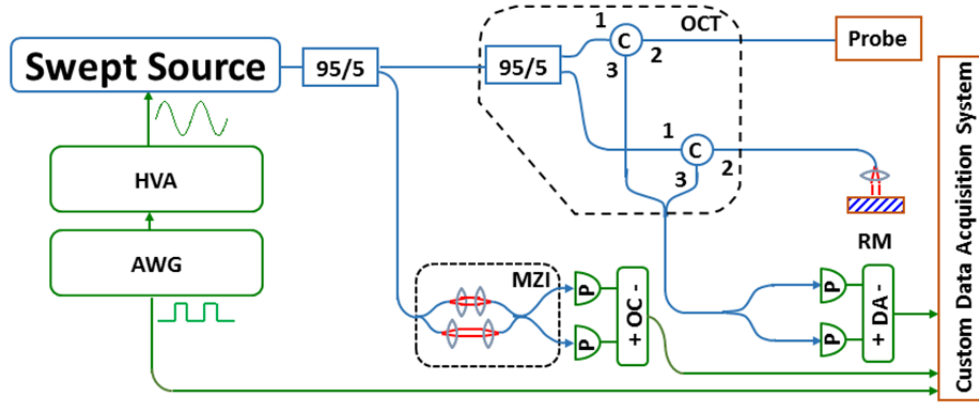


Figure 35. Layout of ultrahigh speed VCSEL swept source OCT system for endoscopic applications. C: circulator. HVA: high voltage amplifier. AWG: arbitrary waveform generator. MZI: Mach-Zehnder interferometer. P: photodetector. OC: optical clock. DA: differential amplifier. RM: reference mirror.

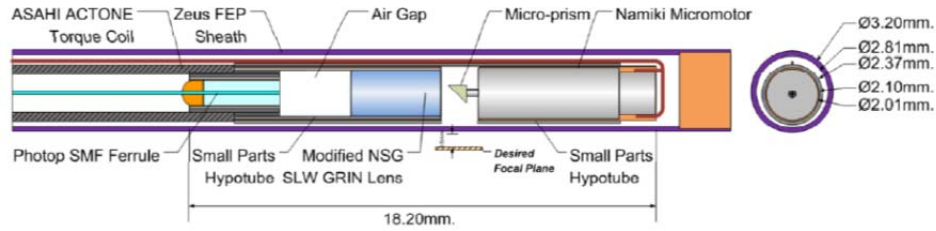


Figure 36. Schematic of micromotor imaging probe. The distal micromotor provides high speed and more stable beam scanning than previous proximally actuated torque cable designs. The probe is small enough to pass through the 3.7 mm accessory port of a standard endoscope.

Micromotor Endoscopic Imaging Probes

To fully utilize ultrahigh speed imaging, we have concurrently developed imaging probe devices capable of high speed beam scanning. Using a micromotor as an optical beam scanner it is possible to develop an imaging probe that is only 3.3 mm outer diameter and less than 20 mm rigid length (**Figure 36**). The small probe size is important because it can be inserted into the 3.7 mm accessory channel of an endoscope and used as an adjunct to standard endoscopy. The micromotor scans in the rotary direction, and the probe is pulled back at the proximal end with a motorized stage at a calibrated speed to generate a 3D OCT volume. High speed distal scanning avoids the need for proximal torque cable rotation, which is a major source of non-uniform rotational distortion in previous OCT imaging probes. This technology was validated in an *in vivo* rabbit imaging study [6]. The imaging speed was 1 MHz A-scan rate and 400 frames per second. The focused transverse spot size of the probe output beam was 8 μm (FWHM). Volumetric images were acquired in the rabbit esophagus and rectum, as well as *ex vivo* human colon tissue. This study demonstrated that ultrahigh speed OCT and high speed scanning probe technology could acquire image volumes over large fields at microscopic resolution.

The instrument was then engineered for use in the endoscopy suite [161]. 3D-OCT imaging was performed in patients with a cross section of pathologies undergoing upper and lower endoscopy. The use of distally actuated imaging micromotor catheters enabled improved access, such as volumetric imaging in the small intestine and the assessment of hiatal hernia using retroflex imaging. The high rotational scanning stability of the micromotor enabled 3D volumetric imaging with micron scale volumetric accuracy for both *en face* OCT and cross-

sectional imaging, as well as OCT angiography (OCTA) for 3D visualization of subsurface microvasculature.

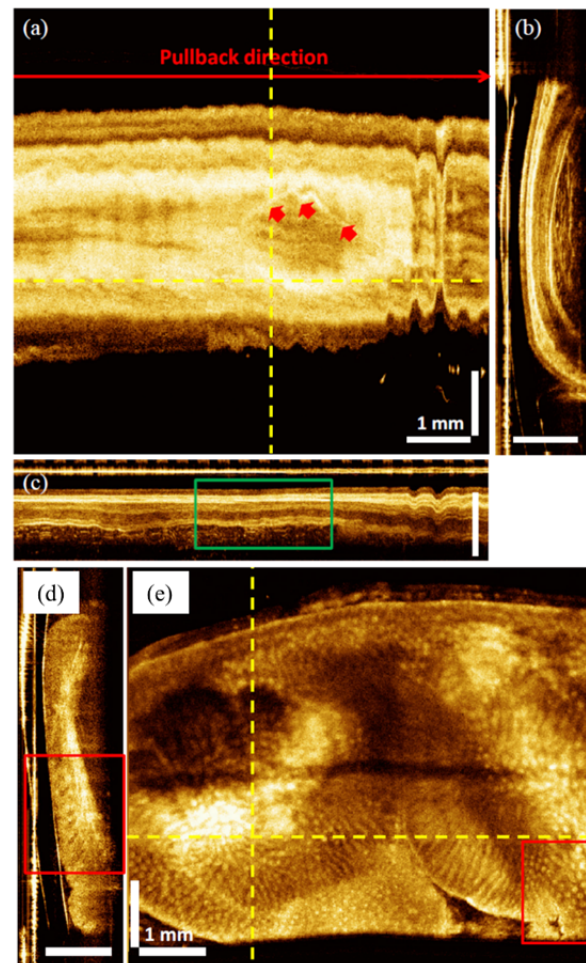


Figure 37. (A, B, C) Volumetric image set of rabbit esophagus showing *en face*, cross-sectional and longitudinal planes respectively. The layered architecture of the esophageal wall is clearly resolved. (D, E) Volumetric image of *ex vivo* human colon showing cross-sectional and *en face* planes respectively. Surface architecture of colonic crypts are visible.

5.3 Novel Diagnostics with Endoscopic OCT

Progression to esophageal adenocarcinoma (EAC) is characterized by a series of cytological and tissue architectural changes that occur in the squamous epithelium (SE). Following repeated acid exposure due to gastroesophageal reflux disease (GERD), SE is initially replaced by columnar lined esophagus, a condition known as Barrett’s esophagus (BE). BE in turn progress to low grade (LGD) and later to high grade dysplasia (HGD), and eventually becomes EAC [39]. Dysplasia of any grade increases cancer risk by an order of magnitude [162], and HGD is associated with a 10–60% risk of developing adenocarcinoma within 3-5 years [163-165]. Although EAC is highly lethal once the cancer arises, prognosis is very favorable if it can be detected and treated at a dysplastic state. Treatment methods for BE with HGD, such as radiofrequency ablation (RFA) have been shown to have high success rates. Therefore, detection of dysplasia is of paramount importance in reducing progression to EAC.

Over the past decade several studies have assessed the utility of OCT to identify dysplasia [166, 167]. However limitations in imaging speed made it difficult to acquire high density volumetric data sets which are required in order to generate *en face* OCT images. Furthermore, previous OCT imaging probes employed proximal scanning that necessitated the rotation of a long (~2 m) torque cable. This caused non-uniform rotational distortion (NURD) from friction between the torque coil and probe sheath, distorting *en face* image features [168]. Therefore, to date, diagnostic criteria used in clinical OCT studies have been based on cross-sectional image features [166, 167]. However, these studies have shown a limited diagnostic accuracy and moderate interobserver agreement. The results of previous endoscopic OCT studies suggest that cross-sectional OCT alone might not be sufficiently accurate for detection of dysplasia.

We have recently designed an ultrahigh speed endoscopic swept source OCT system and beginning in 2013 deployed it to the endoscopy clinic at the Boston VA Healthcare System and Harvard Medical School to perform clinical endoscopic studies. This advanced technology enables new imaging techniques which promise to improve the diagnostic potential of endoscopic OCT. We have demonstrated that the high speed imaging and precise beam scanning allows depth resolve *en face* OCT and visualization of mucosal surface patterns, which may be more sensitive markers of dysplasia than cross-sectional image features. In addition, we have also performed the first demonstration of endoscopic OCT angiography (OCTA), enabling three dimensional visualization of the microvasculature without the need of exogenous contrast agents. This result was featured on cover of *Gastroenterology*, 147, 6, December 2014, Tsai, et al. This result is significant not only because it represents a highly challenging technical accomplishment, but also because the combination of microvascular features with structural features promises to improve the sensitivity and specificity for detecting early neoplastic changes. The next sections will summarize the clinical results we have obtained with advanced endoscopic OCT.

En Face OCT and Pit Patterns

Conventional endoscopy produces views that visualize surface morphology. Therefore, a number of imaging techniques have been developed to not only characterize features observed on the endoscopic views and correlate them with pathology, but also to improve the contrast and visibility of the surface structures. Imaging techniques such as magnifying endoscopy, chromoendoscopy, narrowband imaging (NBI) and confocal laser endomicroscopy (CLE) have been extensively studied to enhance the visualization of the surface patterns and improve the diagnostic yield of endoscopy. However, these techniques suffer from limitations including low diagnostic accuracy, high interobserver variation, limited coverage, extended procedural time and the need for exogenous contrast agents; which so far hindered their clinical acceptance.

Using ultrahigh speed endoscopic swept source OCT technology, we have imaged more than 40 patients to date. Continuing enrollment is ongoing. The ultrahigh speed endoscopic OCT system, combined with high speed and precision distal scanning probes enabled depth resolved visualization of mucosal surface patterns with high resolution and contrast. **Figure 38** shows representative *en face* OCT images from a variety of normal mucosal surface patterns pertinent to both the upper and lower GI tracts, as well as an example of non-dysplastic Barrett's esophagus (NDBE). **Figure 38 (A)** shows the colonic folds and regular circular pit pattern associated with normal colon. **Figure 38 (B)** shows normal squamous epithelium (SE) which shows homogeneous tissue structure as expected. **Figure 38 (C)** is from an

area with NDBE and shows regularly organized BE pit patterns. **Figure 38 (D)** shows regular gastric pit patterns associated with normal stomach.

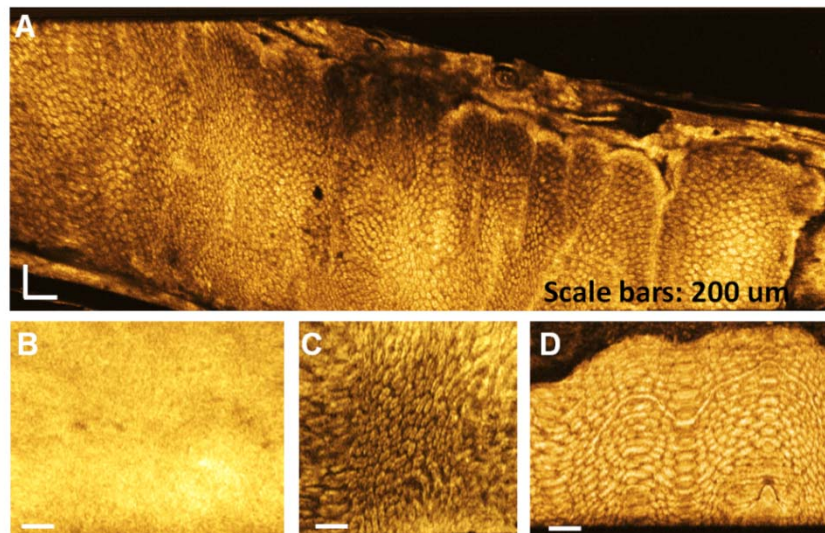


Figure 38. Representative *en face* OCT images of images of normal GI tissues and non-dysplastic Barrett's Esophagus (NDBE). (A) Colonic mucosa. (B) Esophageal mucosa. (C) Barrett's mucosa. (D) Gastric mucosa.

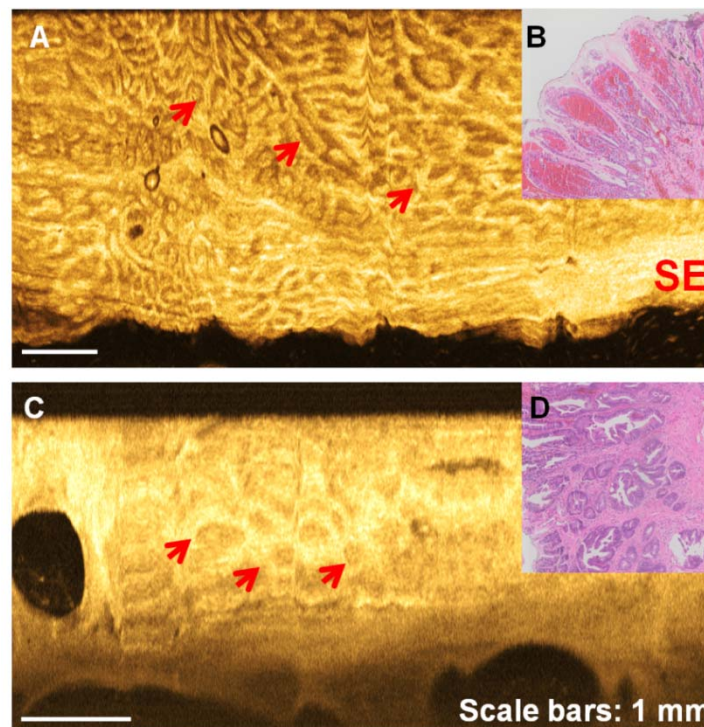


Figure 39. Representative *en face* OCT images of pathologies in the upper GI tract. (A) Low grade dysplasia (LGD). (B) Esophageal adenocarcinoma (EAC), grade T1. (B, D) Corresponding histology from (A) and (C), respectively. Arrows point to irregular pit pattern architecture.

Figure 39 shows representative *en face* OCT images of upper GI pathologies and corresponding histology. **Figure 39 (A)** is from a region with low grade dysplasia (LGD), while

Figure 39 (C) shows intramucosal adenocarcinoma (IMC). Compared with regularly shaped and distributed pit patterns of NDBE, LGD and IMC exhibit irregularity and distortion on the pit patterns. The appearance of the mucosal surface patterns resembles to “ridge/villous” and “irregular/distorted” patterns observed in the endoscopy imaging literature, which are associated with the presence of malignancy [169].

As demonstrated in **Figures 40** and **41**, the ultrahigh speed endoscopic OCT system is capable of visualizing mucosal surface pattern with high contrast and resolution. *En face* OCT images show marked differences between non-dysplastic and dysplastic BE tissue. We are currently continuing patient recruitment as well as analyzing the OCT images to establish a comprehensive diagnostic criteria and performing a sensitivity/specificity test to validate the utility of *en face* OCT in detecting early malignancy in the GI tract.

Endoscopic OCTA and Microvasculature

An important diagnostic criteria used in CLE and NBI for identification of malignancy is the regularity and distribution of tissue vasculature. However, conventional structural OCT imaging does not have vascular contrast. Only larger vessels can be visualized as hyposcattering structures as they cast shadows to the underlying tissues. To overcome this limitation, a set of phase and intensity-sensitive signal processing techniques have been developed that can produce vascular contrast from OCT images. These techniques have been broadly named as Doppler OCT [104, 128] and OCTA [11, 76, 170]. Although OCTA has been demonstrated for visualizing larger vasculature in an animal model [158], speed, resolution and stability of previous systems have not been sufficient for endoscopic clinical applications. Consequently, angiography imaging studies in human subjects have been limited to single cross-sectional 2D frames [171], making assessment of GI pathologies challenging.

The ultrahigh speed imaging and stable beam scanning achieved by ultrahigh speed endoscopic OCT technology makes endoscopic OCTA feasible. We have recently demonstrated endoscopic OCTA from both upper and lower GI tracts of patients undergoing surveillance endoscopy and colonoscopy [2]. **Figure 40** shows example *en face* OCT and OCTA images from normal esophagus and recto-anal junction. The structural *en face* OCT images in **Figures 40 (A, B, E)** show details of tissue architecture and mucosal morphology, however, vascular information is limited to large vessels. The corresponding OCTA images shown in **Figures 40 (C, D, F)**, on the other hand, visualize microvasculature with high resolution and contrast. OCTA is advantageous over CLE since it does not require intravenous injection of exogenous contrast agents (such as fluorescein). Furthermore, it also allows depth resolved visualization of microvasculature over a large field of view (16 mm x 10 mm), which is not attainable by CLE and NBI. Therefore, endoscopic OCTA promises to be a valuable adjunct to OCT structural imaging.

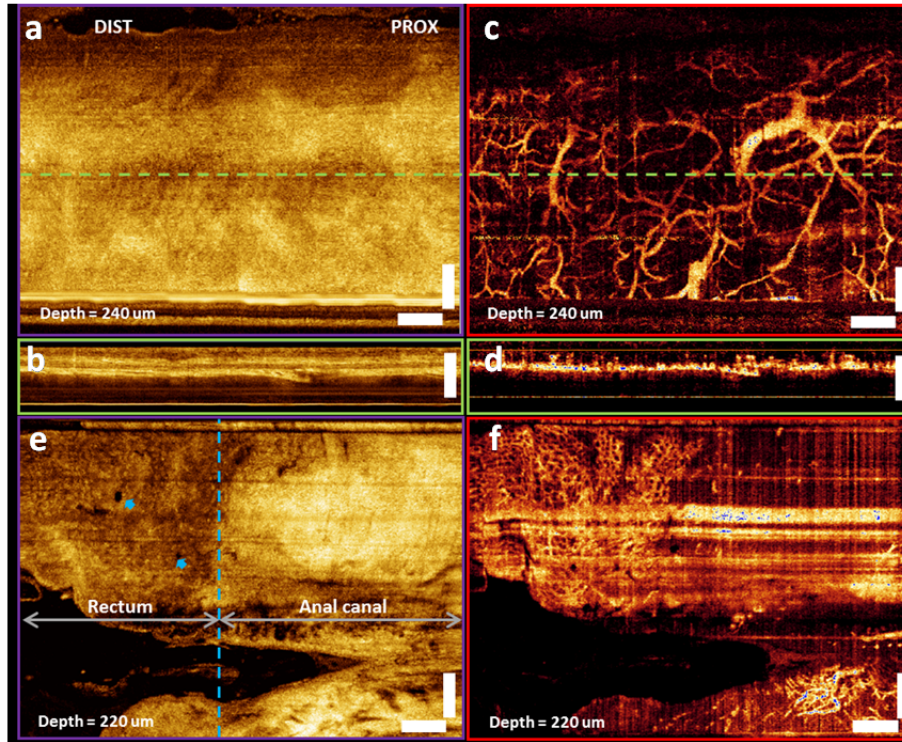


Figure 40. Endoscopic optical coherence tomography (OCT) and angiography (OCTA) of normal esophagus (A–D) and recto-anal junction (E, F). (A) *En face* OCT image at 240 μm depth (lamina propria [LP] layer). (B) Cross-sectional OCT image along the pullback direction. (C) *En face* OCT angiogram in the LP layer. (D) Cross-sectional OCTA along the pullback direction. (E) *En face* OCT image at 220 μm depth (LP layer). (F) OCT angiogram shows the surface vasculature of the crypts in the rectum. Red arrows, anal glands; blue arrows, rectal glands; white bar, 1 mm.

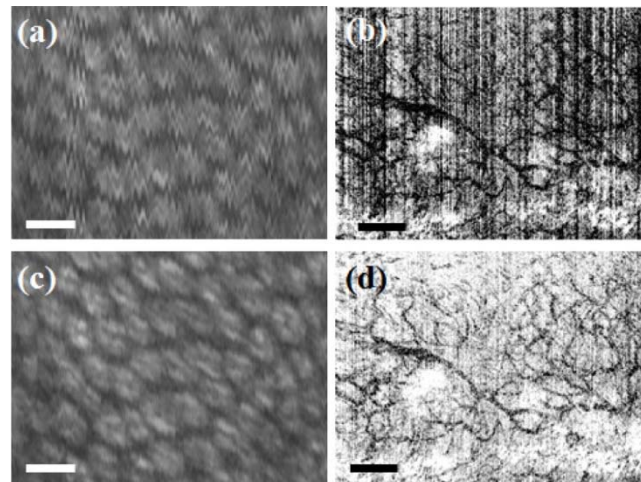


Figure 41. Demonstration of the NURD correction algorithm for *en face* OCT and OCTA images. *En face* OCT images before (A) and after (B) applying the correction algorithm, respectively. OCT angiograms before (C) and after (D) applying the correction algorithm, respectively. All figures are generated by projection over 140 μm of depth, and about 150–500 μm beneath tissue surface. (A) and (C) are taken from the rectum, and (B) and (D) are taken from esophagus of two patients who were undergoing endoscopic surveillance. Scale bars are 200 μm for (A) and (C), and 500 μm for (B) and (D).

Both *en face* OCT and OCTA can have imaging artifacts due to mechanical and patient-related motion. Image processing to generate OCTA involves calculating the correlation between subsequently acquired OCT frames in order to detect motion from blood flow; hence the quality of the OCT angiograms is particularly sensitive to parasitic motion or beam scanning instability. Motion artifacts include cardiac and respiratory motion, as well as non-uniform rotational distortion (NURD) of the imaging catheter. NURD is a major cause of motion artifacts encountered in endoscopic OCT systems [168]. While using a micromotor imaging probe significantly reduces the severity of NURD, residual non-uniformity of the motor rotation on the order of several milli-radians can still cause distortion in the *en face* OCT and OCTA images as shown in **Figure 40 (A, B)**. To address this problem, we have developed a NURD correction algorithm that resamples cross-sectional OCT images based on fiducial markers located on the OCT probe [172]. We have shown that this method achieves a ~15 fold improvement in rotational scanning stability and effectively suppresses artifacts caused by NURD (**Figure 41 (C, D)**).

In summary, the development of advanced ultrahigh speed endoscopic OCT technology based on the VCSEL light source allowed visualization of mucosal surface patterns and the development of endoscopic OCTA with micron-scale resolution and high contrast. Our preliminary studies suggest that these new capabilities are promising for improving the sensitivity and specificity to detect pathology in the GI tract including dysplasia in Barrett's esophagus. The detection of dysplasia in Barrett's esophagus has been an ongoing challenge for the endoscopic imaging community and larger scale prospective studies using integrated structural OCT and OCTA are planned to investigate diagnostic performance.

6.0 Pathology Imaging

Cancer is the second leading cause of death in the United States, responsible for 577,000 deaths in 2012 [173]. Following the detection of malignancy through imaging, routine screening or other methods, the standard of care for many types of cancer, including malignant tumors of the breast [174-176] and thyroid [177, 178], is resection of the tumor and surrounding tissue. Excised tissue is evaluated using conventional histological examination in which the tissue is fixed in formaldehyde, dehydrated, embedded in paraffin, cut into micron thin slices, deparaffinized, rehydrated, stained, dehydrated and finally mounted on a microscope slide for visual inspection. The large number of processing steps require considerable time, usually in excess of one day [179]. The resulting delay between surgery and pathological assessment poses complications when surgical treatment depends on the results of histopathology. For example, in the case of early breast cancer, breast-conserving therapy and radiation is the standard of care because it achieves survival and local recurrence rates equivalent to those of mastectomy while providing superior cosmetic outcomes, reduced morbidity associated with lymphedema, and improved post-operative quality of life [180-184]. However, local recurrence following breast-conserving surgery is strongly correlated with margin status as determined by post-operative histopathology [185, 186]. Owing to the limited sensitivity of gross examination, residual tumor is present near the surgical margin in up to 40% of cases [187, 188]. In the event of a positive margin on histopathology, patients typically require a repeat surgery with associated morbidity and delays in adjuvant therapy. Similarly, in the treatment of papillary thyroid neoplasm, a

finding of vascular or capsular invasion following a lobectomy typically requires a second surgery to perform a total or near-total thyroidectomy [178].

Unfortunately, the long processing times precludes the use of conventional paraffin embedded histopathology for the intraoperative evaluation of excised tissue. An alternative, frozen sections analysis (FSA), replaces dehydration with simple freezing, allowing rapid intraoperative evaluation, but has limited acceptance owing to the processing time per section (~20 min) and low sensitivity and specificity compared to conventional histology [189-191]. Consequently, relatively few surgeons currently use FSA for intraoperative evaluation of breast pathology [192]. These limitations are even more acute in the case of papillary thyroid neoplasms, where sensitivities as low as 17% using FSA have been reported [193] and the use of FSA for papillary thyroid neoplasm is no longer recommended [194]. There is a need for advanced imaging technologies that perform rapid, high resolution imaging of unprocessed tissue samples in the surgical or pathology lab setting.

During the previous reporting period, a major focus of our research was the development of transformative new imaging technologies that could augment or eventually replace the classic histopathology techniques in applications where long processing times interfere with patient treatment. As a result of these efforts, we developed new advanced imaging capabilities based on optical coherence microscopy (OCM) and multiphoton microscopy (MPM) that enable real-time visualization of cellular structure in thick sections of unprocessed human tissue. These techniques replace the lengthy dehydration, embedding, microtoming and staining process with optical sectioning, which enables imaging planes corresponding to thin histological sections without the need to physically cut the tissue. These methods allow rapid evaluation of tissue pathology in a clinical setting (e.g. intrasurgical imaging) while still preserving the tissue to enable subsequent conventional histological processing (e.g. post-operative evaluation).

6.1 Multiphoton Microscopy for Rapid Evaluation of Pathology

Introduction to Multiphoton Microscopy (MPM)

Multiphoton microscopy has had a revolutionary impact on fundamental scientific research and biological imaging in fields ranging from cell biology to neurosciences [195, 196]. MPM can achieve cellular resolution and high contrast axial sectioning in thick tissue specimens by point scanning short pulse near-infrared light across tissue. However, MPM can also provide molecular specific contrast using both extrinsic probes and intrinsic fluorescence, enabling it to visualize many of the same biochemical markers that are the hallmarks of pathology in conventional histological examination. The excellent resolution and molecular contrast available with MPM are particularly well-suited for visualizing subcellular-resolution features, such as nuclear size and shape, and morphological changes in tumor extracellular matrix and stroma, such as reorganization of collagen, which are important hallmarks of neoplasia [197-200].

A major advantage of MPM is the ability to use fluorescent probes that rapidly target specific cellular agents, including DNA, specific proteins and cellular receptors. By carefully choosing contrast agents, MPM images can be generated from unfixed tissue that closely approximate more familiar microscopy techniques, such as the use of DNA-specific dyes and transmission wide-field microscopy in conventional clinical histopathology, but without the lengthy (20+ hour) processing. This concept is demonstrated in **Figure 42**, where an intact, unprocessed human breast tissue specimen has been stained analogously to conventional H&E histology and then optically sectioned using MPM. Consequently, MPM has the potential to enable real-time

evaluation of microscopic pathology in a surgical setting while retaining familiar markers of pathology from conventional histology.

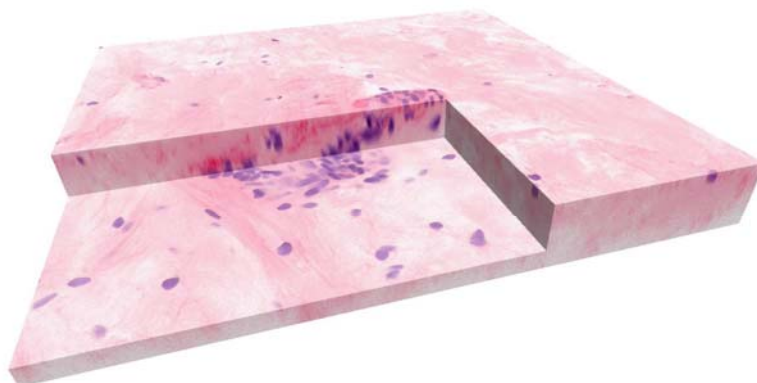


Figure 42. Virtual 3D H&E histopathology performed using multiphoton microscopy (MPM) of freshly excised, unfixed normal human breast tissue showing collagen fibers (red through pink) and cell nuclei (purple).

Preliminary Multiphoton Microscopy Study of Breast Surgical Specimens

Working in collaboration with Dr. James Connolly, M.D. at the Beth Israel Deaconess Medical Center and Harvard Medical School, we investigated the sensitivity of MPM by evaluating freshly excised, human breast lumpectomy specimens for the presence of cancerous tissue on simulated surgical margins. Discarded (not required for patient diagnosis) surgical specimens were rapidly stained with a nuclear contrast agent (acridine orange), mounted against a coverslip, and imaged using two spectral channels, corresponding to two-photon fluorescence (TPF) of acridine orange to visualize nuclei and SHG from collagen to detect stromal organization. In order to facilitate clinical interpretation of nonlinear microscopy images, pseudo-H&E images were created by remapping the TPF and SHG channels to a colormap similar to that of standard H&E histology (**Figure 42**). This use of two channel detection and color mapping generates tissue contrast that is analogous to standard H&E while also displaying images using analogous colors. This method has the powerful advantage that the MPM images more closely match the interpretation paradigm used by pathologists who have extensive training on H&E images.

In order to enable imaging of large (several square centimeters) tissue areas and precise registration with conventional H&E histology, large field of view images were generated by rapidly scanning the microscope stage and specimen. The multiphoton microscope acquires 1024 x 1024 pixel images of a ~500 μm x 500 μm field of view at 20 frames per second. Multiple image frames were mosaicked in post-processing using a combination of unwarping and nonlinear intensity blending algorithms (**Figure 43**). The resulting composite images were then converted to a multilevel tiled pyramid format that allowed for efficient transmission, visualization, zooming, and panning of large, high resolution images (Deep Zoom, Microsoft). This automated image acquisition and processing scheme allowed us to interrogate entire square centimeter areas of breast specimens with nuclear resolution. The image display is similar to “Google Maps” and enables panning a large field of view to rapidly identify regions of interest, then zooming to a high magnification, small field of view (**Figure 44 (A)**). Images at multiple depth levels up to 100 μm below the tissue surface were also obtained to generate images

analogous to serial sections in histology. After nonlinear microscopy imaging, the cassette containing the specimen was placed in 10% neutral buffered formalin prior to processing, paraffin embedding, sectioning, and H&E staining. Corresponding H&E sections were scanned using a digital slide scanner at 20x magnification (Aperio) and converted to the same file format as the MPM images for visualization and reading (**Figure 44 (B)**).

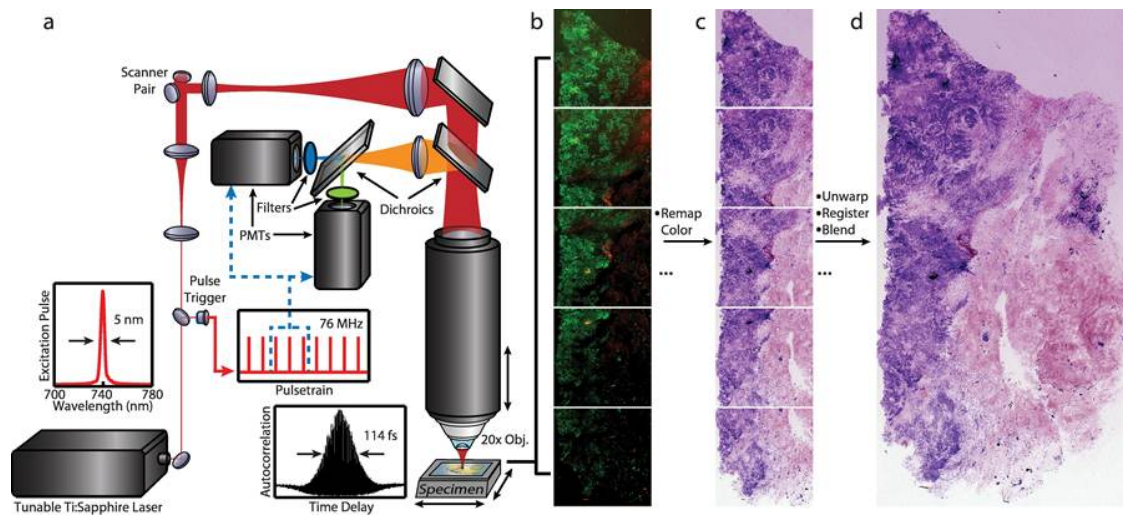


Figure 43. Schematic of multiphoton microscope with extended field of view and color remapping. (A) Dual detection channels are used to collect TPF and SHG signals for nuclear and stromal contrast, respectively. A 1024 x 1024 pixel image can be acquired at a rate of 20 fps. (B) Overlapping fields are automatically acquired and (C) field distortion correction, pseudo-H&E color remapping, and (D) image mosaicking is applied in post-processing.

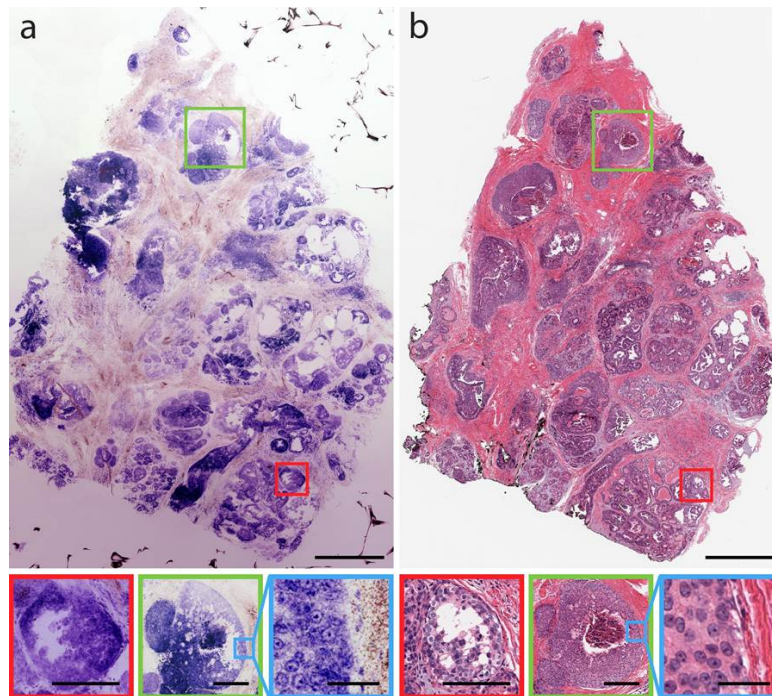


Figure 44. Human breast specimen with ductal carcinoma in situ (DCIS). (A) MPM image and (B) corresponding H&E histology showing different subtypes of DCIS (scale bar: 1 mm). Finger-like projections of abnormal cells invading the duct lumen are indicative of micropapillary DCIS (red box, scale bar: 250 μ m). Holes of cellular debris and comedo plug are indicative of comedo DCIS (green box, scale bar: 250 μ m). Individual cell nuclei at comedo DCIS border exhibit prominent nucleoli consistent with high-grade DCIS (blue box, scale bar: 50 μ m). Field of view: 8.25 mm x 5 mm (660 MPixels).

MPM Data: <http://tinyurl.com/cwyly6s>

H&E Data: <http://tinyurl.com/9teff9a>

We assembled a dataset of 168 specimens from 50 patients imaged with both MPM and conventional H+E histology. The dataset was divided into a 30 specimen training set and 138 reading set that included paired MPM and H&E images. In the preliminary study, each specimen was diagnosed based on the following tissue subclassifications: normal breast tissue, fibroadenoma, fibrocystic changes, biopsy site changes, flat epithelial atypia, lobular carcinoma in situ (LCIS), DCIS, invasive ductal carcinoma (IDC), and invasive lobular carcinoma (ILC). Similar histological subclassifications were then grouped during data analysis to determine the diagnostic accuracy for detecting benign, atypical, and malignant tissues using nonlinear microscopy. Three pathologists read the nonlinear microscopy and H&E images. Each reader was initially trained on paired MPM and H&E data and then asked to read the 138 nonlinear microscopy images while blinded to the results of H&E histology. The three pathologists then read the H&E images one week later to reduce memory confounders. The blinded reading of MPM images achieved an average 95.4% (C.I. 90.3 to 98.0) sensitivity and 93.3% (C.I. 89.3 to 95.9) specificity, respectively, for distinguishing between invasive cancer and DCIS versus benign tissue as compared with the corresponding H&E diagnosis. The negative predictive value was 97.1% and accuracy was 94.1%.

These results demonstrate that MPM can reproduce the diagnostic capability of conventional histopathology without lengthy fixation or processing. These results were published in PNAS, 111, 43, 2014, Tao, et al [3]. The results from this study enabled us to develop a new NIH funded research program (R01 CA178636-02, “Intraoperative real time breast cancer margin assessment with nonlinear microscopy”) and demonstrate the effectiveness of AFOSR funding research in new program development. In this new program, we plan to develop a wide field of view nonlinear microscope designed for the pathology laboratory and working with a team of pathologists, radiologists and surgeons, demonstrate that MPM imaging of breast surgical specimens can be used to guide surgical resection and reduce the rate of second surgeries.

Development of Ultrahigh Speed, Wide Field of View Multiphoton Microscopy for Pathology

In spite of its high sensitivity and specificity, there is an incompatibility between the field of view of MPM, which requires high numerical aperture imaging to generate nonlinear excitation, and the wide field of view, low magnification (1-4 mm) typically employed to evaluate histology. In our pilot study, this was addressed through the mosaicking of hundreds of rapidly imaged 500 μ m x 500 μ m fields to generate a composite image comparable to conventional, low-magnification histopathology. However, in spite of the relatively high imaging speed, this approach alone is insufficient owing to the very large image size and consequently long imaging times required to generate a two photon dataset comparable to a conventional pathology slide.

To address this limitation, we are collaborating with Thorlabs Inc.’s Advanced Imaging Group to develop next-generation multiphoton microscopy optics that will enable wide field of view over areas comparable to conventional low magnification (5-10x) brightfield microscopy but preserving high numerical aperture beam focusing and fluorescence collection. The

technology we are developing will enable rapid (>2 fps) imaging over a 4 mm x 4 mm field of view (16 mm² area) in unsectioned human surgical specimens using a combination of highly optimized laser scanning optics and a novel objective design developed by Thorlabs. With this capability, a pathologist will be able to directly evaluate surgical specimens without the need for mosaicking. Alternatively, by rapid translation of the sample, we estimate that the system will be able to scan and mosaic approximately 1800 mm² per minute, enabling rapid intraoperative imaging of entire surgical specimens.

Development of Gigavoxel Multiphoton Fluorescent Lifetime Imaging Technology

While MPM can be performed with extrinsic contrast agents to label specific cellular or tissue components or even cellular receptors, these agents are typically not approved for *in vivo* applications. For applications such as *in vivo* imaging, where extrinsic contrast is not permissible, the limited intrinsic contrast of tissue may not be sufficient for diagnostic assessment. Fluorescent lifetime imaging microscopy (FLIM) is a complementary imaging modality to MPM that enhances intrinsic fluorescent contrast. FLIM can be performed using MPM for axial sectioning (MPM-FLIM) [201]. In FLIM, single or two photon excitation excites a fluorophore which decays with a characteristic time constant that depends on the specific fluorophore, pH, temperature, local proteins and other characteristics [202-205]. FLIM therefore provides information on the microenvironment of individual cells or entire tissues, which could reflect metabolic changes associated with malignancy [202]. MPM-FLIM has shown promise as a means of detecting pathology in human breast specimens [206] and animal breast cancer models [207] by imaging changes in NADH and FAD lifetimes associated with tumor metabolism as well as changes in stroma.

While high speed imaging and mosaicking of samples is an established technique for wide-area MPM imaging [208], to date MPM-FLIM has been limited to very narrow fields of view because of the extremely slow acquisition rates of existing MPM-FLIM systems which use time correlated single photon counting (TCSPC) [209-211]. It should be noted that FLIM without MPM can be implemented in a wide field geometry significantly faster than TCSPC [212, 213], but does not provide the depth sectioning required for imaging intact tissue specimens and still suffers from relatively low imaging speed compared to MPM. Therefore, although FLIM has shown promise as a means for imaging and detecting cancer pathology, it has not been possible to perform a systematic evaluation of MPM-FLIM in surgical specimens to assess its potential for intrasurgical evaluation.

The limited throughput of TCSPC occurs because it is necessary to illuminate individual pixels at sufficiently low power, such that on average during any given sampling period, only a single photon arrives. With knowledge of the instrument response function, the arrival time of a single photon can be estimated with sub-nanosecond accuracy. However, the need to individually count photons greatly limits throughput [209-211]. To address this limitation, we have developed a fundamentally new approach to MPM-FLIM measurement based on optically clocked, direct temporal sampling of fluorescent emission. In this method (**Figure 44**), adapted from optically clocked, swept source OCT, a fast digitizer is phase-locked to a multiple of the excitation laser repetition rate. Individual laser pulses are imaged onto the sample at normal MPM power levels, generating many thousands of photons per excitation and allowing measurement of the fluorescent decay time at rates that are 3-4 orders of magnitude faster than TCSPC.

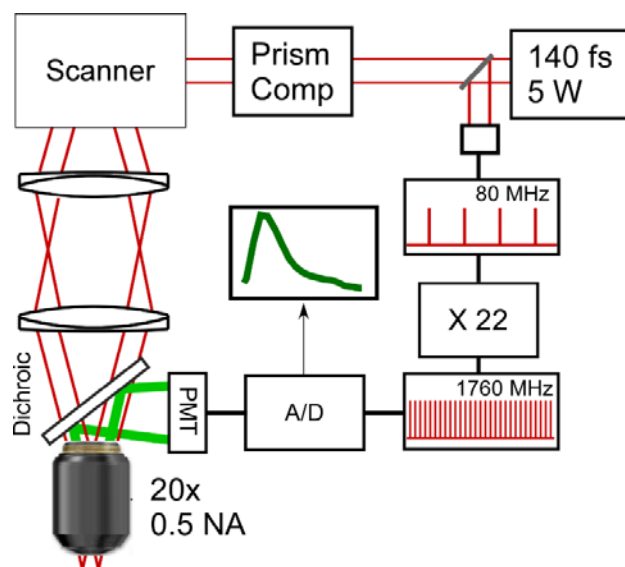


Figure 45. Schematic diagram of the prototype high speed MPM-FLIM technology showing the signal path (upper left path) and the reference clock (lower right clock). A GHz sample rate A/D combines the sample and reference signals to extract time-resolved fluorescence without single-photon counting.

To explore the concept of optically clocked direct temporal sampling, a prototype MPM-FLIM system was developed and used to image freshly excised human breast surgical specimens (**Figure 45**). Images were acquiring with a single spectral channel (375-700 nm) at a rate of 10 megapixels per second over a 1.1 x 0.8 mm field of view **Figure 46 (A)**. An enlarged view (**Figure 46 (B)**) shows a breast ductal structure with a well-resolved supporting basement membrane (yellow/green), columnar secretory cells (turquoise), and metabolically inactive lumen (violet). This preliminary data demonstrates record imaging speeds and strongly suggests that TPM-FLIM imaging of human tissue is feasible at speeds that will enable surveying of centimeter-scale pathology specimens.

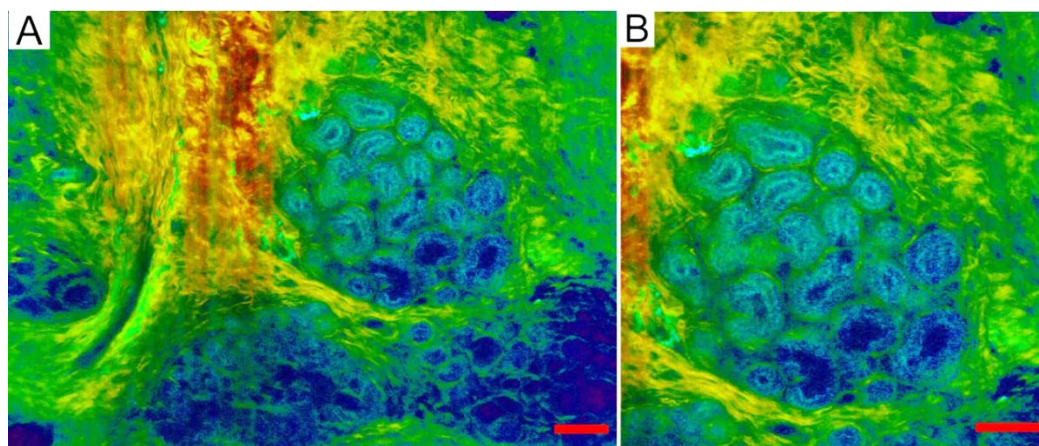


Figure 46. 16 megapixel MPM-FLIM image of freshly excised normal human breast tissue aquired at 10 megapixels/s. (A) 1.1 mm wide field image acquired in 1.6 seconds. (B) Enlarged view of a ductal unit showing individual cells arranged with a well-defined lumen. Scale bars: 100 μ m.

6.2 Development of Next Generation Optical Coherence Microscopy Technology

While techniques based on nonlinear excitation of fluorescence provide molecular contrast and very high resolution, the need for tight temporal and spatial confinement of the excitation beam requires high NA optics and are strongly affected by optical aberration and scattering. This limitation, along with the shorter, more strongly attenuated fluorescence emission wavelength, limit the maximum imaging depth in tissue. Furthermore, although techniques exist for parallel imaging of multiple depths, they are complex and impose further limitations on maximum imaging depth. Consequently, MPM is most effective for imaging *en face* planes which are at shallow depths. In contrast, interferometric techniques can simultaneously image many depths in parallel, operate effectively at a wide range of numerical apertures, and can image at longer wavelengths without the need to detect short (usually visible) wavelength fluorescence. These advantages make interferometric techniques effective for imaging specimens that have three-dimensional structure or specimens for which the region of interest is more than 100-200 μm below the surface.

Optical Coherence Microscopy (OCM)

Optical coherence microscopy (OCM) combines optical coherence with confocal microscopy to enable depth resolved visualization of specimens with cellular resolution [131, 214]. The addition of coherent detection greatly increases imaging depth, while enabling multiple depths to be imaged in parallel, enabling higher imaging rates. In addition, because it uses interferometry, OCM can provide depth-resolved, quantitative phase information from materials or biological specimens, which offers unique advantages over other phase microscopy techniques such as phase contrast and differential interferential interference contrast microscopy [215, 216]. Furthermore, by employing polarization-sensitive detection techniques, OCM can provide depth resolved birefringence information on the samples, including retardation, axis of retardation and degree of polarization non-uniformity.

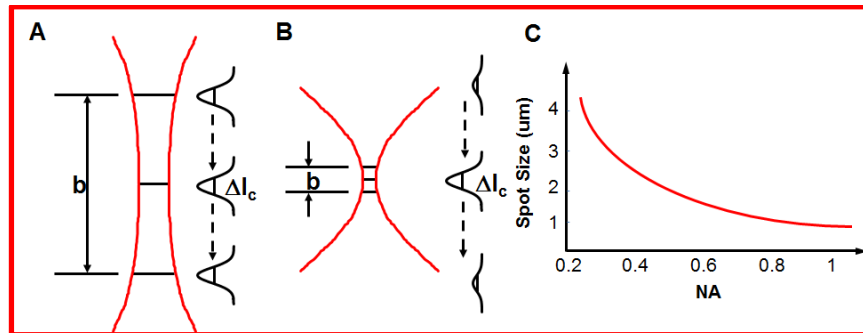


Figure 47. High NA, short confocal parameter (a) and low NA, long confocal parameter (b) imaging regimes. (c) Dependence of the transverse spot size on NA of the objective. l_c : coherence length, b : confocal parameter.

Figure 47 (A, B) shows two general operating regimes for OCM imaging. In the first mode, a relatively low NA objective is employed, which results in a long confocal parameter for the imaging beam, and consequently makes it possible to image over longer depth ranges. However, an increase in confocal parameter comes at a cost of decreased transverse resolution. In microscopic imaging applications where high transverse resolution is desired, high NA objectives must be used. As seen **Figure 47 (B)**, the high NA configuration, while improving the

transverse resolution, reduces the confocal parameter significantly. OCM, however, circumvents this trade-off because the axial resolution is not set by the NA of the objective; but by the coherence length or axial point spread function of the coherent detection. Therefore, the NA in OCM is selected based on the desired spot size. As shown in **Figure 47 (C)**, even a relatively low NA objective gives <3 μm transverse resolution, which is in most cases sufficient for achieving cellular resolution.

Our group first developed and demonstrated OCM in 1994 [131]. We recently demonstrated OCM imaging with a time domain system at a speed of 2 frames per second (fps) over a $400\text{ }\mu\text{m} \times 400\text{ }\mu\text{m}$ FOV [217]. This system was subsequently developed into an integrated 3D-OCT and OCM instrument, enabling multiscale imaging of cancer pathology. Working in collaboration with Dr. James Connolly, M.D. at the pathology department of Beth Israel Deaconess Medical Center (BIDMC) and Harvard Medical School, we performed a series of studies using integrated 3D-OCT and OCM to image normal and pathological human tissue *ex vivo*, including gastrointestinal tract, thyroid, breast, and kidney; comparing OCT/OCM images with the gold standard histology to identify the characteristic features of pathology [135, 217-219]. During the last contract period, we developed advanced technology for OCM which dramatically improves image acquisition data rates.

High Speed Fourier Domain Optical Coherence Microscopy

In standard microscopy, features are viewed in the *en face* plane at a given depth. Therefore, although Fourier domain OCT methods perform superior to time domain due to the ability to image many depths in parallel, if the image is to be acquired from only a single depth, this advantage is not readily appreciable. In addition, since each pixel in an *en face* image requires an A-scan, extremely high imaging speeds are required. For this reason, first generation Fourier domain OCT systems were not suitable for OCM and this delayed the development of Fourier domain OCM techniques. However, with advances in light source and detection technology, it is now possible to reach axial scan rates of several hundred kHz to MHz. Fourier domain OCM has the advantage that images from multiple depths are acquired simultaneously, such several *en face* planes can be acquired without the need for repeated scanning or mechanically translating the interferometer reference arm. In addition to greatly decreasing the time required to volumetrically image the sample, this also significantly relaxes the need to match the coherence gate depth position and the focal plane depth position. This is an important feature for integrating the technology with confocal, fluorescence and nonlinear microscopes, which usually have variations of path length with scanning. In addition, the ability to measure phase of the back reflected light also enables numerical algorithms that can correct for aberrations or the defocusing effects. During the last contract period we investigated the development of Fourier domain OCM technology in both swept source and spectral domain configurations for pathology imaging.

The first demonstration of swept source OCM was performed by our group in 2007 using a high speed Fourier-domain mode-locked (FDML) laser [220]. OCM imaging was performed at 42 kHz axial scan rate, with imaging resolutions of $1.6\text{ }\mu\text{m} \times 8\text{ }\mu\text{m}$ (transverse \times axial) over a $\sim 220\text{ }\mu\text{m} \times 220\text{ }\mu\text{m}$ field of view. More recently our collaboration with Praevium / Thorlabs on the development of high speed VCSEL swept source technology has allowed us to substantially improve the performance over earlier swept source OCM [221, 222]. The VCSEL laser supports variable sweep rates from 50 kHz to 1.2 MHz while maintaining a sweep range of $>100\text{ nm}$. We have demonstrated swept source OCM using the VCSEL light source at both 1050 nm and 1310

nm wavelengths, with an axial scan rate of 100 kHz and 560 kHz, respectively, with an adjustable transverse resolution between 0.86 μm to 3.42 μm and an axial resolution of 8.1 μm , comparable to conventional histological sections [223].

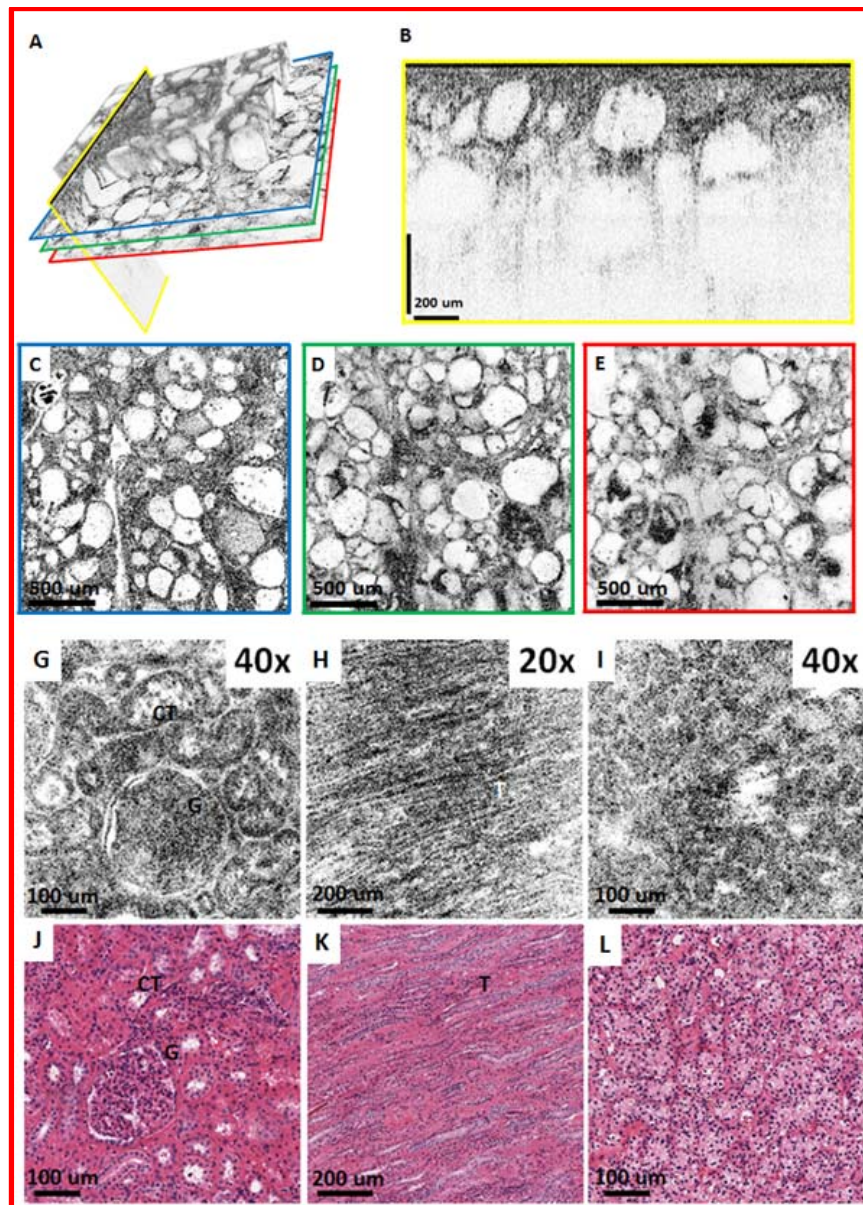


Figure 48: (A-E): Depth resolved OCM imaging of a fresh *ex vivo* human thyroid specimen, with a 10X objective, (A) Volume rendering emphasizing that arbitrary planes can be selected for visualization. For the imaging planes indicated by the colored lines, reconstructed cross-sectional and *en face* images are shown in (B-E). (C-E) are *en face* images from 50 μm , 130 μm and 180 μm below the surface of the specimen, respectively. The cross-sectional image in (B) is displayed using logarithmic scale, whereas (C-E) are displayed using square root scale. (G-J): Ex-vivo OCM images (G-I) and corresponding histology (J-L) from fresh normal human kidney (G, H, J, K) and clear cell renal cell carcinoma specimens (I, L) specimen obtained using 40X (G, I) and 20X (H) water immersion objectives. (G, I, J, L) are from renal cortex, whereas (H, K) are from renal medulla. CT: Convolved tubules, G: Glomerulus, T: Collecting ducts.

Figure 48 shows representative images taken with at 1310 nm using VCSEL OCM with 10X (**Figure 48 (A-E)**), 20X (**Figure 48 (G, I)**) and 40X (**Figure 48 (H)**) objectives. With a 560 kHz axial scan rate and an axial scan sampling density of 1024 x 1024 pixels, an imaging rate of ~0.5 volumes per second was achieved. In **Figure 46 (A)**, a volumetric rendering of an OCM dataset taken from freshly excised normal human thyroid sample is shown. From this dataset one can either construct images in the *en face* direction, similar to standard microscopy (**Figure 48 (C-E)**), or cross-sectional images with very high transverse resolution (**Figure 48 (B)**). Furthermore, it is possible to digitally scan in depth to visualize *en face* images from multiple depths (**Figure 48 (C-E)**). For example, **Figure 48 (G-L)** shows images from fresh human kidney specimens, demonstrating the ability of SS-OCM to generate structural images with close resemble standard H&E staining in fixed specimens.

Similar results can also be achieved using spectral domain OCM. Spectral domain detection has the advantage that extremely broadband light sources are readily available around 800 nm, which enables very high axial resolutions ($<5\ \mu\text{m}$) that is not yet attainable with swept source technology, however axial scan rates are limited by the speed of line scan camera technology. We have developed a SD-OCM system using a superluminescent diode (SLD) light source that provides a 4.2 μm axial resolution [224]. This system operated at a 210 kHz axial scan rate, which is significantly faster than most spectral domain systems, but because each pixel in the *en face* image requires an axial scan, the *en face* frame rates were limited.

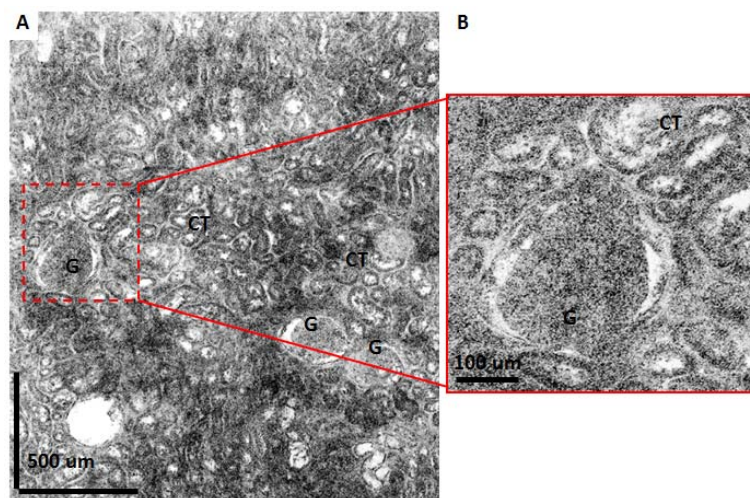


Figure 49. Large field mosaic OCM image of a normal human kidney specimen. Image is constructed by merging 30 frames taken with the 40X/W objective producing a total field of 1.8 mm x 2.1 mm. (B) shows a zoomed view for the region shown with dashed lines in (A). CT: Convolved tubules, G: Glomerulus.

Image Tiling and Display for Large Field of View

OCM at high numerical aperture has a limited field of view similar to MPM. Even using a moderate power 20X objective it is difficult to achieve more than 1 mm² FOV, which limits the ability to evaluate large specimens which may be several cm in dimension. The FOV of OCM can be increased by post-processing and tiling multiple smaller fields together [223, 224]. **Figure 49** shows a large field of view, high resolution OCM image of human kidney constructed from smaller fields that have been tiled together. The image was generated by combining 30 frames acquired with a 40X objective to obtain a 1.8 mm by 2.1 mm total field. Glomeruli and convoluted tubules can be observed throughout the imaging field, consistent with the

characteristics of normal renal cortex. As previously described, the deep zoom display format allows the user to pan around the image and zoom to regions of interest enabling a more detailed examination. **Figure 49 (B)** shows an example where a region with a glomerulus surrounded by convoluting tubules is enlarged to show finer details.

7.0 Other Collaborations

7.1 Computer-aided Diagnosis of Plaque Erosion

The two most frequent underlying mechanisms for sudden cardiac death and acute coronary syndrome (ACS) are plaque rupture and plaque erosion [225-227]. Plaque rupture has been well characterized both *ex vivo* and *in vivo* [225, 228]. However, an *in vivo* diagnosis of plaque erosion in patients with ACS had not been possible due to the lack of a diagnostic modality. Recently, *in vivo* diagnosis of plaque erosion has become possible using intravascular OCT [6, 229]. However, the diagnostic algorithm used in the study was based on qualitative morphological assessment, which has potentially high inter- and intra-observer variability. Plaque erosion has distinct pathologic properties including proteoglycan-rich and smooth muscle cell-rich fibrous regions lacking a superficial endothelial layer [226, 227, 230]. We hypothesized that quantitative diagnostic metrics of superficial tissue properties can provide more objective criteria, which may enhance *in vivo* diagnosis of plaque erosion. Furthermore, quantitative metrics can allow for multiple time point comparisons of the same lesion, which may advance our understanding of natural history of plaque erosion and its response to treatment.

Working in collaboration with Massachusetts General Hospital (MGH) OCT Registry led by Dr. Ik-Kyung Jang, we have developed an algorithm for *in vivo* quantitative diagnosis of plaque erosion. The MGH OCT Registry is an international collaborative effort with the aim to facilitate clinical intravascular OCT research for coronary artery diagnosis and treatment. The registry involves more than 20 international sites, with a clinical intravascular OCT database of around 3000 cases.

A total of 42 patients with ACS caused by plaque erosion were included in the study [229]. Plaque erosion was identified according to the previously established OCT criteria. Non-eroded fibrous plaques remote from the erosion site within the same vessel were used as controls (**Figure 50**). Both optical properties and morphological features of the focal eroded region as well as erosion-adjacent region were quantified and compared between plaque erosion and control fibrous caps. In addition, a logistic regression model was developed upon selected features for automated classification of plaque erosion. Compared to control plaques, eroded plaques have significantly lower surface intensity ($p < 0.001$), lower region of interest (ROI) intensity ($p < 0.001$), lower surface normalized standard deviation (NSD) ($p < 0.001$), lower ROI NSD ($p < 0.001$), higher optical attenuation ($p < 0.001$), larger tissue protrusion area ($p < 0.001$) and greater surface roughness ($p < 0.001$) (**Figure 51**). Erosion-adjacent regions also have lower ROI NSD ($p = 0.008$), higher attenuation ($p < 0.001$), and greater surface roughness ($p = 0.005$). Using the logistic regression model built upon the quantitative features, plaque erosion can be accurately classified against intact fibrous plaques (sensitivity: 100%, specificity: 95.2%), and the likelihood of plaque erosion can be determined to facilitate diagnosis (**Figure 52**). The entire vessel can also be automatically labeled in a continuous colormap indicating the likelihood of plaque erosion (**Figure 53**).

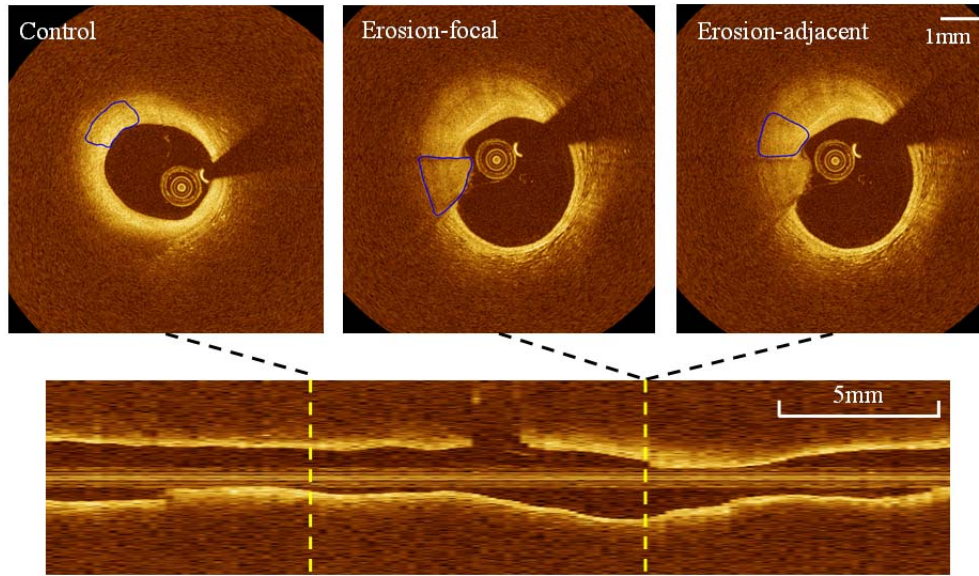


Figure 50. Representative cases of plaque erosion and a control fibrous plaque. Examples of plaque erosion and a control fibrous plaque included for analysis. ROIs were traced (blue contour) in the erosion-focal, erosion-adjacent region, and in a control fibrous plaque remote (≥ 5 mm) from the culprit site.

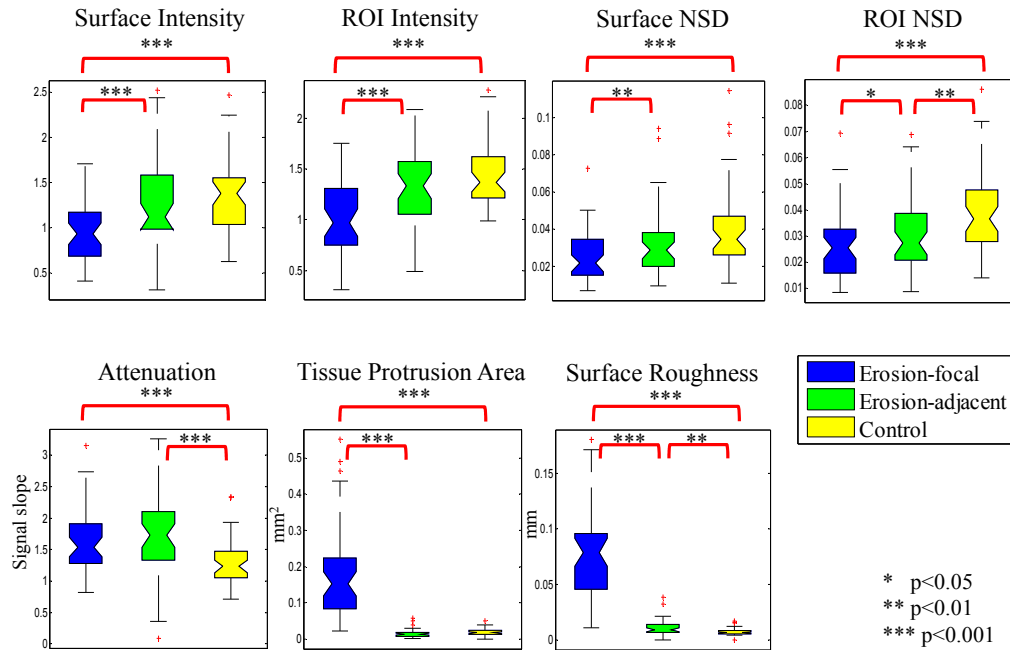


Figure 51. Quantitative comparison of optical and morphological properties between plaque erosion-focal, erosion-adjacent, and control fibrous plaques. Significant optical and morphological differences are observed in all the metrics between erosion-focal and control regions. Erosion-adjacent regions also have significantly lower ROI NSD, higher attenuation and greater surface roughness compared with control. Erosion-focal regions have significantly lower surface intensity, lower ROI intensity, lower surface NSD, lower ROI NSD, larger protrusion area, and greater surface roughness compared with erosion-adjacent region. All the intensity values of a lesion are normalized to the intensity of the image foreground.

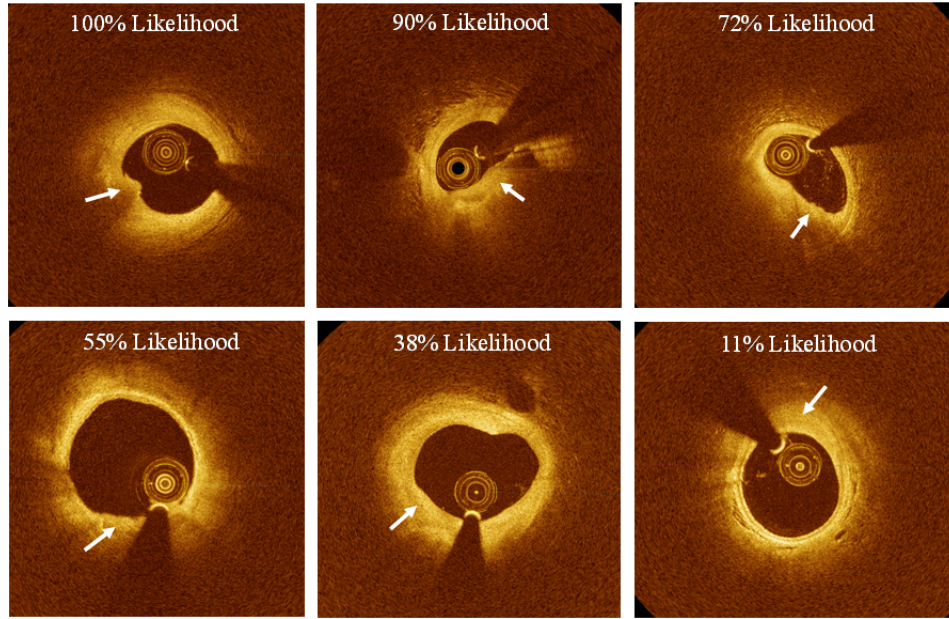


Figure 52. Classification of plaque erosion by the logistic regression model. Examples of plaque erosion (or non-eroded fibrous plaques) with likelihood ranging from 100% to 11% as determined by the logistic regression model. The likelihood of plaque erosion can be used to risk stratify the lesion progression. Definite erosion can be classified by simple thresholding (e.g., use 50% as the cut-off value).

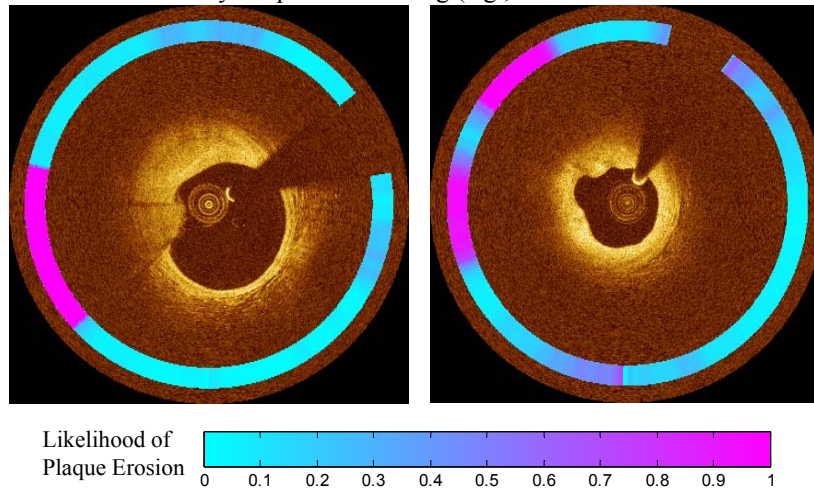


Figure 53. Automated labeling of plaque erosion. Two examples of OCT images are labeled automatically for the likelihood of plaque erosion using the proposed algorithm. At each angular position, the region of interest (ROI) was selected automatically as a 10 degree region bounded radially by the lumen boundary and the vessel wall. The algorithm was then applied to the ROI and the likelihood of plaque erosion can be generated for this position. The entire vessel can therefore be automatically labeled in a continuous colormap indicating the likelihood of plaque erosion.

This newly developed algorithm promises to make the diagnosis of plaque erosion more accurate, consistent, and simple. With the ability to make a real time diagnosis, cardiologists will be able to develop treatment strategies tailored for each individual patient. Future studies will be focused on validating the algorithm by histopathology studies, and applying the algorithm to large clinical trials to correlate the prevalence of plaque erosion to clinical presentations.

7.2 OCT for Evaluation of Kidney Transplantation

There is currently a worldwide shortage of kidneys for transplantation due mainly to the fact that there is no reliable means to determine their viability (i.e. kidneys from non-living donors). Also, following transplantation, kidneys often do not function immediately and their functional status is unclear. In studies during an earlier contract period, working in collaboration with Prof. Yu Chen at University of Maryland (formerly a postdoctoral associate in our group) and Prof. Peter Andrews at Georgetown University, we investigated ultrahigh resolution OCT imaging of kidney microstructure in the rat to investigate the effect of renal ischemia, modeling that which occurs in kidney transplantation. 3D-OCT enabled visualization of the morphology of the uriniferous tubules and the renal corpuscles. OCT revealed dramatic shrinkage of tubular lumens due to swelling of the lining epithelium during ischemic injury and 3D visualization and volumetric rendering software quantitatively measured volumetric changes in tubular lumens in response to renal ischemia. Intravenous infusion of mannitol resulted in thinning of the tubular walls and an increase in the tubular lumen diameters. Mannitol also prevented cell swelling that otherwise resulted in shrinkage of proximal tubule lumens during ischemia. These studies showed that OCT could be used to quantitatively measure structural markers which were candidate markers for kidney viability [231, 232].

Follow on, independent studies by the U. Maryland and Georgetown groups investigated changes in transplant protocol for living donor kidneys to reduce ischemic injury, reducing the time of mannitol administration from 30 to 15 min or less before clamping the renal artery [233]. OCT imaging showed that this change in the timing of mannitol administration protected the human donor proximal tubules from normothermic-induced cell swelling. An evaluation of post-transplant recovery of renal function showed that patients treated with this modified protocol returned to normal renal function significantly faster than those treated with mannitol 30 min or more before clamping the renal artery. The U. Maryland and Georgetown groups invited us to participate in an NIH program (R01 DK094877-01, “Non-invasive evaluation of transplant kidney using OCT”, P.I. Peter Andrews) which is aimed at developing and applying advanced OCT imaging technology including Doppler OCT and OCTA to assess structural and functional markers of kidney function in transplant surgery.

We and our collaborators are continuing developing advanced ultrahigh speed swept source OCT technology to evaluate the structural and functional markers in human donor kidneys prior to and following renal transplant. These imaging studies will be correlated with post-transplant renal function in order to develop imaging guidelines and associated algorithms for OCT evaluation of kidney viability for transplant. The proposed studies will increase the number of healthy kidneys available for transplantation by making the most efficient use of available donor kidneys, eliminating the possible use of bad donor kidneys (i.e., excessively damaged ischemic or diseased kidneys), providing a measure of expected post-transplant renal function, and allowing better distinction between post-transplant immunological rejection and ischemic-induced acute renal failure.

Although the initial research leading to this program was performed in 2007, this is an example of the longer term impact of AFOSR funding on clinical care as well as new program development.

8.0 Publications under AFOSR Program from 2011 to 2014

- [1] B. Baumann, B. Potsaid, M. F. Kraus, J. J. Liu, D. Huang, J. Horneegger, A. E. Cable, J. S. Duker, and J. G. Fujimoto, "Total retinal blood flow measurement with ultrahigh speed swept source/Fourier domain OCT," *Biomed Opt Express*, vol. 2, pp. 1539-52, Jun 1 2011.
- [2] J. L. Bradley, S. P. Shah, V. Manjunath, J. G. Fujimoto, J. S. Duker, and E. Reichel, "Ultra-high-resolution optical coherence tomographic findings in commotio retinae," *Arch Ophthalmol*, vol. 129, pp. 107-8, Jan 2011.
- [3] U. Demirbas, M. Schmalz, B. Sumpf, G. Erbert, G. S. Petrich, L. A. Kolodziejski, J. G. Fujimoto, F. X. Kartner, and A. Leitenstorfer, "Femtosecond Cr:LiSAF and Cr:LiCAF lasers pumped by tapered diode lasers," *Opt Express*, vol. 19, pp. 20444-61, Oct 10 2011.
- [4] B. Garita, M. W. Jenkins, M. Han, C. Zhou, M. Vanauker, A. M. Rollins, M. Watanabe, J. G. Fujimoto, and K. K. Linask, "Blood flow dynamics of one cardiac cycle and relationship to mechanotransduction and trabeculation during heart looping," *Am J Physiol Heart Circ Physiol*, vol. 300, pp. H879-91, Mar 2011.
- [5] I. Grulkowski, J. J. Liu, B. Baumann, B. Potsaid, C. Lu, and J. G. Fujimoto, "Imaging limbal and scleral vasculature using Swept Source Optical Coherence Tomography," *Photonics Lett Pol*, vol. 3, pp. 132-134, Jan 1 2011.
- [6] J. Ho, L. Branchini, C. Regatieri, C. Krishnan, J. G. Fujimoto, and J. S. Duker, "Analysis of normal peripapillary choroidal thickness via spectral domain optical coherence tomography," *Ophthalmology*, vol. 118, pp. 2001-7, Oct 2011.
- [7] J. Ho, A. J. Witkin, J. Liu, Y. Chen, J. G. Fujimoto, J. S. Schuman, and J. S. Duker, "Documentation of intraretinal retinal pigment epithelium migration via high-speed ultrahigh-resolution optical coherence tomography," *Ophthalmology*, vol. 118, pp. 687-93, Apr 2011.
- [8] C. H. Judson, L. N. Vuong, I. Gorczynska, V. J. Srinivasan, J. G. Fujimoto, and J. S. Duker, "Intact Retinal Tissue and Retinal Pigment Epithelium Identified within a Coloboma Via High-Speed, Ultrahigh Resolution Optical Coherence Tomography," *Retin Cases Brief Rep*, vol. 5, pp. 46-48, Winter 2011.
- [9] A. Li, C. Zhou, J. Moore, P. Zhang, T. H. Tsai, H. C. Lee, D. M. Romano, M. L. McKee, D. A. Schoenfeld, M. J. Serra, K. Raygor, H. F. Cantiello, J. G. Fujimoto, and R. E. Tanzi, "Changes in the expression of the Alzheimer's disease-associated presenilin gene in drosophila heart leads to cardiac dysfunction," *Curr Alzheimer Res*, vol. 8, pp. 313-22, May 2011.
- [10] Y. Y. Liu, H. Ishikawa, M. Chen, G. Wollstein, J. S. Duker, J. G. Fujimoto, J. S. Schuman, and J. M. Rehg, "Computerized macular pathology diagnosis in spectral domain optical coherence tomography scans based on multiscale texture and shape features," *Invest Ophthalmol Vis Sci*, vol. 52, pp. 8316-22, 2011.
- [11] H. C. Lowe, J. Narula, J. G. Fujimoto, and I. K. Jang, "Intracoronary optical diagnostics current status, limitations, and potential," *JACC Cardiovasc Interv*, vol. 4, pp. 1257-70, Dec 2011.
- [12] V. Manjunath, J. Goren, J. G. Fujimoto, and J. S. Duker, "Analysis of choroidal thickness in age-related macular degeneration using spectral-domain optical coherence tomography," *Am J Ophthalmol*, vol. 152, pp. 663-8, Oct 2011.

- [13] V. Manjunath, H. Shah, J. G. Fujimoto, and J. S. Duker, "Analysis of peripapillary atrophy using spectral domain optical coherence tomography," *Ophthalmology*, vol. 118, pp. 531-6, Mar 2011.
- [14] V. Manjunath, M. Taha, J. G. Fujimoto, and J. S. Duker, "Posterior lattice degeneration characterized by spectral domain optical coherence tomography," *Retina*, vol. 31, pp. 492-6, Mar 2011.
- [15] T. H. Tsai, B. Potsaid, M. F. Kraus, C. Zhou, Y. K. Tao, J. Hornegger, and J. G. Fujimoto, "Piezoelectric-transducer-based miniature catheter for ultrahigh-speed endoscopic optical coherence tomography," *Biomed Opt Express*, vol. 2, pp. 2438-48, Aug 1 2011.
- [16] M. A. Yaseen, V. J. Srinivasan, S. Sakadzic, H. Radhakrishnan, I. Gorczynska, W. Wu, J. G. Fujimoto, and D. A. Boas, "Microvascular oxygen tension and flow measurements in rodent cerebral cortex during baseline conditions and functional activation," *J Cereb Blood Flow Metab*, vol. 31, pp. 1051-63, Apr 2011.
- [17] B. Baumann, W. Choi, B. Potsaid, D. Huang, J. S. Duker, and J. G. Fujimoto, "Swept source/Fourier domain polarization sensitive optical coherence tomography with a passive polarization delay unit," *Opt Express*, vol. 20, pp. 10229-41, Apr 23 2012.
- [18] L. Branchini, C. V. Regatieri, I. Flores-Moreno, B. Baumann, J. G. Fujimoto, and J. S. Duker, "Reproducibility of choroidal thickness measurements across three spectral domain optical coherence tomography systems," *Ophthalmology*, vol. 119, pp. 119-23, Jan 2012.
- [19] Y. Chen, S. W. Huang, C. Zhou, B. Potsaid, and J. G. Fujimoto, "Improved Detection Sensitivity of Line-Scanning Optical Coherence Microscopy," *IEEE J Sel Top Quantum Electron*, vol. 18, pp. 1094-1099, May 1 2012.
- [20] W. Choi, B. Baumann, J. J. Liu, A. C. Clermont, E. P. Feener, J. S. Duker, and J. G. Fujimoto, "Measurement of pulsatile total blood flow in the human and rat retina with ultrahigh speed spectral/Fourier domain OCT," *Biomed Opt Express*, vol. 3, pp. 1047-61, May 1 2012.
- [21] W. Choi, B. Baumann, E. A. Swanson, and J. G. Fujimoto, "Extracting and compensating dispersion mismatch in ultrahigh-resolution Fourier domain OCT imaging of the retina," *Opt Express*, vol. 20, pp. 25357-68, Nov 5 2012.
- [22] L. S. Folio, G. Wollstein, H. Ishikawa, R. A. Bilonick, Y. Ling, L. Kagemann, R. J. Noecker, J. G. Fujimoto, and J. S. Schuman, "Variation in optical coherence tomography signal quality as an indicator of retinal nerve fibre layer segmentation error," *Br J Ophthalmol*, vol. 96, pp. 514-8, Apr 2012.
- [23] I. Grulkowski, J. J. Liu, B. Potsaid, V. Jayaraman, C. D. Lu, J. Jiang, A. E. Cable, J. S. Duker, and J. G. Fujimoto, "Retinal, anterior segment and full eye imaging using ultrahigh speed swept source OCT with vertical-cavity surface emitting lasers," *Biomed Opt Express*, vol. 3, pp. 2733-51, Nov 1 2012.
- [24] Y. Jia, J. C. Morrison, J. Tokayer, O. Tan, L. Lombardi, B. Baumann, C. D. Lu, W. Choi, J. G. Fujimoto, and D. Huang, "Quantitative OCT angiography of optic nerve head blood flow," *Biomed Opt Express*, vol. 3, pp. 3127-37, Dec 1 2012.
- [25] Y. Jia, O. Tan, J. Tokayer, B. Potsaid, Y. Wang, J. J. Liu, M. F. Kraus, H. Subhash, J. G. Fujimoto, J. Hornegger, and D. Huang, "Split-spectrum amplitude-decorrelation angiography with optical coherence tomography," *Opt Express*, vol. 20, pp. 4710-25, Feb 13 2012.

- [26] Y. L. Jia, J. C. Morrison, J. Tokayer, O. Tan, L. Lombardi, B. Baumann, C. D. Lu, W. Choi, J. G. Fujimoto, and D. Huang, "Quantitative OCT angiography of optic nerve head blood flow," *Biomedical Optics Express*, vol. 3, Dec 2012.
- [27] M. F. Kraus, B. Potsaid, M. A. Mayer, R. Bock, B. Baumann, J. J. Liu, J. Hornegger, and J. G. Fujimoto, "Motion correction in optical coherence tomography volumes on a per A-scan basis using orthogonal scan patterns," *Biomed Opt Express*, vol. 3, pp. 1182-99, Jun 1 2012.
- [28] H. C. Lee, C. Zhou, D. W. Cohen, A. E. Mondelblatt, Y. Wang, A. D. Aguirre, D. Shen, Y. Sheikine, J. G. Fujimoto, and J. L. Connolly, "Integrated optical coherence tomography and optical coherence microscopy imaging of ex vivo human renal tissues," *J Urol*, vol. 187, pp. 691-9, Feb 2012.
- [29] D. Li, U. Demirbas, A. Benedick, A. Sennaroglu, J. G. Fujimoto, and F. X. Kartner, "Attosecond timing jitter pulse trains from semiconductor saturable absorber mode-locked Cr:LiSAF lasers," *Opt Express*, vol. 20, pp. 23422-35, Oct 8 2012.
- [30] C. V. Regatieri, L. Branchini, J. Carmody, J. G. Fujimoto, and J. S. Duker, "Choroidal thickness in patients with diabetic retinopathy analyzed by spectral-domain optical coherence tomography," *Retina*, vol. 32, pp. 563-8, Mar 2012.
- [31] C. V. Regatieri, L. Branchini, J. G. Fujimoto, and J. S. Duker, "Choroidal imaging using spectral-domain optical coherence tomography," *Retina*, vol. 32, pp. 865-76, May 2012.
- [32] V. Sebastian, S. K. Lee, C. Zhou, M. F. Kraus, J. G. Fujimoto, and K. F. Jensen, "One-step continuous synthesis of biocompatible gold nanorods for optical coherence tomography," *Chem Commun (Camb)*, vol. 48, pp. 6654-6, Jul 7 2012.
- [33] T. H. Tsai, C. Zhou, H. C. Lee, Y. K. Tao, O. O. Ahsen, M. Figueiredo, D. C. Adler, J. M. Schmitt, Q. Huang, J. G. Fujimoto, and H. Mashimo, "Comparison of Tissue Architectural Changes between Radiofrequency Ablation and Cryospray Ablation in Barrett's Esophagus Using Endoscopic Three-Dimensional Optical Coherence Tomography," *Gastroenterol Res Pract*, vol. 2012, p. 684832, 2012.
- [34] T. H. Tsai, C. Zhou, Y. K. Tao, H. C. Lee, O. O. Ahsen, M. Figueiredo, T. Kirtane, D. C. Adler, J. M. Schmitt, Q. Huang, J. G. Fujimoto, and H. Mashimo, "Structural markers observed with endoscopic 3-dimensional optical coherence tomography correlating with Barrett's esophagus radiofrequency ablation treatment response (with videos)," *Gastrointest Endosc*, vol. 76, pp. 1104-12, Dec 2012.
- [35] G. Wollstein, L. Kagemann, R. A. Bilonick, H. Ishikawa, L. S. Folio, M. L. Gabriele, A. K. Ungar, J. S. Duker, J. G. Fujimoto, and J. S. Schuman, "Retinal nerve fibre layer and visual function loss in glaucoma: the tipping point," *Br J Ophthalmol*, vol. 96, pp. 47-52, Jan 2012.
- [36] C. Zhou, T. Kirtane, T. H. Tsai, H. C. Lee, D. C. Adler, J. Schmitt, Q. Huang, J. G. Fujimoto, and H. Mashimo, "Three-dimensional endoscopic optical coherence tomography imaging of cervical inlet patch," *Gastrointest Endosc*, vol. 75, pp. 675-7; discussion 677, Mar 2012.
- [37] C. Zhou, T. H. Tsai, H. C. Lee, T. Kirtane, M. Figueiredo, Y. K. Tao, O. O. Ahsen, D. C. Adler, J. M. Schmitt, Q. Huang, J. G. Fujimoto, and H. Mashimo, "Characterization of buried glands before and after radiofrequency ablation by using 3-dimensional optical coherence tomography (with videos)," *Gastrointest Endosc*, vol. 76, pp. 32-40, Jul 2012.

- [38] M. Adhi, J. J. Liu, A. H. Qavi, I. Grulkowski, J. G. Fujimoto, and J. S. Duker, "Enhanced Visualization of the Choroido-Scleral Interface Using Swept-Source OCT," *Ophthalmic Surg Lasers Imaging Retina*, vol. 44, pp. S40-2, 2013/11 2013.
- [39] O. O. Ahsen, Y. K. Tao, B. M. Potsaid, Y. Sheikine, J. Jiang, I. Grulkowski, T. H. Tsai, V. Jayaraman, M. F. Kraus, J. L. Connolly, J. Horneegger, A. Cable, and J. G. Fujimoto, "Swept source optical coherence microscopy using a 1310 nm VCSEL light source," *Opt Express*, vol. 21, pp. 18021-33, 2013/7 2013.
- [40] A. A. Alwassia, M. Adhi, J. Y. Zhang, C. V. Regatieri, A. Al-Quthami, D. Salem, J. G. Fujimoto, and J. S. Duker, "Exercise-induced acute changes in systolic blood pressure do not alter choroidal thickness as measured by a portable spectral-domain optical coherence tomography device," *Retina*, vol. 33, pp. 160-5, 2013/1 2013.
- [41] L. Branchini, C. Regatieri, M. Adhi, I. Flores-Moreno, V. Manjunath, J. G. Fujimoto, and J. S. Duker, "Effect of intravitreal anti-vascular endothelial growth factor therapy on choroidal thickness in neovascular age-related macular degeneration using spectral-domain optical coherence tomography," *JAMA Ophthalmol*, vol. 131, pp. 693-4, 2013/5 2013.
- [42] L. A. Branchini, M. Adhi, C. V. Regatieri, N. Nandakumar, J. J. Liu, N. Laver, J. G. Fujimoto, and J. S. Duker, "Analysis of choroidal morphologic features and vasculature in healthy eyes using spectral-domain optical coherence tomography," *Ophthalmology*, vol. 120, pp. 1901-8, 2013/9 2013.
- [43] C. L. Chen, H. Ishikawa, Y. Ling, G. Wollstein, R. A. Bilonick, J. Xu, J. G. Fujimoto, I. A. Sigal, L. Kagemann, and J. S. Schuman, "Signal normalization reduces systematic measurement differences between spectral-domain optical coherence tomography devices," *Invest Ophthalmol Vis Sci*, vol. 54, pp. 7317-22, 2013/11 2013.
- [44] W. Choi, K. J. Mohler, B. Potsaid, C. D. Lu, J. J. Liu, V. Jayaraman, A. E. Cable, J. S. Duker, R. Huber, and J. G. Fujimoto, "Choriocapillaris and Choroidal Microvasculature Imaging with Ultrahigh Speed OCT Angiography," *PLoS One*, vol. 8, p. e81499, 2013/12/19 2013.
- [45] W. Choi, B. Potsaid, V. Jayaraman, B. Baumann, I. Grulkowski, J. J. Liu, C. D. Lu, A. E. Cable, D. Huang, J. S. Duker, and J. G. Fujimoto, "Phase-sensitive swept-source optical coherence tomography imaging of the human retina with a vertical cavity surface-emitting laser light source," *Opt Lett*, vol. 38, pp. 338-40, 2013/2 2013.
- [46] A. Devor, P. A. Bandettini, D. A. Boas, J. M. Bower, R. B. Buxton, L. B. Cohen, A. M. Dale, G. T. Einevoll, P. T. Fox, M. A. Franceschini, K. J. Friston, J. G. Fujimoto, M. A. Geyer, J. H. Greenberg, E. Halgren, M. S. Hamalainen, F. Helmchen, B. T. Hyman, A. Jasanoff, T. L. Jernigan, L. L. Judd, S. G. Kim, D. Kleinfeld, N. J. Kopell, M. Kutas, K. K. Kwong, M. E. Larkum, E. H. Lo, P. J. Magistretti, J. B. Mandeville, E. Masliah, P. P. Mitra, W. C. Mobley, M. A. Moskowitz, A. Nimmerjahn, J. H. Reynolds, B. R. Rosen, B. M. Salzberg, C. B. Schaffer, G. A. Silva, P. T. So, N. C. Spitzer, R. B. Tootell, D. C. Van Essen, W. Vanduffel, S. A. Vinogradov, L. L. Wald, L. V. Wang, B. Weber, and A. G. Yodh, "The challenge of connecting the dots in the B.R.A.I.N.," *Neuron*, vol. 80, pp. 270-4, 2013/10/16 2013.
- [47] D. Ferrara, K. J. Mohler, N. Waheed, M. Adhi, J. J. Liu, I. Grulkowski, M. F. Kraus, C. Bauman, J. Horneegger, J. G. Fujimoto, and J. S. Duker, "En Face Enhanced-Depth Swept-Source Optical Coherence Tomography Features of Chronic Central Serous Chorioretinopathy," *Ophthalmology*, 2013/11/26 2013.

- [48] I. Grulkowski, J. J. Liu, B. Potsaid, V. Jayaraman, J. Jiang, J. G. Fujimoto, and A. E. Cable, "High-precision, high-accuracy ultralong-range swept-source optical coherence tomography using vertical cavity surface emitting laser light source," *Opt Lett*, vol. 38, pp. 673-5, 2013/3 2013.
- [49] I. Grulkowski, J. J. Liu, J. Y. Zhang, B. Potsaid, V. Jayaraman, A. E. Cable, J. S. Duker, and J. G. Fujimoto, "Reproducibility of a long-range swept-source optical coherence tomography ocular biometry system and comparison with clinical biometers," *Ophthalmology*, vol. 120, pp. 2184-90, 2013/11 2013.
- [50] V. Kajic, M. Esmaelpour, C. Glittenberg, M. F. Kraus, J. Honegger, R. Othara, S. Binder, J. G. Fujimoto, and W. Drexler, "Automated three-dimensional choroidal vessel segmentation of 3D 1060 nm OCT retinal data," *Biomed Opt Express*, vol. 4, pp. 134-50, 2013/1 2013.
- [51] H. C. Lee, J. J. Liu, Y. Sheikine, A. D. Aguirre, J. L. Connolly, and J. G. Fujimoto, "Ultrahigh speed spectral-domain optical coherence microscopy," *Biomed Opt Express*, vol. 4, pp. 1236-54, 2013/9/07 2013.
- [52] A. R. Li, O. O. Ahsen, J. J. Liu, C. Du, M. L. McKee, Y. Yang, W. Wasco, C. H. Newton-Cheh, C. J. O'Donnell, J. G. Fujimoto, C. Zhou, and R. E. Tanzi, "Silencing of the *Drosophila* ortholog of SOX5 in heart leads to cardiac dysfunction as detected by optical coherence tomography," *Human Molecular Genetics*, vol. 22, pp. 3798-3806, 2013/9 2013.
- [53] J. J. Liu, I. Grulkowski, M. F. Kraus, B. Potsaid, C. D. Lu, B. Baumann, J. S. Duker, J. Honegger, and J. G. Fujimoto, "In vivo imaging of the rodent eye with swept source/Fourier domain OCT," *Biomed Opt Express*, vol. 4, pp. 351-63, 2013/2 2013.
- [54] C. D. Lu, M. F. Kraus, B. Potsaid, J. J. Liu, W. Choi, V. Jayaraman, A. E. Cable, J. Honegger, J. S. Duker, and J. G. Fujimoto, "Handheld ultrahigh speed swept source optical coherence tomography instrument using a MEMS scanning mirror," *Biomed Opt Express*, vol. 5, pp. 293-311, Dec 20 2013.
- [55] Z. Nadler, B. Wang, G. Wollstein, J. E. Nevins, H. Ishikawa, L. Kagemann, I. A. Sigal, R. D. Ferguson, D. X. Hammer, I. Grulkowski, J. J. Liu, M. F. Kraus, C. D. Lu, J. Honegger, J. G. Fujimoto, and J. S. Schuman, "Automated lamina cribrosa microstructural segmentation in optical coherence tomography scans of healthy and glaucomatous eyes," *Biomed Opt Express*, vol. 4, pp. 2596-608, 2013/12/04 2013.
- [56] T. H. Tsai, B. Potsaid, Y. K. Tao, V. Jayaraman, J. Jiang, P. J. Heim, M. F. Kraus, C. Zhou, J. Honegger, H. Mashimo, A. E. Cable, and J. G. Fujimoto, "Ultrahigh speed endoscopic optical coherence tomography using micromotor imaging catheter and VCSEL technology," *Biomed Opt Express*, vol. 4, pp. 1119-32, 2013/7 2013.
- [57] B. Wang, J. E. Nevins, Z. Nadler, G. Wollstein, H. Ishikawa, R. A. Bilonick, L. Kagemann, I. A. Sigal, I. Grulkowski, J. J. Liu, M. Kraus, C. D. Lu, J. Honegger, J. G. Fujimoto, and J. S. Schuman, "In vivo lamina cribrosa micro-architecture in healthy and glaucomatous eyes as assessed by optical coherence tomography," *Invest Ophthalmol Vis Sci*, vol. 54, pp. 8270-4, 2013/12 2013.
- [58] E. Wei, Y. Jia, O. Tan, B. Potsaid, J. J. Liu, W. Choi, J. G. Fujimoto, and D. Huang, "Parafoveal Retinal Vascular Response to Pattern Visual Stimulation Assessed with OCT Angiography," *PLoS One*, vol. 8, p. e81343, 2013/12/07 2013.
- [59] T. Yonetsu, B. E. Bouma, K. Kato, J. G. Fujimoto, and I. K. Jang, "Optical Coherence Tomography - 15 Years in Cardiology," *Circulation Journal*, vol. 77, pp. 1933-1940, 2013/8 2013.

- [60] M. Adhi, J. J. Liu, A. H. Qavi, I. Grulkowski, C. D. Lu, K. J. Mohler, D. Ferrara, M. F. Kraus, C. R. Bauman, A. J. Witkin, N. K. Waheed, J. Hornegger, J. G. Fujimoto, and J. S. Duker, "Choroidal Analysis in Healthy Eyes Using Swept-Source Optical Coherence Tomography Compared to Spectral Domain Optical Coherence Tomography," *American Journal of Ophthalmology*, vol. 157, pp. 1272-1281, Jun 2014.
- [61] O. O. Ahsen, H. C. Lee, M. G. Giacomelli, Z. Wang, K. C. Liang, T. H. Tsai, B. Potsaid, H. Mashimo, and J. G. Fujimoto, "Correction of rotational distortion for catheter-based en face OCT and OCT angiography," *Optics Letters*, vol. 39, pp. 5973-5976, Oct 15 2014.
- [62] M. Esmaeelpour, S. Ansari-Shahrezaei, C. Glittenberg, S. Nemetz, M. F. Kraus, J. Hornegger, J. G. Fujimoto, W. Drexler, and S. Binder, "Choroid, Haller's, and Sattler's Layer Thickness in Intermediate Age-Related Macular Degeneration With and Without Fellow Neovascular Eyes," *Investigative Ophthalmology & Visual Science*, vol. 55, pp. 5074-5080, Aug 2014.
- [63] M. Esmaeelpour, V. Kajic, B. Zabihian, R. Othara, S. Ansari-Shahrezaei, L. Kellner, I. Krebs, S. Nemetz, M. F. Kraus, J. Hornegger, J. G. Fujimoto, W. Drexler, and S. Binder, "Choroidal Haller's and Sattler's Layer Thickness Measurement Using 3-Dimensional 1060-nm Optical Coherence Tomography," *Plos One*, vol. 9, Jun 9 2014.
- [64] J. G. Fein, L. A. Branchini, V. Manjunath, C. V. Regatieri, J. G. Fujimoto, and J. S. Duker, "Analysis of Short-Term Change in Subfoveal Choroidal Thickness in Eyes With Age-Related Macular Degeneration Using Optical Coherence Tomography," *Ophthalmic Surgery Lasers & Imaging*, vol. 45, pp. 32-37, Jan-Feb 2014.
- [65] D. Ferrara, K. J. Mohler, N. Waheed, M. Adhi, J. J. Liu, I. Grulkowski, M. F. Kraus, C. Bauman, J. Hornegger, J. G. Fujimoto, and J. S. Duker, "En Face Enhanced-Depth Swept-Source Optical Coherence Tomography Features of Chronic Central Serous Choroidopathy," *Ophthalmology*, vol. 121, pp. 719-726, Mar 2014.
- [66] Y. Jia, E. Wei, X. Wang, X. Zhang, J. C. Morrison, M. Parikh, L. H. Lombardi, D. M. Gattey, R. L. Armour, B. Edmunds, M. F. Kraus, J. G. Fujimoto, and D. Huang, "Optical Coherence Tomography Angiography of Optic Disc Perfusion in Glaucoma," *Ophthalmology*, Mar 11 2014.
- [67] Y. L. Jia, S. T. Bailey, D. J. Wilson, O. Tan, M. L. Klein, C. J. Flaxel, B. Potsaid, J. J. Liu, C. D. Lu, M. F. Kraus, J. G. Fujimoto, and D. Huang, "Quantitative Optical Coherence Tomography Angiography of Choroidal Neovascularization in Age-Related Macular Degeneration," *Ophthalmology*, vol. 121, pp. 1435-1444, Jul 2014.
- [68] Y. L. Jia, E. Wei, X. G. Wang, X. B. Zhang, J. C. Morrison, M. Parikh, L. H. Lombardi, D. M. Gattey, R. L. Armour, B. Edmunds, M. F. Kraus, J. G. Fujimoto, and D. Huang, "Optical Coherence Tomography Angiography of Optic Disc Perfusion in Glaucoma," *Ophthalmology*, vol. 121, pp. 1322-1332, Jul 2014.
- [69] M. F. Kraus, J. J. Liu, J. Schottenhamml, C. L. Chen, A. Budai, L. Branchini, T. Ko, H. Ishikawa, G. Wollstein, J. Schuman, J. S. Duker, J. G. Fujimoto, and J. Hornegger, "Quantitative 3D-OCT motion correction with tilt and illumination correction, robust similarity measure and regularization," *Biomedical Optics Express*, vol. 5, pp. 2591-2613, Aug 1 2014.
- [70] J. J. Liu, A. J. Witkin, M. Adhi, I. Grulkowski, M. F. Kraus, A. H. Dhalla, C. D. Lu, J. Hornegger, J. S. Duker, and J. G. Fujimoto, "Enhanced Vitreous Imaging in Healthy Eyes Using Swept Source Optical Coherence Tomography," *Plos One*, vol. 9, Jul 18 2014.

- [71] C. D. Lu, M. F. Kraus, B. Potsaid, J. J. Liu, W. Choi, V. Jayaraman, A. E. Cable, J. Hornegger, J. S. Duker, and J. G. Fujimoto, "Handheld ultrahigh speed swept source optical coherence tomography instrument using a MEMS scanning mirror," *Biomedical Optics Express*, vol. 5, pp. 293-311, Jan 1 2014.
- [72] Y. K. Tao, D. J. Shen, Y. Sheikine, O. O. Ahsen, H. H. Wang, D. B. Schmolze, N. B. Johnson, J. S. Brooker, A. E. Cable, J. L. Connolly, and J. G. Fujimoto, "Assessment of breast pathologies using nonlinear microscopy," *Proceedings of the National Academy of Sciences of the United States of America*, vol. 111, pp. 15304-15309, Oct 28 2014.
- [73] T. H. Tsai, O. O. Ahsen, H. C. Lee, K. C. Liang, M. Figueiredo, Y. K. Tao, M. G. Giacomelli, B. M. Potsaid, V. Jayaraman, Q. Huang, A. E. Cable, J. G. Fujimoto, and H. Mashimo, "Endoscopic Optical Coherence Angiography Enables 3-Dimensional Visualization of Subsurface Microvasculature," *Gastroenterology*, vol. 147, pp. 1219-1221, Dec 2014.
- [74] T. H. Tsai, H. C. Lee, O. O. Ahsen, K. Liang, M. G. Giacomelli, B. Potsaid, Y. K. Tao, V. Jayaraman, M. Figueiredo, Q. Huang, A. Cable, J. G. Fujimoto, and H. Mashimo, "Ultrahigh speed endoscopic optical coherence tomography for gastroenterology," *Biomed. Opt. Express*, vol. 5, pp. 4387-4404, Dec 1 2014.
- [75] R. Vergallo, M. I. Papafaklis, T. Yonetsu, C. V. Bourantas, I. Andreou, Z. Wang, J. G. Fujimoto, I. McNulty, H. Lee, L. M. Biasucci, F. Crea, C. L. Feldman, L. K. Michalis, P. H. Stone, and I. K. Jang, "Endothelial Shear Stress and Coronary Plaque Characteristics in Humans Combined Frequency-Domain Optical Coherence Tomography and Computational Fluid Dynamics Study," *Circulation-Cardiovascular Imaging*, vol. 7, pp. 905-911, Nov 2014.
- [76] B. Wang, J. E. Nevins, Z. Nadler, G. Wollstein, H. Ishikawa, R. A. Bilonick, L. Kagemann, I. A. Sigal, I. Grulkowski, J. J. Liu, M. Kraus, C. D. Lu, J. Hornegger, J. G. Fujimoto, and J. S. Schuman, "Reproducibility of In-Vivo OCT Measured Three-Dimensional Human Lamina Cribrosa Microarchitecture," *Plos One*, vol. 9, Apr 18 2014.
- [77] X. G. Wang, Y. L. Jia, R. Spain, B. Potsaid, J. J. Liu, B. Baumann, J. Hornegger, J. G. Fujimoto, Q. Wu, and D. Huang, "Optical coherence tomography angiography of optic nerve head and parafovea in multiple sclerosis," *British Journal of Ophthalmology*, vol. 98, pp. 1368-1373, Oct 2014.
- [78] Z. Wang, H. B. Jia, J. W. Tian, T. Soeda, R. Vergallo, Y. Minami, H. Lee, A. Aguirre, J. G. Fujimoto, and I. K. Jang, "Computer-Aided Image Analysis Algorithm to Enhance In Vivo Diagnosis of Plaque Erosion by Intravascular Optical Coherence Tomography," *Circulation-Cardiovascular Imaging*, vol. 7, pp. 805-810, Sep 2014.
- [79] Z. Wang, H. C. Lee, O. O. Ahsen, B. Lee, W. Choi, B. Potsaid, J. Liu, V. Jayaraman, A. Cable, M. F. Kraus, K. C. Liang, J. Hornegger, and J. G. Fujimoto, "Depth-encoded all-fiber swept source polarization sensitive OCT," *Biomedical Optics Express*, vol. 5, pp. 2931-2949, Sep 1 2014.
- [80] N. Zhang, T. H. Tsai, O. O. Ahsen, K. Liang, H. C. Lee, P. Xue, X. Li, and J. G. Fujimoto, "Compact piezoelectric transducer fiber scanning probe for optical coherence tomography," *Opt Lett*, vol. 39, pp. 186-8, Jan 15 2014.

References

- [1] E. Moults, W. Choi, N. K. Waheed, M. Adhi, B. Lee, C. D. Lu, V. Jayaraman, B. Potsaid, P. J. Rosenfeld, J. S. Duker, and J. G. Fujimoto, "Ultrahigh-Speed Swept-Source OCT Angiography in Exudative AMD," *Ophthalmic Surg Lasers Imaging Retina*, vol. 45, pp. 496-505, Nov 1 2014.
- [2] T. H. Tsai, O. O. Ahsen, H. C. Lee, K. Liang, M. Figueiredo, Y. K. Tao, M. G. Giacomelli, B. M. Potsaid, V. Jayaraman, Q. Huang, A. E. Cable, J. G. Fujimoto, and H. Mashimo, "Endoscopic Optical Coherence Angiography Enables Three Dimensional Visualization of Subsurface Microvasculature," *Gastroenterology*, Aug 26 2014.
- [3] Y. K. Tao, D. J. Shen, Y. Sheikine, O. O. Ahsen, H. H. Wang, D. B. Schmolze, N. B. Johnson, J. S. Brooker, A. E. Cable, J. L. Connolly, and J. G. Fujimoto, "Assessment of breast pathologies using nonlinear microscopy," *Proceedings of the National Academy of Sciences of the United States of America*, vol. 111, pp. 15304-15309, Oct 28 2014.
- [4] I. Grulkowski, J. J. Liu, B. Potsaid, V. Jayaraman, C. D. Lu, J. Jiang, A. E. Cable, J. S. Duker, and J. G. Fujimoto, "Retinal, anterior segment and full eye imaging using ultrahigh speed swept source OCT with vertical-cavity surface emitting lasers," *Biomed Opt Express*, vol. 3, pp. 2733-51, Nov 1 2012.
- [5] W. Choi, B. Potsaid, V. Jayaraman, B. Baumann, I. Grulkowski, J. J. Liu, C. D. Lu, A. E. Cable, D. Huang, J. S. Duker, and J. G. Fujimoto, "Phase-sensitive swept-source optical coherence tomography imaging of the human retina with a vertical cavity surface-emitting laser light source," *Opt Lett*, vol. 38, pp. 338-40, Feb 1 2013.
- [6] T.-H. Tsai, B. Potsaid, Y. K. Tao, V. Jayaraman, J. Jiang, P. J. S. Heim, M. F. Kraus, C. Zhou, J. Hornegger, H. Mashimo, A. E. Cable, and J. G. Fujimoto, "Ultrahigh speed endoscopic optical coherence tomography using micromotor imaging catheter and VCSEL technology," *Biomedical Optics Express*, vol. 4, pp. 1119-1132, 2013/07/01 2013.
- [7] S. Makita, Y. Hong, M. Yamanari, T. Yatagai, and Y. Yasuno, "Optical coherence angiography," *Opt Express*, vol. 14, pp. 7821-40, Aug 21 2006.
- [8] J. Fingler, D. Schwartz, C. Yang, and S. E. Fraser, "Mobility and transverse flow visualization using phase variance contrast with spectral domain optical coherence tomography," *Opt Express*, vol. 15, pp. 12636-53, Oct 1 2007.
- [9] Y. K. Tao, A. M. Davis, and J. A. Izatt, "Single-pass volumetric bidirectional blood flow imaging spectral domain optical coherence tomography using a modified Hilbert transform," *Opt Express*, vol. 16, pp. 12350-61, Aug 4 2008.
- [10] L. An and R. K. Wang, "In vivo volumetric imaging of vascular perfusion within human retina and choroids with optical micro-angiography," *Opt Express*, vol. 16, pp. 11438-52, Jul 21 2008.
- [11] A. Mariampillai, B. A. Standish, E. H. Moriyama, M. Khurana, N. R. Munce, M. K. Leung, J. Jiang, A. Cable, B. C. Wilson, I. A. Vitkin, and V. X. Yang, "Speckle variance detection of microvasculature using swept-source optical coherence tomography," *Opt Lett*, vol. 33, pp. 1530-2, Jul 1 2008.
- [12] B. J. Vakoc, R. M. Lanning, J. A. Tyrrell, T. P. Padera, L. A. Bartlett, T. Stylianopoulos, L. L. Munn, G. J. Tearney, D. Fukumura, R. K. Jain, and B. E. Bouma, "Three-dimensional microscopy of the tumor microenvironment in vivo using optical frequency domain imaging," *Nat Med*, vol. 15, pp. 1219-23, Oct 2009.
- [13] L. Yu and Z. Chen, "Doppler variance imaging for three-dimensional retina and choroid angiography," *J Biomed Opt*, vol. 15, p. 016029, Jan-Feb 2010.
- [14] C. Blatter, T. Klein, B. Grajciar, T. Schmoll, W. Wieser, R. Andre, R. Huber, and R. A. Leitgeb, "Ultrahigh-speed non-invasive widefield angiography," *J Biomed Opt*, vol. 17, p. 070505, Jul 2012.
- [15] B. Braaf, K. V. Vienola, C. K. Sheehy, Q. Yang, K. A. Vermeer, P. Tiruveedhula, D. W. Arathorn, A. Roorda, and J. F. de Boer, "Real-time eye motion correction in phase-resolved OCT angiography with tracking SLO," *Biomedical optics express*, vol. 4, pp. 51-65, Jan 1 2013.
- [16] D. M. Schwartz, J. Fingler, D. Y. Kim, R. J. Zawadzki, L. S. Morse, S. S. Park, S. E. Fraser, and J. S. Werner, "Phase-variance optical coherence tomography: a technique for noninvasive angiography," *Ophthalmology*, vol. 121, pp. 180-7, Jan 2014.
- [17] D. S. McLeod and G. A. Luttly, "High-resolution histologic analysis of the human choroidal vasculature," *Invest Ophthalmol Vis Sci*, vol. 35, pp. 3799-811, Oct 1994.

- [18] V. J. Srinivasan, S. Sakadzic, I. Gorczynska, S. Ruvinskaya, W. Wu, J. G. Fujimoto, and D. A. Boas, "Quantitative cerebral blood flow with optical coherence tomography," *Opt Express*, vol. 18, pp. 2477-94, Feb 1 2010.
- [19] J. F. De Boer and T. E. Milner, "Review of polarization sensitive optical coherence tomography and Stokes vector determination," *Journal of Biomedical Optics*, vol. 7, pp. 359-371, 2002.
- [20] M. Pircher, C. K. Hitzenberger, and U. Schmidt-Erfurth, "Polarization sensitive optical coherence tomography in the human eye," *Progress in retinal and eye research*, vol. 30, pp. 431-451, 2011.
- [21] M. C. Pierce, R. L. Sheridan, B. Hyle Park, B. Cense, and J. F. de Boer, "Collagen denaturation can be quantified in burned human skin using polarization-sensitive optical coherence tomography," *Burns*, vol. 30, pp. 511-517, 2004.
- [22] S. K. Nadkarni, M. C. Pierce, B. H. Park, J. F. de Boer, P. Whittaker, B. E. Bouma, J. E. Bressner, E. Halpern, S. L. Houser, and G. J. Tearney, "Measurement of Collagen and Smooth Muscle Cell Content in Atherosclerotic Plaques Using Polarization-Sensitive Optical Coherence Tomography," *Journal of the American College of Cardiology*, vol. 49, pp. 1474-1481, 2007.
- [23] M. R. Hee, D. Huang, E. A. Swanson, and J. G. Fujimoto, "Polarization-sensitive low-coherence reflectometer for birefringence characterization and ranging," *Journal of the Optical Society of America B*, vol. 9, 1992.
- [24] M. K. Al-Qaisi and T. Akkin, "Polarization-sensitive optical coherence tomography based on polarization-maintaining fibers and frequency multiplexing," *Opt. Express*, vol. 16, pp. 13032-13041, 2008.
- [25] C. Hitzenberger, E. Goetzinger, M. Sticker, M. Pircher, and A. Fercher, "Measurement and imaging of birefringence and optic axis orientation by phase resolved polarization sensitive optical coherence tomography," *Optics Express*, vol. 9, pp. 780-790, 2001/12/17 2001.
- [26] B. H. Park, M. C. Pierce, B. Cense, and J. F. de Boer, "Jones matrix analysis for a polarization-sensitive optical coherence tomography system using fiber-optic components," *Opt. Lett.*, vol. 29, pp. 2512-2514, 2004.
- [27] W. Y. Oh, S. H. Yun, B. J. Vakoc, M. Shishkov, A. E. Desjardins, B. H. Park, J. F. de Boer, G. J. Tearney, and B. E. Bouma, "High-speed polarization sensitive optical frequency domain imaging with frequency multiplexing," *Opt. Express*, vol. 16, pp. 1096-1103, 2008.
- [28] M. Yamanari, S. Makita, and Y. Yasuno, "Polarization-sensitive swept-source optical coherence tomography with continuous source polarization modulation," *Opt. Express*, vol. 16, pp. 5892-5906, 2008.
- [29] B. Baumann, W. Choi, B. Potsaid, D. Huang, J. S. Duker, and J. G. Fujimoto, "Swept source Fourier domain polarization sensitive optical coherence tomography with a passive polarization delay unit," *Opt. Express*, vol. 20, pp. 10229-10241, 2012.
- [30] G. J. Tearney, M. E. Brezinski, B. E. Bouma, S. A. Boppart, C. Pitris, J. F. Southern, and J. G. Fujimoto, "In Vivo Endoscopic Optical Biopsy with Optical Coherence Tomography," *Science*, vol. 276, pp. 2037-2039, June 27, 1997 1997.
- [31] V. Jayaraman, G. Cole, M. Robertson, A. Uddin, and A. Cable, "High-sweep-rate 1310 nm MEMS-VCSEL with 150 nm continuous tuning range," *Electronics Letters*, vol. 48, pp. 867-869, 2012.
- [32] C. E. Saxer, J. F. de Boer, B. H. Park, Y. Zhao, Z. Chen, and J. S. Nelson, "High-speed fiber based polarization-sensitive optical coherence tomography of in vivo human skin," *Optics letters*, vol. 25, pp. 1355-1357, 2000/09/15 2000.
- [33] B. Park, M. C. Pierce, B. Cense, S.-H. Yun, M. Mujat, G. Tearney, B. Bouma, and J. de Boer, "Real-time fiber-based multi-functional spectral-domain optical coherence tomography at 1.3 μm ," *Opt. Express*, vol. 13, pp. 3931-3944, 2005.
- [34] E. Götzinger, M. Pircher, B. Baumann, T. Schmoll, H. Sattmann, R. A. Leitgeb, and C. K. Hitzenberger, "Speckle noise reduction in high speed polarization sensitive spectral domain optical coherence tomography," *Optics Express*, vol. 19, pp. 14568-14585, 2011/07/18 2011.
- [35] Y. Lim, M. Yamanari, S. Fukuda, Y. Kaji, T. Kiuchi, M. Miura, T. Oshika, and Y. Yasuno, "Birefringence measurement of cornea and anterior segment by office-based polarization-sensitive optical coherence tomography," *Biomedical Optics Express*, vol. 2, pp. 2392-2402, 2011/08/01 2011.
- [36] M. J. Ju, Y.-J. Hong, S. Makita, Y. Lim, K. Kurokawa, L. Duan, M. Miura, S. Tang, and Y. Yasuno, "Advanced multi-contrast Jones matrix optical coherence tomography for Doppler and polarization sensitive imaging," *Opt. Express*, vol. 21, pp. 19412-19436, 2013.
- [37] M. F. Kraus, B. Potsaid, M. A. Mayer, R. Bock, B. Baumann, J. J. Liu, J. Hornegger, and J. G. Fujimoto, "Motion correction in optical coherence tomography volumes on a per A-scan basis using orthogonal scan patterns," *Biomed Opt Express*, vol. 3, pp. 1182-99, Jun 1 2012.

- [38] "Cancer Facts and Figures," American Cancer Society 2013.
- [39] X. Chen and C. S. Yang, "Esophageal adenocarcinoma: a review and perspectives on the mechanism of carcinogenesis and chemoprevention," *Carcinogenesis*, vol. 22, pp. 1119-29, Aug 2001.
- [40] R. D. Odze and G. Y. Lauwers, "Histopathology of Barrett's esophagus after ablation and endoscopic mucosal resection therapy," *Endoscopy*, vol. 40, pp. 1008-1015, Dec 2008.
- [41] J. J. G. H. M. Bergman, "Radiofrequency Ablation - Great for Some or Justified for Many?," *New England Journal of Medicine*, vol. 360, pp. 2353-2355, May 28 2009.
- [42] C. Ell, O. Pech, and A. May, "Radiofrequency Ablation in Barrett's Esophagus," *New England Journal of Medicine*, vol. 361, pp. 1021-1021, Sep 3 2009.
- [43] N. J. Shaheen, P. Sharma, B. F. Overholt, H. C. Wolfsen, R. E. Sampliner, K. K. Wang, J. A. Galanko, M. P. Bronner, J. R. Goldblum, A. E. Bennett, B. A. Jobe, G. M. Eisen, M. B. Fennerty, J. G. Hunter, D. E. Fleischer, V. K. Sharma, R. H. Hawes, B. J. Hoffman, R. I. Rothstein, S. R. Gordon, H. Mashimo, K. J. Chang, V. R. Muthusamy, S. A. Edmundowicz, S. J. Spechler, A. A. Siddiqui, R. F. Souza, A. Infantolino, G. W. Falk, M. B. Kimmey, R. D. Madanick, A. Chak, and C. J. Lightdale, "Radiofrequency Ablation in Barrett's Esophagus with Dysplasia," *New England Journal of Medicine*, vol. 360, pp. 2277-2288, May 28 2009.
- [44] R. Pouw, J. Gondrie, C. Sondermeijer, F. ten Kate, T. van Gulik, K. Krishnadath, P. Fockens, B. Weusten, and J. Bergman, "Eradication of Barrett Esophagus with Early Neoplasia by Radiofrequency Ablation, with or without Endoscopic Resection," *Journal of Gastrointestinal Surgery*, vol. 12, pp. 1627-1637, 2008.
- [45] B. Dunkin, J. Martinez, P. Bejarano, C. Smith, K. Chang, A. Livingstone, and W. Melvin, "Thin-layer ablation of human esophageal epithelium using a bipolar radiofrequency balloon device," *Surgical Endoscopy*, vol. 20, pp. 125-130, 2006.
- [46] V. K. Sharma, K. K. Wang, B. F. Overholt, C. J. Lightdale, M. B. Fennerty, P. J. Dean, D. K. Pleskow, R. Chuttani, A. Reymunde, N. Santiago, K. J. Chang, M. B. Kimmey, and D. E. Fleischer, "Balloon-based, circumferential, endoscopic radiofrequency ablation of Barrett's esophagus: 1-year follow-up of 100 patients (with video)," *Gastrointestinal Endoscopy*, vol. 65, pp. 185-195, 2007.
- [47] H. Barr, N. Krasner, P. B. Boulos, P. Chatlani, and S. G. Bown, "PHOTODYNAMIC THERAPY FOR COLORECTAL-CANCER - A QUANTITATIVE PILOT-STUDY," *British Journal of Surgery*, vol. 77, pp. 93-96, Jan 1990.
- [48] M. H. Johnston, "Cryotherapy and other newer techniques," *Gastrointest Endosc Clin N Am*, vol. 13, pp. 491-504, 2003 2003.
- [49] H. Barr, N. Stone, and B. Rembacken, "Endoscopic therapy for Barrett's oesophagus," *Gut*, vol. 54, pp. 875-884, Jun 2005.
- [50] T. H. Tsai, C. Zhou, Y. K. Tao, H. C. Lee, O. O. Ahsen, M. Figueiredo, T. Kirtane, D. C. Adler, J. M. Schmitt, Q. Huang, J. G. Fujimoto, and H. Mashimo, "Structural markers observed with endoscopic 3-dimensional optical coherence tomography correlating with Barrett's esophagus radiofrequency ablation treatment response (with videos)," *Gastrointest Endosc*, Jul 24 2012.
- [51] I. Grulkowski, J. J. Liu, J. Y. Zhang, B. Potsaid, V. Jayaraman, A. E. Cable, J. S. Duker, and J. G. Fujimoto, "Reproducibility of a long-range swept-source optical coherence tomography ocular biometry system and comparison with clinical biometers," *Ophthalmology*, vol. 120, pp. 2184-90, Nov 2013.
- [52] M. F. Kraus, J. J. Liu, J. Schottenhamml, C. L. Chen, A. Budai, L. Branchini, T. Ko, H. Ishikawa, G. Wollstein, J. Schuman, J. S. Duker, J. G. Fujimoto, and J. Hornegger, "Quantitative 3D-OCT motion correction with tilt and illumination correction, robust similarity measure and regularization," *Biomed Opt Express*, vol. 5, pp. 2591-613, Aug 1 2014.
- [53] D. Huang, E. A. Swanson, C. P. Lin, J. S. Schuman, W. G. Stinson, W. Chang, M. R. Hee, T. Flotte, K. Gregory, C. A. Puliafito, and et al., "Optical coherence tomography," *Science*, vol. 254, pp. 1178-81, Nov 22 1991.
- [54] B. Potsaid, B. Baumann, D. Huang, S. Barry, A. E. Cable, J. S. Schuman, J. S. Duker, and J. G. Fujimoto, "Ultrahigh speed 1050nm swept source/Fourier domain OCT retinal and anterior segment imaging at 100,000 to 400,000 axial scans per second," *Opt Express*, vol. 18, pp. 20029-48, Sep 13 2010.
- [55] Z. Nadler, B. Wang, G. Wollstein, J. E. Nevins, H. Ishikawa, L. Kagemann, I. A. Sigal, R. D. Ferguson, D. X. Hammer, I. Grulkowski, J. J. Liu, M. F. Kraus, C. D. Lu, J. Hornegger, J. G. Fujimoto, and J. S. Schuman, "Automated lamina cribrosa microstructural segmentation in optical coherence tomography scans of healthy and glaucomatous eyes," *Biomed Opt Express*, vol. 4, pp. 2596-608, 2013.
- [56] B. Wang, J. E. Nevins, Z. Nadler, G. Wollstein, H. Ishikawa, R. A. Bilonick, L. Kagemann, I. A. Sigal, I. Grulkowski, J. J. Liu, M. Kraus, C. D. Lu, J. Hornegger, J. G. Fujimoto, and J. S. Schuman, "In vivo

- lamina cribrosa micro-architecture in healthy and glaucomatous eyes as assessed by optical coherence tomography," *Invest Ophthalmol Vis Sci*, vol. 54, pp. 8270-4, Dec 2013.
- [57] B. E. Robinson, "Prevalence of Asymptomatic Eye Disease Prévalence des maladies oculaires asymptomatiques," *Revue Canadienne D'Optométrie*, vol. 65, p. 175, 2003.
- [58] H. A. Quigley, "Number of people with glaucoma worldwide," *Br J Ophthalmol*, vol. 80, pp. 389-93, May 1996.
- [59] F. Wang, D. Ford, J. M. Tielsch, H. A. Quigley, and P. K. Whelton, "Undetected eye disease in a primary care clinic population," *Archives of Internal Medicine*, vol. 154, pp. 1821-8, Aug 22 1994.
- [60] R. Varma, S. A. Mohanty, J. Deneen, J. Wu, and S. P. Azen, "Burden and predictors of undetected eye disease in Mexican-Americans: the Los Angeles Latino Eye Study," *Med Care*, vol. 46, pp. 497-506, May 2008.
- [61] E. Y. Wong, J. E. Keeffe, J. L. Rait, H. T. Vu, A. Le, D. C. McCarty Ph, and H. R. Taylor, "Detection of undiagnosed glaucoma by eye health professionals," *Ophthalmology*, vol. 111, pp. 1508-14, Aug 2004.
- [62] S. Garg and R. M. Davis, "Diabetic retinopathy screening update," *Clinical diabetes*, vol. 27, pp. 140-145, 2009.
- [63] S. Radhakrishnan, A. M. Rollins, J. E. Roth, S. Yazdanfar, V. Westphal, D. S. Bardenstein, and J. A. Izatt, "Real-time optical coherence tomography of the anterior segment at 1310 nm," *Archives of Ophthalmology*, vol. 119, pp. 1179-85, Aug 2001.
- [64] W. Jung, J. Kim, M. Jeon, E. J. Chaney, C. N. Stewart, and S. A. Boppart, "Handheld Optical Coherence Tomography Scanner for Primary Care Diagnostics," *Ieee Transactions on Biomedical Engineering*, vol. 58, pp. 741-744, Mar 2011.
- [65] F. Larocca, D. Nankivil, S. Farsiu, and J. A. Izatt, "Handheld simultaneous scanning laser ophthalmoscopy and optical coherence tomography system," *Biomedical optics express*, vol. 4, pp. 2307-21, 2013.
- [66] R. L. Shelton, W. Jung, S. I. Sayegh, D. T. McCormick, J. Kim, and S. A. Boppart, "Optical coherence tomography for advanced screening in the primary care office," *Journal of Biophotonics*, Apr 18 2013.
- [67] C. D. Lu, M. F. Kraus, B. Potsaid, J. J. Liu, W. Choi, V. Jayaraman, A. E. Cable, J. Hornegger, J. S. Duker, and J. G. Fujimoto, "Handheld ultrahigh speed swept source optical coherence tomography instrument using a MEMS scanning mirror," *Biomedical optics express*, vol. 5, pp. 293-311, Jan 1 2014.
- [68] M. Tang, Y. Li, M. Avila, and D. Huang, "Measuring total corneal power before and after laser in situ keratomileusis with high-speed optical coherence tomography," *J Cataract Refract Surg*, vol. 32, pp. 1843-50, Nov 2006.
- [69] T. Swartz, L. Marten, and M. Wang, "Measuring the cornea: the latest developments in corneal topography," *Curr Opin Ophthalmol*, vol. 18, pp. 325-33, Jul 2007.
- [70] M. Doors, T. T. Berendschot, J. de Brabander, C. A. Webers, and R. M. Nuijts, "Value of optical coherence tomography for anterior segment surgery," *J Cataract Refract Surg*, vol. 36, pp. 1213-29, Jul 2010.
- [71] M. Tang, A. Chen, Y. Li, and D. Huang, "Corneal power measurement with Fourier-domain optical coherence tomography," *J Cataract Refract Surg*, vol. 36, pp. 2115-22, Dec 2010.
- [72] I. Grulkowski, J. J. Liu, B. Potsaid, V. Jayaraman, J. Jiang, J. G. Fujimoto, and A. E. Cable, "High-precision, high-accuracy ultralong-range swept-source optical coherence tomography using vertical cavity surface emitting laser light source," *Opt Lett*, vol. 38, pp. 673-5, Mar 1 2013.
- [73] P. M. Bischoff and R. W. Flower, "Ten years experience with choroidal angiography using indocyanine green dye: a new routine examination or an epilogue?," *Doc Ophthalmol*, vol. 60, pp. 235-91, Sep 30 1985.
- [74] R. W. Flower, "Extraction of choriocapillaris hemodynamic data from ICG fluorescence angiograms," *Invest Ophthalmol Vis Sci*, vol. 34, pp. 2720-9, Aug 1993.
- [75] L. Zhu, Y. Zheng, C. H. von Kerczek, L. D. T. Topoleski, and R. W. Flower, "Feasibility of extracting velocity distribution in choriocapillaris in human eyes from ICG dye angiograms," *Journal of Biomechanical Engineering-Transactions of the Asme*, vol. 128, pp. 203-209, Apr 2006.
- [76] E. Jonathan, J. Enfield, and M. J. Leahy, "Correlation mapping: rapid method for retrieving microcirculation morphology from optical coherence tomography intensity images," *Dynamics and Fluctuations in Biomedical Photonics Viii*, vol. 7898, 2011.
- [77] Y. Jia, O. Tan, J. Tokayer, B. Potsaid, Y. Wang, J. J. Liu, M. F. Kraus, H. Subhash, J. G. Fujimoto, J. Hornegger, and D. Huang, "Split-spectrum amplitude-decorrelation angiography with optical coherence tomography," *Opt Express*, vol. 20, pp. 4710-25, Feb 13 2012.
- [78] W. Choi, K. J. Mohler, B. Potsaid, C. D. Lu, J. J. Liu, V. Jayaraman, A. E. Cable, J. S. Duker, R. Huber, and J. G. Fujimoto, "Choriocapillaris and choroidal microvasculature imaging with ultrahigh speed OCT angiography," *PLoS One*, vol. 8, p. e81499, 2013.

- [79] J. M. Olver, "Functional anatomy of the choroidal circulation: methyl methacrylate casting of human choroid," *Eye (Lond)*, vol. 4 (Pt 2), pp. 262-72, 1990.
- [80] S. S. Hayreh, "Blood supply of the optic nerve head and its role in optic atrophy, glaucoma, and oedema of the optic disc," *Br J Ophthalmol*, vol. 53, pp. 721-48, Nov 1969.
- [81] J. Flammer, "The vascular concept of glaucoma," *Surv Ophthalmol*, vol. 38 Suppl, pp. S3-6, May 1994.
- [82] J. Flammer, S. Orgul, V. P. Costa, N. Orzalesi, G. K. Kriegelstein, L. M. Serra, J. P. Renard, and E. Stefansson, "The impact of ocular blood flow in glaucoma," *Prog Retin Eye Res*, vol. 21, pp. 359-93, Jul 2002.
- [83] M. C. Grieshaber and J. Flammer, "Blood flow in glaucoma," *Curr Opin Ophthalmol*, vol. 16, pp. 79-83, Apr 2005.
- [84] L. Schmetterer and M. Wolzt, "Ocular blood flow and associated functional deviations in diabetic retinopathy," *Diabetologia*, vol. 42, pp. 387-405, Apr 1999.
- [85] R. Klein, B. E. Klein, S. E. Moss, T. Y. Wong, L. Hubbard, K. J. Cruickshanks, and M. Palta, "Retinal vascular abnormalities in persons with type 1 diabetes: the Wisconsin Epidemiologic Study of Diabetic Retinopathy: XVIII," *Ophthalmology*, vol. 110, pp. 2118-25, Nov 2003.
- [86] A. Yoshida, G. T. Feke, J. Morales-Stoppello, G. D. Collas, D. G. Goger, and J. W. McMeel, "Retinal blood flow alterations during progression of diabetic retinopathy," *Arch Ophthalmol*, vol. 101, pp. 225-7, Feb 1983.
- [87] V. Patel, S. Rassam, R. Newsom, J. Wiek, and E. Kohner, "Retinal blood flow in diabetic retinopathy," *BMJ*, vol. 305, pp. 678-83, Sep 19 1992.
- [88] A. S. Hafez, R. L. Bizzarro, and M. R. Lesk, "Evaluation of optic nerve head and peripapillary retinal blood flow in glaucoma patients, ocular hypertensives, and normal subjects," *Am J Ophthalmol*, vol. 136, pp. 1022-31, Dec 2003.
- [89] G. Fuchsjager-Mayrl, B. Wally, M. Georgopoulos, G. Rainer, K. Kircher, W. Buehl, T. Amoako-Mensah, H. G. Eichler, C. Vass, and L. Schmetterer, "Ocular blood flow and systemic blood pressure in patients with primary open-angle glaucoma and ocular hypertension," *Invest Ophthalmol Vis Sci*, vol. 45, pp. 834-9, Mar 2004.
- [90] A. Harris, R. C. Sergott, G. L. Spaeth, J. L. Katz, J. A. Shoemaker, and B. J. Martin, "Color Doppler analysis of ocular vessel blood velocity in normal-tension glaucoma," *Am J Ophthalmol*, vol. 118, pp. 642-9, Nov 15 1994.
- [91] S. J. Rankin, B. E. Walman, A. R. Buckley, and S. M. Drance, "Color Doppler imaging and spectral analysis of the optic nerve vasculature in glaucoma," *Am J Ophthalmol*, vol. 119, pp. 685-93, Jun 1995.
- [92] G. T. Feke, S. M. Buzney, H. Ogasawara, N. Fujio, D. G. Goger, N. P. Spack, and K. H. Gabbay, "Retinal circulatory abnormalities in type 1 diabetes," *Invest Ophthalmol Vis Sci*, vol. 35, pp. 2968-75, Jun 1994.
- [93] B. Bertram, S. Wolf, S. Fiehofer, K. Schulte, O. Arend, and M. Reim, "Retinal circulation times in diabetes mellitus type 1," *Br J Ophthalmol*, vol. 75, pp. 462-5, Aug 1991.
- [94] S. E. Bursell, A. C. Clermont, B. T. Kinsley, D. C. Simonson, L. M. Aiello, and H. A. Wolpert, "Retinal blood flow changes in patients with insulin-dependent diabetes mellitus and no diabetic retinopathy," *Invest Ophthalmol Vis Sci*, vol. 37, pp. 886-97, Apr 1996.
- [95] C. E. Riva, J. E. Grunwald, S. H. Sinclair, and B. L. Petrig, "Blood velocity and volumetric flow rate in human retinal vessels," *Invest Ophthalmol Vis Sci*, vol. 26, pp. 1124-32, Aug 1985.
- [96] G. T. Feke, H. Tagawa, D. M. Deupree, D. G. Goger, J. Sebag, and J. J. Weiter, "Blood flow in the normal human retina," *Invest Ophthalmol Vis Sci*, vol. 30, pp. 58-65, Jan 1989.
- [97] J. P. Garcia, Jr., P. T. Garcia, and R. B. Rosen, "Retinal blood flow in the normal human eye using the canon laser blood flowmeter," *Ophthalmic Research*, vol. 34, pp. 295-9, Sep-Oct 2002.
- [98] K. Guan, C. Hudson, and J. G. Flanagan, "Variability and repeatability of retinal blood flow measurements using the Canon Laser Blood Flowmeter," *Microvasc Res*, vol. 65, pp. 145-51, May 2003.
- [99] J. E. Grunwald, C. E. Riva, J. Baine, and A. J. Brucker, "Total retinal volumetric blood flow rate in diabetic patients with poor glycemic control," *Invest Ophthalmol Vis Sci*, vol. 33, pp. 356-63, Feb 1992.
- [100] G. T. Feke, H. Tagawa, A. Yoshida, D. G. Goger, J. J. Weiter, S. M. Buzney, and J. W. McMeel, "Retinal circulatory changes related to retinopathy progression in insulin-dependent diabetes mellitus," *Ophthalmology*, vol. 92, pp. 1517-22, Nov 1985.
- [101] J. E. Grunwald, J. DuPont, and C. E. Riva, "Retinal haemodynamics in patients with early diabetes mellitus," *Br J Ophthalmol*, vol. 80, pp. 327-31, Apr 1996.

- [102] B. Pemp, E. Polska, G. Garhofer, M. Bayerle-Eder, A. Kautzky-Willer, and L. Schmetterer, "Retinal blood flow in type 1 diabetic patients with no or mild diabetic retinopathy during euglycemic clamp," *Diabetes Care*, vol. 33, pp. 2038-42, Sep 2010.
- [103] G. Garhofer, R. Werkmeister, N. Dragostinoff, and L. Schmetterer, "Retinal blood flow in healthy young subjects," *Invest Ophthalmol Vis Sci*, vol. 53, pp. 698-703, Feb 2012.
- [104] R. A. Leitgeb, L. Schmetterer, W. Drexler, A. F. Fercher, R. J. Zawadzki, and T. Bajraszewski, "Real-time assessment of retinal blood flow with ultrafast acquisition by color Doppler Fourier domain optical coherence tomography," *Optics Express*, vol. 11, pp. 3116-3121, Nov 17 2003.
- [105] Y. M. Wang, B. A. Bower, J. A. Izatt, O. Tan, and D. Huang, "In vivo total retinal blood flow measurement by Fourier domain Doppler optical coherence tomography," *Journal of Biomedical Optics*, vol. 12, Jul-Aug 2007.
- [106] Y. Wang, B. A. Bower, J. A. Izatt, O. Tan, and D. Huang, "Retinal blood flow measurement by circumpapillary Fourier domain Doppler optical coherence tomography," *J Biomed Opt*, vol. 13, p. 064003, Nov-Dec 2008.
- [107] B. Baumann, B. Potsaid, M. F. Kraus, J. J. Liu, D. Huang, J. Hornegger, A. E. Cable, J. S. Duker, and J. G. Fujimoto, "Total retinal blood flow measurement with ultrahigh speed swept source/Fourier domain OCT," *Biomed Opt Express*, vol. 2, pp. 1539-52, Jun 1 2011.
- [108] W. Choi, B. Baumann, J. J. Liu, A. C. Clermont, E. P. Feener, J. S. Duker, and J. G. Fujimoto, "Measurement of pulsatile total blood flow in the human and rat retina with ultrahigh speed spectral/Fourier domain OCT," *Biomed Opt Express*, vol. 3, pp. 1047-61, May 1 2012.
- [109] A. Grinvald, E. Lieke, R. D. Frostig, C. D. Gilbert, and T. N. Wiesel, "Functional architecture of cortex revealed by optical imaging of intrinsic signals," *Nature*, vol. 324, pp. 361-364, 1986.
- [110] U. Dirnagl, B. Kaplan, M. Jacewicz, and W. Pulsinelli, "Continuous measurement of cerebral cortical blood flow by laser-Doppler flowmetry in a rat stroke model," *J. Cereb. Blood Flow Metab.*, vol. 9, pp. 589-596, 1989.
- [111] A. K. Dunn, H. Bolay, M. A. Moskowitz, and D. A. Boas, "Dynamic Imaging of Cerebral Blood Flow Using Laser Speckle," *J. Cereb. Blood Flow Metab.*, vol. 21, pp. 195-201, 2001.
- [112] A. Villringer and B. Chance, "Non-invasive optical spectroscopy and imaging of human brain function," *Trends in Neurosciences*, vol. 20, pp. 435-442, 1997.
- [113] E. Hillman, D. A. Boas, A. M. Dale, and A. K. Dunn, "Laminar optical tomography: demonstration of millimeter-scale depth-resolved imaging in turbid media," *Optics Letters*, vol. 29, pp. 1650-1652, 2004.
- [114] W. Denk, J. Strickler, and W. Webb, "Two-photon laser scanning fluorescence microscopy," *Science*, vol. 248, pp. 73-76, April 6, 1990 1990.
- [115] V. J. Srinivasan, J. Y. Jiang, M. A. Yaseen, H. Radhakrishnan, W. Wu, S. Barry, A. E. Cable, and D. A. Boas, "Rapid volumetric angiography of cortical microvasculature with optical coherence tomography," *Opt. Lett.*, vol. 35, pp. 43-5, Jan 1 2010.
- [116] V. J. Srinivasan, E. T. Mandeville, A. Can, F. Blasi, M. Climov, A. Daneshmand, J. H. Lee, E. Yu, H. Radhakrishnan, and E. H. Lo, "Multiparametric, Longitudinal Optical Coherence Tomography Imaging Reveals Acute Injury and Chronic Recovery in Experimental Ischemic Stroke," *PloS one*, vol. 8, p. e71478, 2013.
- [117] J. Lee, W. Wu, J. Y. Jiang, B. Zhu, and D. A. Boas, "Dynamic light scattering optical coherence tomography," *Opt. Express*, vol. 20, pp. 22262-22277, 2012.
- [118] J. Lee, H. Radhakrishnan, W. Wu, A. Daneshmand, M. Climov, C. Ayata, and D. A. Boas, "Quantitative imaging of cerebral blood flow velocity and intracellular motility using dynamic light scattering-optical coherence tomography," *J Cereb Blood Flow Metab*, vol. 33, pp. 819-825, 2013.
- [119] J. Lee, W. Wu, F. Lesage, and D. A. Boas, "Multiple-capillary measurement of RBC speed, flux, and density with optical coherence tomography," *J Cereb Blood Flow Metab*, vol. 33, pp. 1707-1710, 2013.
- [120] O. J. Arthurs and S. Boniface, "How well do we understand the neural origins of the fMRI BOLD signal?," *Trends in Neurosciences*, vol. 25, pp. 27-31, 2002.
- [121] L. SOKOLOFF, "Measurement of local cerebral blood flow with iodo [¹⁴C] antipyrine," 1978.
- [122] F. Calamante, D. L. Thomas, G. S. Pell, J. Wiersma, and R. Turner, "Measuring cerebral blood flow using magnetic resonance imaging techniques," *Journal of Cerebral Blood Flow & Metabolism*, vol. 19, pp. 701-735, 1999.
- [123] W.-D. Heiss and K. Herholz, "Assessment of pathophysiology of stroke by positron emission tomography," *European journal of nuclear medicine*, vol. 21, pp. 455-465, 1994.

- [124] D. Kleinfeld, P. P. Mitra, F. Helmchen, and W. Denk, "Fluctuations and stimulus-induced changes in blood flow observed in individual capillaries in layers 2 through 4 of rat neocortex," *Proc. Natl. Acad. Sci.*, vol. 95, pp. 15741-15746, 1998.
- [125] M. Lauritzen and M. Fabricius, "Real time laser-Doppler perfusion imaging of cortical spreading depression in rat neocortex," *Neuroreport*, vol. 6, p. 1271&hyphen, 1995.
- [126] A. Fercher and J. Briers, "Flow visualization by means of single-exposure speckle photography," *Optics Communications*, vol. 37, pp. 326-330, 1981.
- [127] R. Bonner and R. Nossal, "Model for laser Doppler measurements of blood flow in tissue," *Appl. Opt.*, vol. 20, pp. 2097-2107, 1981.
- [128] B. R. White, M. C. Pierce, N. Nassif, B. Cense, B. H. Park, G. J. Tearney, B. E. Bouma, T. C. Chen, and J. F. de Boer, "In vivo dynamic human retinal blood flow imaging using ultra-high-speed spectral domain optical Doppler tomography," *Optics Express*, vol. 11, pp. 3490-3497, Dec 15 2003.
- [129] Z. Chen, T. E. Milner, D. Dave, and J. S. Nelson, "Optical Doppler tomographic imaging of fluid flow velocity in highly scattering media," *Optics Letters*, vol. 22, pp. 64-66, 1997.
- [130] J. A. Izatt, M. D. Kulkarni, S. Yazdanfar, J. K. Barton, and A. J. Welch, "In vivo bidirectional color Doppler flow imaging of picoliter blood volumes using optical coherence tomography," *Opt. Lett.*, vol. 22, pp. 1439-1441, 1997.
- [131] J. A. Izatt, M. R. Hee, G. M. Owen, E. A. Swanson, and J. G. Fujimoto, "Optical coherence microscopy in scattering media," *Optics Letters*, vol. 19, pp. 590-2, Apr 15 1994.
- [132] D. Atochin, I. Demchenko, J. Atern, A. Boso, C. Piantadosi, and P. Huang, "Contributions of endothelial and neuronal nitric oxide synthases to cerebrovascular responses to hyperoxia," *Journal of Cerebral Blood Flow & Metabolism*, vol. 23, pp. 1219-1226, 2003.
- [133] Y. Zhao, Z. Chen, C. Saxer, S. Xiang, J. F. de Boer, and J. S. Nelson, "Phase-resolved optical coherence tomography and optical Doppler tomography for imaging blood flow in human skin with fast scanning speed and high velocity sensitivity," *Opt. Lett.*, vol. 25, pp. 114-116, 2000.
- [134] R. K. Wang and L. An, "Doppler optical micro-angiography for volumetric imaging of vascular perfusion in vivo," *Optics Express*, vol. 17, pp. 8926-8940, 2009/05/25 2009.
- [135] H.-C. Lee, C. Zhou, D. W. Cohen, A. E. Mondelblatt, Y. Wang, A. D. Aguirre, D. Shen, Y. Sheikine, J. G. Fujimoto, and J. L. Connolly, "Integrated Optical Coherence Tomography and Optical Coherence Microscopy Imaging of Ex Vivo Human Renal Tissues," *Journal of Urology*, vol. 187, pp. 691-699, Feb 2012.
- [136] N. Weiss, T. G. van Leeuwen, and J. Kalkman, "Localized measurement of longitudinal and transverse flow velocities in colloidal suspensions using optical coherence tomography," *Physical Review E*, vol. 88, p. 042312, 2013.
- [137] V. J. Srinivasan, H. Radhakrishnan, E. H. Lo, E. T. Mandeville, J. Y. Jiang, S. Barry, and A. E. Cable, "OCT methods for capillary velocimetry," *Biomed. Opt. Express*, vol. 3, pp. 612-629, 2012.
- [138] A. Bouwens, D. Szlag, M. Szkulmowski, T. Bolmont, M. Wojtkowski, and T. Lasser, "Quantitative lateral and axial flow imaging with optical coherence microscopy and tomography," *Optics Express*, vol. 21, pp. 17711-17729, 2013/07/29 2013.
- [139] Y. Wang and R. Wang, "Autocorrelation optical coherence tomography for mapping transverse particle-flow velocity," *Opt. Lett.*, vol. 35, pp. 3538-3540, 2010.
- [140] X. Liu, Y. Huang, J. C. Ramella-Roman, S. A. Mathews, and J. U. Kang, "Quantitative transverse flow measurement using optical coherence tomography speckle decorrelation analysis," *Optics Letters*, vol. 38, pp. 805-807, 2013/03/01 2013.
- [141] M. Tomita, Y. Tomita, M. Unekawa, H. Toriumi, and N. Suzuki, "Oscillating neuro-capillary coupling during cortical spreading depression as observed by tracking of FITC-labeled RBCs in single capillaries," *Neuroimage*, vol. 56, pp. 1001-1010, 2011.
- [142] B. Stefanovic, E. Hutchinson, V. Yakovleva, V. Schram, J. T. Russell, L. Belluscio, A. P. Koretsky, and A. C. Silva, "Functional reactivity of cerebral capillaries," *J Cereb Blood Flow Metab*, vol. 28, pp. 961-972, 2007.
- [143] M. L. Schulte, J. D. Wood, and A. G. Hudetz, "Cortical electrical stimulation alters erythrocyte perfusion pattern in the cerebral capillary network of the rat," *Brain Research*, vol. 963, pp. 81-92, 2003.
- [144] J. Lee, J. Y. Jiang, W. Wu, F. Lesage, and D. A. Boas, "Statistical intensity variation analysis for rapid volumetric imaging of capillary network flux," *Biomedical Optics Express*, vol. 5, pp. 1160-1172, 2014/04/01 2014.

- [145] P. R. Allison and A. S. Johnstone, "The Oesophagus Lined with Gastric Mucous Membrane," *Thorax*, vol. 8, pp. 87-101, 1953.
- [146] B. J. Reid, X. H. Li, P. C. Galipeau, and T. L. Vaughan, "Barrett's oesophagus and oesophageal adenocarcinoma: time for a new synthesis," *Nature Reviews Cancer*, vol. 10, pp. 87-101, Feb 2010.
- [147] T. J. Hayeck, C. Y. Kong, S. J. Spechler, G. S. Gazelle, and C. Hur, "The prevalence of Barrett's esophagus in the US: estimates from a simulation model confirmed by SEER data," *Dis Esophagus*, vol. 23, pp. 451-7, Aug 2010.
- [148] A. P. Naef, M. Savary, and L. Ozzello, "Columnar-Lined Lower Esophagus - Acquired Lesion with Malignant Predisposition - Report on 140 Cases of Barretts Esophagus with 12 Adenocarcinomas," *Journal of Thoracic and Cardiovascular Surgery*, vol. 70, pp. 826-835, 1975.
- [149] www.cancer.org, American Cancer Society.
- [150] W. J. Blot, S. S. Devesa, and J. F. Fraumeni, Jr., "Continuing climb in rates of esophageal adenocarcinoma: an update," *JAMA*, vol. 270, p. 1320, Sep 15 1993.
- [151] S. S. Devesa, W. J. Blot, and J. F. Fraumeni, Jr., "Changing patterns in the incidence of esophageal and gastric carcinoma in the United States," *Cancer*, vol. 83, pp. 2049-53, Nov 15 1998.
- [152] N. J. Shaheen, B. F. Overholt, R. E. Sampliner, H. C. Wolfsen, K. K. Wang, D. E. Fleischer, V. K. Sharma, G. M. Eisen, M. B. Fennerty, J. G. Hunter, M. P. Bronner, J. R. Goldblum, A. E. Bennett, H. Mashimo, R. I. Rothstein, S. R. Gordon, S. A. Edmundowicz, R. D. Madanick, A. F. Peery, V. R. Muthusamy, K. J. Chang, M. B. Kimmey, S. J. Spechler, A. A. Siddiqui, R. F. Souza, A. Infantolino, J. A. Dumot, G. W. Falk, J. A. Galanko, B. A. Jobe, R. H. Hawes, B. J. Hoffman, P. Sharma, A. Chak, and C. J. Lightdale, "Durability of Radiofrequency Ablation in Barrett's Esophagus With Dysplasia," *Gastroenterology*, vol. 141, pp. 460-468, 2011.
- [153] D. E. Fleischer, B. F. Overholt, V. K. Sharma, A. Reymunde, M. B. Kimmey, R. Chuttani, K. J. Chang, R. Muthasamy, C. J. Lightdale, N. Santiago, D. K. Pleskow, P. J. Dean, and K. K. Wang, "Endoscopic radiofrequency ablation for Barrett's esophagus: 5-year outcomes from a prospective multicenter trial," *Endoscopy*, vol. 42, pp. 781,789, 2010.
- [154] B. Vaccaro, S. Gonzalez, J. Poneros, P. Stevens, K. Capiak, C. Lightdale, and J. Abrams, "Detection of Intestinal Metaplasia After Successful Eradication of Barrett's Esophagus with Radiofrequency Ablation," *Digestive Diseases and Sciences*, vol. 56, pp. 1996-2000, 2011.
- [155] R. E. Pouw, J. J. Gondrie, A. M. Rygiel, C. M. Sondermeijer, F. J. ten Kate, R. D. Odze, M. Vieth, K. K. Krishnadath, and J. J. Bergman, "Properties of the Neosquamous Epithelium After Radiofrequency Ablation of Barrett's Esophagus Containing Neoplasia," *American Journal of Gastroenterology*, vol. 104, pp. 1366-1373, Jun 2009.
- [156] D. C. Adler, Y. Chen, R. Huber, J. Schmitt, J. Connolly, and J. G. Fujimoto, "Three-dimensional endomicroscopy using optical coherence tomography," *Nature Photonics*, vol. 1, pp. 709-716, Dec 2007.
- [157] D. C. Adler, C. Zhou, T. H. Tsai, J. Schmitt, Q. Huang, H. Mashimo, and J. G. Fujimoto, "Three-dimensional endomicroscopy of the human colon using optical coherence tomography," *Optics Express*, vol. 17, pp. 784-796, 2009.
- [158] B. J. Vakoc, M. Shishko, S. H. Yun, W. Y. Oh, M. J. Suter, A. E. Desjardins, J. A. Evans, N. S. Nishioka, G. J. Tearney, and B. E. Bouma, "Comprehensive esophageal microscopy by using optical frequency-domain imaging (with video)," *Gastrointestinal Endoscopy*, vol. 65, pp. 898-905, May 2007.
- [159] M. J. Suter, B. J. Vakoc, P. S. Yachinski, M. Shishkov, G. Y. Lauwers, M. Mino-Kenudson, B. E. Bouma, N. S. Nishioka, and G. J. Tearney, "Comprehensive microscopy of the esophagus in human patients with optical frequency domain imaging," *Gastrointestinal Endoscopy*, vol. 68, pp. 745-53, Oct 2008.
- [160] C. Zhou, T. H. Tsai, H. C. Lee, T. Kirtane, M. Figueiredo, Y. K. Tao, O. O. Ahsen, D. C. Adler, J. M. Schmitt, Q. Huang, J. G. Fujimoto, and H. Mashimo, "Characterization of buried glands before and after radiofrequency ablation by using 3-dimensional optical coherence tomography (with videos)," *Gastrointest Endosc*, vol. 76, pp. 32-40, Jul 2012.
- [161] T. H. Tsai, H. C. Lee, O. O. Ahsen, K. Liang, M. G. Giacomelli, B. Potsaid, Y. K. Tao, V. Jayaraman, M. Figueiredo, Q. Huang, A. Cable, J. G. Fujimoto, and H. Mashimo, "Itrahigh speed endoscopic optical coherence tomography for gastroenterology," *Biomed. Opt. Express*, vol. 5, pp. 4387-4404, Dec 1 2014.
- [162] F. Hvid-Jensen, L. Pedersen, A. M. Drewes, H. T. Sorensen, and P. Funch-Jensen, "Incidence of Adenocarcinoma among Patients with Barrett's Esophagus," *New England Journal of Medicine*, vol. 365, pp. 1375-1383, Oct 13 2011.

- [163] B. J. Reid, D. S. Levine, G. Longton, P. L. Blount, and P. S. Rabinovitch, "Predictors of progression to cancer in Barrett's esophagus: baseline histology and flow cytometry identify low- and high-risk patient subsets," *Am J Gastroenterol*, vol. 95, pp. 1669-76, Jul 2000.
- [164] N. S. Buttar, K. K. Wang, T. J. Sebo, D. M. Riehle, K. K. Krishnadath, L. S. Lutzke, M. A. Anderson, T. M. Petterson, and L. J. Burgart, "Extent of high-grade dysplasia in Barrett's esophagus correlates with risk of adenocarcinoma," *Gastroenterology*, vol. 120, pp. 1630-9, Jun 2001.
- [165] S. J. Spechler, "Dysplasia in Barrett's esophagus: limitations of current management strategies," *Am J Gastroenterol*, vol. 100, pp. 927-35, Apr 2005.
- [166] G. Isenberg, M. V. Sivak, Jr., A. Chak, R. C. Wong, J. E. Willis, B. Wolf, D. Y. Rowland, A. Das, and A. Rollins, "Accuracy of endoscopic optical coherence tomography in the detection of dysplasia in Barrett's esophagus: a prospective, double-blinded study," *Gastrointest Endosc*, vol. 62, pp. 825-31, Dec 2005.
- [167] J. A. Evans, J. M. Poneros, B. E. Bouma, J. Bressner, E. F. Halpern, M. Shishkov, G. Y. Lauwers, M. Mino-Kenudson, N. S. Nishioka, and G. J. Tearney, "Optical coherence tomography to identify intramucosal carcinoma and high-grade dysplasia in Barrett's esophagus," *Clin Gastroenterol Hepatol*, vol. 4, pp. 38-43, Jan 2006.
- [168] W. Kang, H. Wang, Z. Wang, M. W. Jenkins, G. A. Isenberg, A. Chak, and A. M. Rollins, "Motion artifacts associated with in vivo endoscopic OCT images of the esophagus," *Optics Express*, vol. 19, pp. 20722-35, Oct 10 2011.
- [169] P. Sharma, A. Bansal, S. Mathur, S. Wani, R. Cherian, D. McGregor, A. Higbee, S. Hall, and A. Weston, "The utility of a novel narrow band imaging endoscopy system in patients with Barrett's esophagus," *Gastrointestinal Endoscopy*, vol. 64, pp. 167-175, 2006.
- [170] J. K. Barton and S. Stromski, "Flow measurement without phase information in optical coherence tomography images," *Optics Express*, vol. 13, pp. 5234-5239, Jul 11 2005.
- [171] V. X. Yang, S. J. Tang, M. L. Gordon, B. Qi, G. Gardiner, M. Cirocco, P. Kortan, G. B. Haber, G. Kandel, I. A. Vitkin, B. C. Wilson, and N. E. Marcon, "Endoscopic Doppler optical coherence tomography in the human GI tract: initial experience," *Gastrointest Endosc*, vol. 61, pp. 879-90, Jun 2005.
- [172] O. O. Ahsen, H. C. Lee, M. G. Giacomelli, Z. Wang, K. Liang, T. H. Tsai, B. Potsaid, H. Mashimo, and J. G. Fujimoto, "Correction of rotational distortion for catheter-based en face OCT and OCT angiography," *Opt Lett*, vol. 39, pp. 5973-6, Oct 15 2014.
- [173] *American Cancer Society: Cancer Facts & Figures*, 2012.
- [174] M. Morrow, R. Jagsi, A. K. Alderman, J. J. Griggs, S. T. Hawley, A. S. Hamilton, J. J. Graff, and S. J. Katz, "Surgeon Recommendations and Receipt of Mastectomy for Treatment of Breast Cancer," *Jama-Journal of the American Medical Association*, vol. 302, pp. 1551-1556, Oct 14 2009.
- [175] M. Morrow, E. A. Strom, L. W. Bassett, D. D. Dershaw, B. Fowble, J. R. Harris, F. O'Malley, S. J. Schnitt, S. E. Singletary, and D. P. Winchester, "Standard for the Management of Ductal Carcinoma In Situ of the Breast (DCIS)," *CA: A Cancer Journal for Clinicians*, vol. 52, pp. 256-276, 2002.
- [176] M. Morrow, E. A. Strom, L. W. Bassett, D. D. Dershaw, B. Fowble, A. Giuliano, J. R. Harris, F. O'Malley, S. J. Schnitt, S. E. Singletary, and D. P. Winchester, "Standard for Breast Conservation Therapy in the Management of Invasive Breast Carcinoma," *CA: A Cancer Journal for Clinicians*, vol. 52, pp. 277-300, 2002.
- [177] D. S. Cooper, G. M. Doherty, B. R. Haugen, B. R. Hauger, R. T. Kloos, S. L. Lee, S. J. Mandel, E. L. Mazzaferri, B. McIver, F. Pacini, M. Schlumberger, S. I. Sherman, D. L. Steward, and R. M. Tuttle, "Revised American Thyroid Association management guidelines for patients with thyroid nodules and differentiated thyroid cancer.," *Thyroid : official journal of the American Thyroid Association*, vol. 19, pp. 1167-214, 2009.
- [178] T. Carling and R. Udelsman, "Follicular neoplasms of the thyroid: what to recommend.," *Thyroid : official journal of the American Thyroid Association*, vol. 15, pp. 583-7, 2005.
- [179] J. D. Bancroft and A. Stevens, *Theory and practice of histological techniques*, 6th ed. Edinburgh ; New York: Churchill Livingstone, 2008.
- [180] R. Arriagada, M. G. Le, F. Rochard, and G. Contesso, "Conservative treatment versus mastectomy in early breast cancer: patterns of failure with 15 years of follow-up data. Institut Gustave-Roussy Breast Cancer Group," *J Clin Oncol*, vol. 14, pp. 1558-64, May 1996.
- [181] B. Fisher, S. Anderson, J. Bryant, R. G. Margolese, M. Deutsch, E. R. Fisher, J.-H. Jeong, and N. Wolmark, "Twenty-Year Follow-up of a Randomized Trial Comparing Total Mastectomy, Lumpectomy, and Lumpectomy plus Irradiation for the Treatment of Invasive Breast Cancer," *New England Journal of Medicine*, vol. 347, pp. 1233-1241, 2002.

- [182] J. A. van Dongen, A. C. Voogd, I. S. Fentiman, C. Legrand, R. J. Sylvester, D. Tong, E. van der Schueren, P. A. Helle, K. van Zijl, and H. Bartelink, "Long-term results of a randomized trial comparing breast-conserving therapy with mastectomy: European Organization for Research and Treatment of Cancer 10801 trial," *J Natl Cancer Inst*, vol. 92, pp. 1143-50, Jul 19 2000.
- [183] J. J. Coen, A. G. Taghian, L. A. Kachnic, S. I. Assaad, and S. N. Powell, "Risk of lymphedema after regional nodal irradiation with breast conservation therapy," *Int J Radiat Oncol Biol Phys*, vol. 55, pp. 1209-15, Apr 1 2003.
- [184] I. L. Nesvold, A. A. Dahl, E. Lokkevik, A. Marit Mengshoel, and S. D. Fossa, "Arm and shoulder morbidity in breast cancer patients after breast-conserving therapy versus mastectomy," *Acta Oncol*, vol. 47, pp. 835-42, 2008.
- [185] G. A. Cefaro, D. Genovesi, R. Marchese, L. A. Ursini, E. Cianchetti, E. Ballone, and M. Di Nicola, "Predictors of local recurrence after conservative surgery and whole-breast irradiation," *Breast Cancer Res Treat*, vol. 98, pp. 329-35, Aug 2006.
- [186] J. L. Connolly, J. Boyages, A. J. Nixon, G. Peiro, I. Gage, B. Silver, A. Recht, J. R. Harris, and S. J. Schnitt, "Predictors of breast recurrence after conservative surgery and radiation therapy for invasive breast cancer," *Mod Pathol*, vol. 11, pp. 134-9, Feb 1998.
- [187] F. J. Fleming, A. D. Hill, E. W. Mc Dermott, A. O'Doherty, N. J. O'Higgins, and C. M. Quinn, "Intraoperative margin assessment and re-excision rate in breast conserving surgery," *Eur J Surg Oncol*, vol. 30, pp. 233-7, Apr 2004.
- [188] G. P. Swanson, K. Ryneerson, and R. Symmonds, "Significance of margins of excision on breast cancer recurrence," *Am J Clin Oncol*, vol. 25, pp. 438-41, Oct 2002.
- [189] D. M. Layfield, A. Agrawal, H. Roche, and R. I. Cutress, "Intraoperative assessment of sentinel lymph nodes in breast cancer," *British Journal of Surgery*, vol. 98, pp. 4-17, 2010.
- [190] M. R. Weiser, L. L. Montgomery, B. Susnik, L. K. Tan, P. I. Borgen, and H. S. Cody, "Is routine intraoperative frozen-section examination of sentinel lymph nodes in breast cancer worthwhile?," *Ann Surg Oncol*, vol. 7, pp. 651-655, Oct 2000.
- [191] T. P. Olson, J. Harter, A. Munoz, D. M. Mahvi, and T. Breslin, "Frozen section analysis for intraoperative margin assessment during breast-conserving surgery results in low rates of re-excision and local recurrence," *Ann Surg Oncol*, vol. 14, pp. 2953-60, Oct 2007.
- [192] S. L. Blair, K. Thompson, J. Rococco, V. Malcarne, P. D. Beitsch, and D. W. Ollila, "Attaining Negative Margins in Breast-Conservation Operations: Is There a Consensus among Breast Surgeons?," *Journal of the American College of Surgeons*, vol. 209, pp. 608-613, Nov 2009.
- [193] E. Leteurtre, X. Leroy, F. Pattou, a. Wacrenier, B. Carnaille, C. Proye, and M. Lecomte-Houcke, "Why do frozen sections have limited value in encapsulated or minimally invasive follicular carcinoma of the thyroid?," *American journal of clinical pathology*, vol. 115, pp. 370-4, 2001.
- [194] R. Udelsman, W. H. Westra, P. I. Donovan, T. a. Sohn, and J. L. Cameron, "Randomized prospective evaluation of frozen-section analysis for follicular neoplasms of the thyroid.," *Annals of surgery*, vol. 233, pp. 716-22, 2001.
- [195] F. Helmchen and W. Denk, "Deep tissue two-photon microscopy," *Nature Methods*, vol. 2, pp. 932-940, Dec 2005.
- [196] W. R. Zipfel, R. M. Williams, R. Christie, A. Y. Nikitin, B. T. Hyman, and W. W. Webb, "Live tissue intrinsic emission microscopy using multiphoton-excited native fluorescence and second harmonic generation," *Proc Natl Acad Sci U S A*, vol. 100, pp. 7075-80, Jun 10 2003.
- [197] P. P. Provenzano, D. R. Inman, K. W. Eliceiri, J. G. Knittel, L. Yan, C. T. Rueden, J. G. White, and P. J. Keely, "Collagen density promotes mammary tumor initiation and progression," *BMC Med*, vol. 6, p. 11, 2008.
- [198] P. P. Provenzano, K. W. Eliceiri, J. M. Campbell, D. R. Inman, J. G. White, and P. J. Keely, "Collagen reorganization at the tumor-stromal interface facilitates local invasion," *BMC Med*, vol. 4, p. 38, 2006.
- [199] S. J. Schnitt, "The diagnosis and management of pre-invasive breast disease: flat epithelial atypia--classification, pathologic features and clinical significance," *Breast Cancer Res*, vol. 5, pp. 263-8, 2003.
- [200] S. Meng, D. Tripathy, E. P. Frenkel, S. Shete, E. Z. Naftalis, J. F. Huth, P. D. Beitsch, M. Leitch, S. Hoover, D. Euhus, B. Haley, L. Morrison, T. P. Fleming, D. Herlyn, L. W. Terstappen, T. Fehm, T. F. Tucker, N. Lane, J. Wang, and J. W. Uhr, "Circulating tumor cells in patients with breast cancer dormancy," *Clin Cancer Res*, vol. 10, pp. 8152-62, Dec 15 2004.
- [201] M. C. Skala, K. M. Riching, D. K. Bird, A. Gendron-Fitzpatrick, J. Eickhoff, K. W. Eliceiri, P. J. Keely, and N. Ramanujam, "In vivo multiphoton fluorescence lifetime imaging of protein-bound and free

- nicotinamide adenine dinucleotide in normal and precancerous epithelia," *Journal of Biomedical Optics*, vol. 12, pp. 024014-024014, 2007.
- [202] M. C. Skala, K. M. Riching, A. Gendron-Fitzpatrick, J. Eickhoff, K. W. Eliceiri, J. G. White, and N. Ramanujam, "In vivo multiphoton microscopy of NADH and FAD redox states, fluorescence lifetimes, and cellular morphology in precancerous epithelia," *Proc Natl Acad Sci U S A*, vol. 104, pp. 19494-9, 2007.
- [203] H.-J. Lin, P. Herman, and J. R. Lakowicz, "Fluorescence lifetime-resolved pH imaging of living cells.," *Cytometry. Part A : the journal of the International Society for Analytical Cytology*, vol. 52, pp. 77-89, 2003.
- [204] K. Okabe, N. Inada, C. Gota, Y. Harada, T. Funatsu, and S. Uchiyama, "Intracellular temperature mapping with a fluorescent polymeric thermometer and fluorescence lifetime imaging microscopy.," *Nature communications*, vol. 3, p. 705, 2012.
- [205] V. K. Ramanujan, J.-H. Zhang, E. Biener, and B. Herman, "Multiphoton fluorescence lifetime contrast in deep tissue imaging: prospects in redox imaging and disease diagnosis," *Journal of ...*, vol. 10, p. 051407, 2005.
- [206] P. J. Tadrous, J. Siegel, P. M. W. French, S. Shousha, E.-N. Lalani, and G. W. H. Stamp, "Fluorescence lifetime imaging of unstained tissues: early results in human breast cancer," *The Journal of pathology*, vol. 199, pp. 309-17, 2003.
- [207] M. W. Conklin, P. P. Provenzano, K. W. Eliceiri, R. Sullivan, and P. J. Keely, "Fluorescence lifetime imaging of endogenous fluorophores in histopathology sections reveals differences between normal and tumor epithelium in carcinoma in situ of the breast.," *Cell biochemistry and biophysics*, vol. 53, pp. 145-57, 2009.
- [208] D. L. Price, S. K. Chow, N. A. B. Maclean, H. Hakoziaki, S. Peltier, M. E. Martone, and M. H. Ellisman, "High-Resolution Large-Scale Mosaic Imaging Using Multiphoton Microscopy to Characterize Transgenic Mouse Models of Human Neurological Disorders," vol. 00, pp. 65-80, 2006.
- [209] D. D. U. Li, J. Arlt, D. Tyndall, R. Walker, J. Richardson, D. Stoppa, E. Charbon, and R. K. Henderson, "Video-rate fluorescence lifetime imaging camera with CMOS single-photon avalanche diode arrays and high-speed imaging algorithm," *Journal of Biomedical Optics*, vol. 16, pp. 096012-096012, 2011.
- [210] R. Patalay, C. Talbot, Y. Alexandrov, I. Munro, M. a. a. Neil, K. König, P. French, A. Chu, G. W. Stamp, and C. Dunsby, "Quantification of cellular autofluorescence of human skin using multiphoton tomography and fluorescence lifetime imaging in two spectral detection channels.," *Biomedical optics express*, vol. 2, pp. 3295-308, 2011.
- [211] R. Patalay, C. Talbot, Y. Alexandrov, M. O. Lenz, S. Kumar, S. Warren, I. Munro, M. a. a. Neil, K. König, P. M. W. French, A. Chu, G. W. H. Stamp, and C. Dunsby, "Multiphoton multispectral fluorescence lifetime tomography for the evaluation of basal cell carcinomas," *Plos One*, vol. 7, pp. e43460-e43460, 2012.
- [212] J. McGinty, N. P. Galletly, C. Dunsby, I. Munro, D. S. Elson, J. Requejo-Isidro, P. Cohen, R. Ahmad, A. Forsyth, A. V. Thillainayagam, M. a. a. Neil, P. M. W. French, and G. W. Stamp, "Wide-field fluorescence lifetime imaging of cancer," *Biomedical optics express*, vol. 1, pp. 627-640, 2010.
- [213] K. Dowling, M. J. Dayel, M. J. Lever, P. M. W. French, J. D. Hares, and a. K. Dymoke-Bradshaw, "Fluorescence lifetime imaging with picosecond resolution for biomedical applications," *Optics Letters*, vol. 23, pp. 810-2, 1998.
- [214] J. A. Izatt, M. D. Kulkarni, H. W. Wang, K. Kobayashi, and M. V. Sivak, "Optical coherence tomography and microscopy in gastrointestinal tissues," *Ieee Journal of Selected Topics in Quantum Electronics*, vol. 2, pp. 1017-1028, Dec 1996.
- [215] M. A. Choma, A. K. Ellerbee, C. H. Yang, T. L. Creazzo, and J. A. Izatt, "Spectral-domain phase microscopy," *Optics Letters*, vol. 30, pp. 1162-1164, May 15 2005.
- [216] C. Y. Xu, C. Vinegoni, T. S. Ralston, W. Luo, W. Tan, and S. A. Boppart, "Spectroscopic spectral-domain optical coherence microscopy," *Optics Letters*, vol. 31, pp. 1079-1081, Apr 15 2006.
- [217] A. D. Aguirre, Y. Chen, B. Bryan, H. Mashimo, Q. Huang, J. L. Connolly, and J. G. Fujimoto, "Cellular resolution ex vivo imaging of gastrointestinal tissues with optical coherence microscopy," *Journal of Biomedical Optics*, vol. 15, p. 016025, 2010 2010.
- [218] C. Zhou, D. W. Cohen, Y. Wang, H.-C. Lee, A. E. Mondelblatt, T.-H. Tsai, A. D. Aguirre, J. G. Fujimoto, and J. L. Connolly, "Integrated Optical Coherence Tomography and Microscopy for Ex Vivo Multiscale Evaluation of Human Breast Tissues," *Cancer Research*, vol. 70, pp. 10071-10079, Dec 15 2010.

- [219] C. Zhou, Y. Wang, A. D. Aguirre, T.-H. Tsai, D. W. Cohen, J. L. Connolly, and J. G. Fujimoto, "Ex vivo imaging of human thyroid pathology using integrated optical coherence tomography and optical coherence microscopy," *Journal of Biomedical Optics*, vol. 15, p. 016001, 2010 2010.
- [220] S.-W. Huang, A. D. Aguirre, R. A. Huber, D. C. Adler, and J. G. Fujimoto, "Swept source optical coherence microscopy using a Fourier domain mode-locked laser," *Optics Express*, vol. 15, pp. 6210-6217, May 14 2007.
- [221] V. Jayaraman, J. Jiang, H. Li, P. J. S. Heim, G. D. Cole, B. Potsaid, J. G. Fujimoto, and A. Cable, *OCT Imaging up to 760 kHz Axial Scan Rate Using Single-Mode 1310nm MEMS-Tunable VCSELs with > 100nm Tuning Range*, 2011.
- [222] B. Potsaid, V. Jayaraman, J. G. Fujimoto, J. Jiang, P. J. S. Heim, and A. E. Cable, "MEMS tunable VCSEL light source for ultrahigh speed 60kHz-1MHz axial scan rate and long range centimeter class OCT imaging," in *Optical Coherence Tomography and Coherence Domain Optical Methods in Biomedicine XVI*, vol. 8213, J. A. F. J. G. T. V. V. Izatt, Ed., ed, 2012.
- [223] O. O. Ahsen, Y. K. Tao, B. M. Potsaid, Y. Sheikine, J. Jiang, I. Grulkowski, T. H. Tsai, V. Jayaraman, M. F. Kraus, J. L. Connolly, J. Horneegger, A. Cable, and J. G. Fujimoto, "Swept source optical coherence microscopy using a 1310 nm VCSEL light source," *Opt Express*, vol. 21, pp. 18021-33, 2013/7 2013.
- [224] H. C. Lee, J. J. Liu, Y. Sheikine, A. D. Aguirre, J. L. Connolly, and J. G. Fujimoto, "Ultrahigh speed spectral-domain optical coherence microscopy," *Biomed Opt Express*, vol. 4, pp. 1236-54, 2013/9/07 2013.
- [225] R. Virmani, F. D. Kolodgie, A. P. Burke, A. Farb, and S. M. Schwartz, "Lessons From Sudden Coronary Death : A Comprehensive Morphological Classification Scheme for Atherosclerotic Lesions," *Arterioscler Thromb Vasc Biol*, vol. 20, pp. 1262-1275, May 1, 2000 2000.
- [226] A. Farb, A. P. Burke, A. L. Tang, Y. Liang, P. Mannan, J. Smialek, and R. Virmani, "Coronary plaque erosion without rupture into a lipid core A frequent cause of coronary thrombosis in sudden coronary death," *Circulation*, vol. 93, pp. 1354-1363, 1996.
- [227] E. Arbustini, B. Dal Bello, P. Morbini, A. P. Burke, M. Bocciarelli, G. Specchia, and R. Virmani, "Plaque erosion is a major substrate for coronary thrombosis in acute myocardial infarction," *Heart*, vol. 82, pp. 269-272, 1999.
- [228] R. Virmani, A. P. Burke, A. Farb, and F. D. Kolodgie, "Pathology of the Vulnerable Plaque," *J Am Coll Cardiol*, vol. 47, pp. C13-18, April 18, 2006 2006.
- [229] Z. Wang, H. Jia, J. Tian, T. Soeda, R. Vergallo, Y. Minami, H. Lee, A. Aguirre, J. G. Fujimoto, and I.-K. Jang, "Computer-Aided Image Analysis Algorithm to Enhance In Vivo Diagnosis of Plaque Erosion by Intravascular Optical Coherence Tomography," *Circulation: Cardiovascular Imaging*, vol. 7, pp. 805-810, 2014.
- [230] P. K. Shah, "Pathophysiology of coronary thrombosis: role of plaque rupture and plaque erosion," *Progress in Cardiovascular Diseases*, vol. 44, pp. 357-368, 2002.
- [231] Y. Chen, P. M. Andrews, A. D. Aguirre, J. M. Schmitt, and J. G. Fujimoto, "High-resolution three-dimensional optical coherence tomography imaging of kidney microanatomy ex vivo," *J Biomed Opt*, vol. 12, p. 034008, May-Jun 2007.
- [232] P. M. Andrews, Y. Chen, M. L. Onozato, S. W. Huang, D. C. Adler, R. A. Huber, J. Jiang, S. E. Barry, A. E. Cable, and J. G. Fujimoto, "High-resolution optical coherence tomography imaging of the living kidney," *Lab Invest*, vol. 88, pp. 441-9, Apr 2008.
- [233] P. M. Andrews, M. Cooper, J. Verbesey, S. Ghasemian, D. Rogalsky, P. Moody, A. Chen, P. Alexandrov, H. W. Wang, and Y. Chen, "Mannitol infusion within 15 min of cross-clamp improves living donor kidney preservation," *Transplantation*, vol. 98, pp. 893-7, Oct 27 2014.